

# Active Illumination and Computational Methods for Temporal and Spectral Super-Resolution Microscopy

Présentée le 3 septembre 2020

à la Faculté des sciences et techniques de l'ingénieur  
Laboratoire de l'IDIAP  
Programme doctoral en génie électrique

pour l'obtention du grade de Docteur ès Sciences

par

**Christian JAQUES**

Acceptée sur proposition du jury

Prof. M. Unser, président du jury  
Dr. J.-M. Odobez, Dr. M. Liebling, directeurs de thèse  
Dr W. Supatto, rapporteur  
Dr C. Kervrann, rapporteur  
Prof. S. Süsstrunk, rapporteuse



# Abstract

Light microscopy is a tool of paramount importance for biologists and has been constantly improved for the past four centuries. Despite many recent developments, microscopy techniques still require improvement, especially to reach better temporal and spectral resolutions. In particular, many high-end microscopes favor mostly spatial resolution, at the expense of the latter two types of resolution.

In this thesis, we present methods based on the use of active illumination and computational algorithms to increase temporal and spectral resolutions of microscopes. Our methods aim to provide users with the flexibility to choose, within a single instrument, which type of resolution is to be favored based on the application at hand. More generally, our approach has fundamental implications on the signal sensing procedure, allowing, for example, to mitigate temporal aliasing in sequences of images.

Our first method performs temporal super-resolution imaging of monochrome scenes using a hue-encoded shutter. By making use of an active multi-spectral illumination, temporal information is encoded in the hue of the acquisitions. We characterize the method showing a resolution improvement of 2.8 and an increase of frame-rate of a factor 3. We demonstrate the applicability of our method to bright-field transmission microscopy by applying the method to the beating heart of a zebrafish embryo. We then extend this method to fluorescence microscopy. We add a temporal regularization term to make the method robust to fluorescent labelings inhomogeneities. We present an application of the method to the beating heart of a fluorescently-labeled zebrafish that emits fluorescent light of two different colors. Implementing our method within a light-sheet microscope allows us to reconstruct 3D+time videos of the beating heart at twice the acquisition frame-rate.

Our second method offers a way to perform temporal generalized sampling by computing simultaneous inner products with the sampled signal. Similarly to the first method, we take advantage of working with multiple illumination hues to compute as many simultaneous inner products, which we retrieve via an unmixing procedure. We use equivalent basic and dual B-splines representations to ensure having finite-length and positive pre-filters, as well as finite-support reconstruction functions. We show applications of our method to a fast rotating target, as well as to the beating heart of a zebrafish embryo, both in transmission and fluorescence microscopy.

## Abstract

---

Finally, we introduce a method to perform spectral imaging of repeating processes, such as the beating heart. The method sequentially acquires multiple movies with various filters, performs temporal registration of all movies and reconstructs a spectral movie through solving of a spectral unmixing problem, pixel by pixel, at each time point. We characterize the method and show a median error of approximately 10%, by comparing reconstructions on a static sample from our method with measurements obtained with a spectrometer. We then perform validation by comparing static reconstructions with dynamic ones of the same sample. We demonstrate the potential of the method to microscopy by performing spectral imaging of the beating heart of a zebrafish embryo.

Taken together, these methods offer a versatile toolbox to improve the temporal or spectral resolution in both bright field and fluorescence microscopy, which we foresee could be directly implemented in a number of specialized instruments.

*Keywords:* computational imaging, light microscopy, fluorescence microscopy, active illumination, temporal super-resolution imaging, spectral imaging, unmixing, generalized sampling, inverse problems.

# Résumé

La microscopie est un outil primordial pour les biologistes, en constante évolution depuis les quatre derniers siècles. Malgré les multiples développements récents dont a bénéficié la microscopie, il est toujours nécessaire d'améliorer les résolutions temporelle et spectrale des microscopes. De plus, les microscopes actuels tendent à ne favoriser qu'une forme de résolution (en général spatiale), aux dépens des autres formes de résolution.

Dans cette thèse, nous présentons de nouvelles méthodes basées sur des illuminations active et des algorithmes computationnels pour augmenter la résolution temporelle et spectrale en microscopie. Nos méthodes permettent aussi plus de flexibilité dans l'utilisation des microscopes, permettant à l'utilisateur de choisir quel type de résolution favoriser, sans devoir changer d'équipement. Plus généralement, notre approche a des implications plus fondamentales en échantillonnage du signal, permettant de fortement réduire les artéfacts de repliement (aliasing) temporel lors d'acquisitions de vidéos.

Notre première méthode permet de faire de la super-résolution temporelle de scènes monochromes à l'aide d'un obturateur encodé dans les couleurs. Nous caractérisons la méthode et montrons une amélioration de la résolution temporelle d'un facteur 2.8 ainsi qu'une augmentation de la fréquence des images d'un facteur 3. Nous démontrons l'utilisation possible de notre méthode en microscopie par transmission, en l'utilisant pour imager un coeur d'embryon de poisson zèbre. Nous étendons ensuite cette méthode à la microscopie par fluorescence. Pour rendre la méthode robuste aux variations de marquage fluorescent, nous introduisons un terme de régularisation temporelle. Nous présentons ensuite une application de cette méthode sur un coeur d'embryon de poisson génétiquement modifié pour émettre de la lumière par fluorescence de deux couleurs différentes. En implémentant notre méthode sur un microscope à illumination par feuille mince, nous pouvons reconstruire un volume en vidéo (3D + temps) du coeur, à deux fois la fréquence d'acquisition des images.

Ensuite, nous présentons une méthode d'échantillonnage généralisé dans le temps grâce au calcul simultané de plusieurs produits intérieurs entre une illumination active et le signal échantillonné. De manière similaire à notre première méthode, divers signaux sont multiplexés dans le spectre des couleurs et retrouvés après démixage. Nous utilisons les représentations B-spline basique et duale, qui sont équivalentes, pour utiliser des pré-filtres de durée finie et qui restent positifs, ainsi que des fonctions de reconstructions à support fini. Nous montrons

## Résumé

---

des résultats de notre méthode appliquée à une grille qui tourne à rapidement, ainsi qu'à un coeur de poisson zèbre en microscopie par transmission et par fluorescence.

Finalement, nous présentons une méthode d'imagerie spectrale de procédés répétitifs, tel que le battement cardiaque. La méthode acquiert plusieurs vidéos de manière séquentielle, avec différents filtres, aligne dans le temps toutes les vidéos et reconstruit une vidéo spectrale en résolvant un problème inverse, à chaque pixel pour chaque point dans le temps. Nous caractérisons la méthode et montrons une erreur médiane d'environ 10% en comparant des reconstructions obtenues avec notre méthode et des mesures par spectromètre d'échantillons statiques, et nous validons la méthode en comparant les reconstructions du même objet, une fois statique puis dynamique. Nous démontrons le potentiel de la méthode pour la microscopie en l'appliquant à un coeur d'embryon de poisson zèbre.

Toutes ces méthodes offrent de nouveaux outils flexibles pour améliorer les résolutions temporelle ou spectrale en microscopie par transmission et par fluorescence, qui peuvent être directement appliquées dans nombre d'instruments spécialisés.

*Mots clés* : imagerie computationnelle, microscopie optique, microscopie par fluorescence, illumination active, super-résolution temporelle pour l'imagerie, imagerie spectrale, démêlage, échantillonnage généralisé, problèmes inverses.

*To my parents.*

You can tell whether a man is clever by his answers.  
You can tell whether a man is wise by his questions.  
— Naguib Mahfouz

The 'J' in PhD stands for Joy.  
— CJ





# Acknowledgements

A thesis is never the result of a person's sole work and I would like to thank many people who contributed to this thesis, one way or another, intentionally or not. Let me apologise already, for I cannot mention everybody who deserves my appreciation. Rest assured that I do not forget your kindness, positivity, encouragements, gentle mockeries, and other ways to push a fellow human being forward.

First, Michael. Thank you so much. For giving me the opportunity to be your first PhD in Switzerland. For your constant pursuit of a high "signal-to-noise ratio" research which has been challenging at first, before becoming inspiring. Still now, I'm amazed by your unfailing ability to keep a sharp and critical point of view, striving to improve any piece of research coming by your most capable hands. Finally, for your continuous support and encouragements, I would not have completed this thesis otherwise.

Thank you Jean-Marc for the opportunity to work at Idiap and for your always opened door. We did not, *yet*, find the time to go ski-touring together. I trust this will be corrected soon.

All my gratitude goes to the brilliant scientists who kindly agreed to be part of my jury : Michaël Unser, Sabine Süsstrunk, Charles Kervrann, and Willy Supatto. Your positive feedback and numerous suggestions were incredibly welcome at a time where I struggled to see the relevance of my research.

To my colleagues, Olivia and François (M.), I have more than thanks to give. Olivia, I will always keep a fond memory of our many, many coffee discussions, our mountain trips, especially the Weissmies, the lunch jogs, the painfully long demo preparations, ... We first traded coding advice before delving into more philosophical discussions, such as the helpless selfishness of humanity. If I recall, I even gave you political asylum once or twice. We shared coffees before enjoying together some Nikka, Ardbeg, Octomore, and the likes. You made my PhD journey way better, I will always be thankful for it and I am proud to call you a friend.

To François, I know for a fact that you will excel in your research. Your help with the microscope has been great, I definitely owe you some light-sheet optical fine-tuning for life. Congratulations on being impossible to upset. I took it as a challenge but you definitely got the better of me and I am left with no other choice but to admit that you are a kind, smart, great guy. I look forward to seeing you become anything you set your mind to, go get them!

There are so many great people at Idiap that, once again, I apologize for not mentioning

## Acknowledgements

---

everybody deserving of my gratitude. Thanks a lot to the whole IT-crew who were extremely helpful when building our microscope. Frank, Louis-Marie, Bastien for your smiling support, it was great. Of course, thank you Nadine, Sylvie and Elisa for your support, Idiap feels like a big family thanks to you. Angelos, Nam, Pavel, Bastien, Guillaume (C.), Guillaume (H.), Phil, Salim (igré), Noémie, Rémy, Sandrine ... Our coffee breaks could not be better, thank you! Thank you Pavel for not breaking my leg at unihockey.

Special thanks to David (G.), for *never* losing faith in us. I am still a lost cause, however. Your warm, kind words during these times where anything but research looked interesting were a tremendous help. They meant a lot. They still do.

François (Fo.), I hope that you do get that sub-4 hours one! All these lunch jogs... It was super to have a running friend that was not scared of snow storms or daunting heats. Not running because of a storm is for sissies!

Special thanks to Kiki, Alizée, Vinch, Coucou, France, Rams, Elise and Deb for being great running friends. Well, friends in general, at Sat, along the long way up to “la Rosablancche” and everywhere else. Kiki, in exchange for all the therapy sessions, I’ll teach you how to ask for water in German.

To Thibaut and Manu, I owe a lot. I will always keep a fond memory to our mountain tours, the worse the weather, the better. I’m convinced that someday we will Géné-peak together (my apologies). Being “La Valerette”, “la Grande Lui”, “la Dent Jaune” or other classics, we spent great moments up there. We even spent *some* time at the coffee machine, as incredible as it may sound, I found these moments to be somehow productive thanks to the number of ideas discussed, laughed at, re-discussed, taken seriously, pushed further and even sometimes published... Go figure!

Thanks to other mountain buddies : Bichon, Flo, Jonas, and Yann (L.). I think that by now Bichon and Jonas are able to explain this thesis as well as I can thanks to them hearing endless discussions about it that Flo, Manu and I had along the way up... “Une caisse de mutant” was the only way to avoid these annoying talks.

Thanks Axel, Regis, Monseigneur, Jonas, Steve, Schnapps, Roman for taking me rock-climbing with you. Being afraid, hanging to a rope, is a surprisingly efficient way to forget typical PhD’s trivia.

My gratitude to all of the MU gang, Laurène, Anaïs, Julien, Thanh-An, Daniel, Virginie. I envy the friendly, positive, caring towards one-another, encouraging atmosphere that you developed and thank you forever for accepting us in your group. You all rock and I look forward to seeing you in the future, it might be with a beer at hand.

A big thank you to my Mikron friends, that I keep coming back to. My brief appearances have been highly refreshing (well, to me at least) and were a big moral help through this PhD. Thanks Julien (PJU, from whom I learned way more than I taught him...), Stéphane, Julien (Maitre Gums), Oli, Julien (Dodiniou), Julien (W.), Julien (which one again?), Dejanovic’, Lillilli, Benji, Cédric, Paul, C2, Quentin, Baptiste, Louloutre, Maudit Valaisan, Guuuuh, Gatien (not so

much Mikronien anymore). Of course, thanks to all the runners there, as painful as it was, boy was it fun! Raph l'incroyable, Sergio le grand Shaman, Mica, Bernhard (-iniou), Fabio, Julien (B., the other), Florian (président), and all the others whose joyful sweat has left a mark.

An enormous thank you to the “base aérienne de Sion” for their help in building our light-sheet microscope. I am (well, the whole research group) especially indebted to Vital Emery and André Quinodoz for their time and contributions, without which I would have built three microscopes before having a functional one.

To Ferdi, my brother from another mother, we shared too much to ramble about here. I'll just say that I do not want to see any accident happen. Bjorn, my South-African alter ego, next time I will book us a table. Thank you Amlwch for your delicate yet witty remarks, as well as David for the proofreading and moral support.

To the whole gang of EPFL friends, kudos for being great people and even better friends. Séb, Camille, Jérémy et Aurélie, Max, Aashree, Laurenz, Marco, and all the others that I do not forget. Our studies together were a long time ago but they sure were awesome.

Thanks to all of the extended “amis de la morille”, Damien (whose knees aren't as strong as his squash backhand), Gaëlle, Noémie, Matti, Ted, Margaux, Isa and Marc (sans o). Our evenings are always filled with happy things, as it should be.

Vanesa, I owe you so much that words come short. So much so that I keep my words to me but my heart speaks volumes. Your support has been exactly what I needed. In many ways, this thesis is also yours. With all my love, thank you.

To my family. Papa, Maman, Grand-Papa et Grand-Maman, Raphaël, Malaurie, Aline, Fabrice, Norah et Colin, Pierre et Rita, François et Hanny, thank you all!

Finally, a tribute to some of the music bands who were with me throughout my whole thesis, especially during the gruelling redaction phases : Radiohead, alt-j ( $\Delta$ ), Queens of the Stone Age, Coldplay, Noir Désir, Fauve, Ratatat, Portugal. The Man, Muse, les Cowboys Fringants, Charlie Cunningham, Pink Floyd, Queen, Orelsan, Milky Chance, Army Of The Pharaohs, Thylacine, Daft Punk, Ramin Djawadi.

— CJ



# Contents

<b>Abstract (English/Français)</b>	<b>i</b>
<b>Acknowledgements</b>	<b>vii</b>
<b>List of Figures</b>	<b>xv</b>
<b>1 Introduction</b>	<b>1</b>
1.1 Optical microscopy . . . . .	1
1.2 Motivations and contributions . . . . .	3
1.2.1 Fast imaging and spectral imaging are ubiquitous in many areas . . . . .	6
1.2.2 What is the problem with the current instrumentation? . . . . .	7
1.3 Related work . . . . .	7
1.4 Organization of the thesis . . . . .	8
<b>2 Prerequisites</b>	<b>11</b>
2.1 Concepts of resolution, sampling and super-resolution . . . . .	11
2.1.1 Resolution . . . . .	11
2.1.2 Sampling, a ubiquitous concept . . . . .	14
2.1.3 Introduction to super-resolution . . . . .	15
2.1.4 Comparison of super-resolution with binning or interpolation . . . . .	16
2.2 Fluorescence microscopy . . . . .	16
<b>3 Hue-Encoded Shutter Method for Temporal Super-Resolution Microscopy</b>	<b>19</b>
3.1 Abstract . . . . .	19
3.2 Introduction . . . . .	20
3.3 Imaging Model . . . . .	22
3.4 Methods . . . . .	25
3.4.1 Temporal super-resolution . . . . .	25
3.4.2 Determination of the system spectral mixing coefficients and electronics offsets . . . . .	25
3.4.3 Base-hue recovery and hue-dependent model-selection for non-gray samples . . . . .	27
	xi

## Contents

---

3.5	Experiments . . . . .	28
3.5.1	Hardware and parameters setup . . . . .	28
3.5.2	Resolution improvement characterization . . . . .	29
3.5.3	Characterization of robustness with choice of illumination hues . . . . .	29
3.5.4	The conditioning number of the system matrix depends on the illumination functions . . . . .	31
3.6	Applications . . . . .	32
3.6.1	Model selection applied to two samples . . . . .	32
3.6.2	Fast imaging of the beating heart . . . . .	32
3.7	Discussion . . . . .	34
3.8	Conclusion . . . . .	37
<b>4</b>	<b>Temporal super-resolution fluorescence light-sheet microscopy via a hue-encoded shutter</b>	<b>39</b>
4.1	Abstract . . . . .	39
4.2	Introduction . . . . .	40
4.3	Methods . . . . .	44
4.3.1	Imaging model . . . . .	44
4.3.2	Temporal super-resolution from hue encoded signal . . . . .	47
4.4	Experiments . . . . .	48
4.4.1	Temporal super-resolution light-sheet imaging of the beating heart of a zebrafish . . . . .	49
4.4.2	Homogeneity of the fluorescent co-expression ratio . . . . .	49
4.4.3	Combined fast and color imaging on the beating heart of a zebrafish . . . . .	52
4.4.4	ADMM compared to least-squares without regularization . . . . .	52
4.4.5	Impact on the reconstruction of 3D volumes of the beating heart . . . . .	52
4.4.6	Roadmap to higher super-resolution factors . . . . .	54
4.5	Discussion and Conclusion . . . . .	54
<b>5</b>	<b>Generalized temporal sampling with active illumination in optical microscopy</b>	<b>57</b>
5.1	Abstract . . . . .	57
5.2	Introduction . . . . .	57
5.3	Problem statement . . . . .	59
5.4	Methods . . . . .	61
5.4.1	Multi-color B-spline segments as prefilter kernels . . . . .	61
5.4.2	Spectral unmixing . . . . .	64
5.4.3	Converting to samples . . . . .	64
5.5	Experiments . . . . .	64
5.5.1	Reconstructions from synthetic data . . . . .	64

---

5.5.2 Rotating chirp . . . . .	66
5.5.3 Microscopy . . . . .	67
5.5.4 Generalized sampling of the beating heart of the zebrafish under transmission microscopy . . . . .	69
5.5.5 Generalized sampling of the beating heart of the zebrafish on light-sheet fluorescent microscopy . . . . .	69
5.6 Conclusion . . . . .	71
<b>6 Multi-Spectral Widefield Microscopy of the Beating Heart through Post-Acquisition Synchronization and Unmixing</b>	<b>73</b>
6.1 Abstract . . . . .	73
6.2 Introduction . . . . .	74
6.3 Problem Statement . . . . .	76
6.4 Methods . . . . .	76
6.4.1 Temporal registration of movies acquired with different filters . . . . .	76
6.4.2 Spectral imaging/unmixing . . . . .	77
6.4.3 Calibration of the imaging system . . . . .	78
6.5 Results . . . . .	79
6.5.1 Experimental validation . . . . .	79
6.5.2 Spectral imaging of the beating heart of a zebrafish . . . . .	79
6.6 Discussion and Conclusion . . . . .	81
<b>7 Conclusions</b>	<b>83</b>
7.1 Main contributions of the thesis . . . . .	83
7.2 Further research outputs . . . . .	84
7.3 Proposed Future work . . . . .	85
7.4 Final words . . . . .	87
<b>A Derivation of the Alternating Direction Method of Multipliers for temporal super-resolution</b>	<b>89</b>
A.1 Introduction . . . . .	89
A.2 Alternating direction method of multipliers . . . . .	89
A.3 ADMM applied to the temporal super-resolution problem of Chapter 4 . . . . .	90
A.3.1 LASSO-formulation of the problem . . . . .	90
<b>B Constrained <math>\ell_1</math>-norm minimization with linear programming</b>	<b>93</b>
<b>Bibliography</b>	<b>95</b>
<b>Curriculum Vitae</b>	





# List of Figures

1.1	Light-sheet microscopy principle illustrated. We have our own at Idiap . . . . .	4
1.2	Development stages of a zebrafish . . . . .	5
2.1	Rayleigh criterion illustrated . . . . .	12
2.2	PSF illustration . . . . .	12
2.3	Different types of resolution involved in optical microscopy (spatial, temporal and spectral) . . . . .	13
2.4	Interpolation, rebinning and super-resolution illustrated in the case of a moving object . . . . .	15
2.5	Green fluorescent protein absorption and emission spectra . . . . .	17
3.1	Hue-encoded shutter principle schematic illustration . . . . .	19
3.2	Hue-encoded shutter principle illustrated with an example . . . . .	23
3.3	Validation of the hue-encoded shutter method with a moving resolution grid . . . . .	30
3.4	Hue-encoded shutter method can be calibrated with multiple models, which can be automatically selected at reconstruction . . . . .	33
3.5	Hue-encoded shutter method applied to the beating heart of a zebrafish in transmission microscopy . . . . .	34
4.1	Hue-encoded shutter principle schematic illustration . . . . .	39
4.2	Hue-encoded shutter principle for fluorescence light-sheet microscopy . . . . .	41
4.3	Fluo-HESM requires co-localized multi-color fluorescent labeling . . . . .	43
4.4	Fluo-HESM forward matrix illustrated . . . . .	46
4.5	Fluo-HESM allows simultaneous fast imaging of the beating heart and color imaging of its surroundings. . . . .	50
4.6	A static region is required to calibrate fluo-HESM. . . . .	51
4.7	Fluo-HESM is robust to fluorescence labeling inhomogeneities thanks to the temporal $\ell_1$ regularization . . . . .	53
5.1	Generalized sampling compared with naive sampling when applied to the schematized heart . . . . .	58

## List of Figures

---

5.2	A signal in B-spline representation has two equivalent representations, using basic and dual B-splines . . . . .	61
5.3	Illumination functions to generate B-spline prefilters . . . . .	62
5.4	Generalized sampling simulation of a signal made of B-splines of degrees 0 to 3	65
5.5	Generalized sampling of a chirp signal . . . . .	66
5.6	Rotating grid for real chirp experiment . . . . .	68
5.7	Generalized sampling of a zebrafish beating heart with transmission microscopy	70
5.8	Generalized sampling of a zebrafish beating heart with transmission microscopy	71
6.1	Spectral imaging of the schematized beating heart . . . . .	74
6.2	Overview of our multispectral imaging method for repeating processes . . . . .	75
6.3	Various setup configurations for multispectral imaging, multiple filters, a camera and a spectrometer are required . . . . .	77
6.4	Experimental validation of our multispectral method, we compare reconstructed spectra of the same sample, comparing static and dynamic acquired data . . .	80
6.5	Multispectral imaging of the zebrafish beating heart . . . . .	81
7.1	U-Net convolutional neural network adapted for regression . . . . .	86

# 1 Introduction

## 1.1 Optical microscopy

Optical microscopy is an essential tool used in many disciplines since the end of the sixteenth century<sup>1</sup>. I give hereafter a brief history of optical microscopy with a focus on techniques that are relevant to my thesis and purposely omit techniques that do not directly relate to my work.

The first reference to a compound microscope<sup>2</sup> dates back to 1595 and is attributed to Hans and Zacharias Jansen, while the origin of microscopy is attributed to Robert Hooke and Antonie van Leeuwenhoek [1].

Microscopy was intended to see objects invisible to the naked eye, by zooming in on those objects. However, there is a limitation to the zooming factor: diffraction. When light passes through a slit, or a lens, it is diffracted, creating *Airy discs*, as observed by George Airy [2] and formalized by Ernst Abbe [3]. Abbe stated that, given two points light-sources, the minimal distance  $d$  between them to distinguish them is limited by the wavelength of the light and cannot be smaller than half the wavelength. This later became the famous *Abbe's limit*:

$$d = \frac{\lambda}{2n\sin(\theta)} = \frac{\lambda}{2NA}, \quad (1.1)$$

where  $\lambda$  is the wavelength,  $n$  is the refractive index of the medium and  $\theta$  is the half-angle of the converging light cone. NA is the *numerical aperture*, a crucial property of all optical lenses that indicates the attainable resolution. Later on, Lord Rayleigh devised a criterion based on diffraction interferences (known as the *Rayleigh criterion*) stating that “*two point sources are regarded as just resolved when the principal diffraction maximum of one image coincides with the first minimum of the other*” [4].

---

<sup>1</sup>This brief historical introduction to microscopy is largely based on [1].

<sup>2</sup>A compound microscope consists of at least two lenses with matching focal planes. Single magnifying glasses existed already around the year 1000.

## Chapter 1. Introduction

---

Aware of the diffraction limit, scientists continued research on microscopy and the first fluorescence microscope was built by Auguste Köhler, using a UV illumination and relying on autofluorescence. He used darkfield illumination to make sure all the captured light was emitted from the sample. Köhler is still known to all users of optical microscopes as he devised an illumination method, called *Köhler illumination*, over a century ago that is still widely used [5].

The later development of the first fluorescent staining for live tissue (called *fluorochromes*) and dichromatic mirrors further pushed the capabilities of microscopes and made them accessible and universal instruments for biology. From then on, fluorescence microscopy made the imaging of live cell routine. In the 1960s, the first use of fluorescent antibodies was described by Albert Coons, which permitted, notably, the visualization of streptococci bacteria [6, 7].

At the same time, researchers introduced a new method, patented by M. Minsky in 1957 [8], to increase the contrast and resolution of images by cutting off out of focus light reaching the detector, a well established method now called confocal microscopy [9, 10, 11, 12]. Modern confocal microscopes block the out-of-focus light with a pair of pinholes and measure a point-wise light intensity. Spatial scanning of the sample is required to form a full image.

One of the latest microscopy methods introduced, which is of particular relevance to this thesis, as we built our own version of it for data acquisition, is *light sheet fluorescence microscopy* (LSFM), also referred to as *selective plane illumination microscopy* (SPIM), introduced by Voie et al. in 1993 [13], which brings excellent sectioning ability along the Z-axis (the optical axis of the detection axis), low laser exposition to the sample, which reduces photo-damages and allows for fast imaging. While Voie continued his research on light-sheet microscopy [14, 15], almost simultaneously and independently from one another, Ernst Stelzer's group also developed a light-sheet microscope [16, 17, 18]. In LSFM, the illumination light-sheet is commonly generated thanks to a cylindrical lens, perpendicularly to the detection axis. This way, only the imaged plane within the sample is subjected to laser illumination reducing background signal and permitting great optical sectioning while reducing photo-damage. Figure 1.1(top) shows the principle of the light-sheet formation. Although the first fluorescence light-sheet microscope is attributed to Voie et al., in 1902 Siedentopf and Zsigmondy presented the very first light-sheet microscope to observe particles of gold, where sunlight was projected on the sample through a slit [19, 20]. Later on, light-sheet microscopy was widely popularized by Jan Huiskens, working in Stelzer's group at the time [21, 22, 23]. Among others who improved the LSFM capabilities [24, 25, 26, 27, 28], Philipp Keller, also from Stelzer's group at the time, introduced a new kind of light-sheet called digital scanned laser light sheet microscope (DSLIM) [29, 30, 31] where the excitation light sheet is not made by a cylindric lens, but by rapidly scanning the sample with a laser beam. Various open source projects made the build and control of a microscope accessible [32, 33, 34, 35, 36] and we particularly took advantage of

the OpenSPIM project [33]. Figure 1.1(bottom) shows a picture of the light-sheet microscope that I built during my thesis, at the Idiap Research Institute.

So far, optical microscopy was diffraction-limited, that is, the highest achievable resolution was about half the wavelength of the light (typical resolution of 200 nm). Hell and Stelzer were the first to go below the diffraction limit with their stimulated emission-depletion microscope (STED) [38, 39] and others soon improved on the technique [40, 41]. Later on, Betzig et al. presented photoactivated localization microscopy (PALM) [42], while almost simultaneously Rust, Bates and Zhuang introduced stochastic optical reconstruction microscopy (STORM) [43] and Hess et alia introduced fluorescence photoactivation localization microscopy (FPALM) [44]. All of these methods allow us to distinguish single molecules by leveraging specially designed fluorophores that emit light at random times. Acquisition of multiple images that are combined together enable to perform single molecule localization microscopy, going way beyond the diffraction limit and achieve by far the highest spatial resolution obtainable on optical microscopes (best lateral resolution 10 nm). However, these techniques only work on fixed samples, as multiple images are acquired and fused together, assuming no motion in the sample.

## 1.2 Motivations and contributions

In this thesis, we set out to increase both temporal and spectral resolution for optical microscopy. Moreover, the available operating modes on most microscopes tend to lack flexibility as they usually focus on one type of resolution, most frequently the spatial resolution, at the expense of other kinds of resolution. For example, point-scanning confocal microscopy requires scanning of the sample, allowing a high spatial resolution but has a low temporal resolution. One may wonder whether there is a real need for even sharper, more colored, faster videos for microscopy, or for more flexibility.

In fact, there is substantial need. As medicine and developmental biology advance, the needs to see smaller details, faster motions and subtler colours keep rising. To illustrate this need, let us mention the concerning example of congenital heart defects amongst humans. 1% of newborn infants in the United States carry a congenital heart defect [45], and about 25% of them are critical [46], which is the leading cause of death at birth in the United States. In order to understand, diagnose and possibly treat these heart malformations beforehand, developmental biologists extensively study the zebrafish heart development. The zebrafish is close to being a perfect model as (i) zebrafish are vertebrates and the first stages of their heart development is very similar to that of humans [47], (ii) zebrafish can be bred easily and quickly, (iii) embryos are naturally transparent up to a few days of development and can be made transparent over longer periods using well-established techniques [48, 49, 50, 51], (iv)

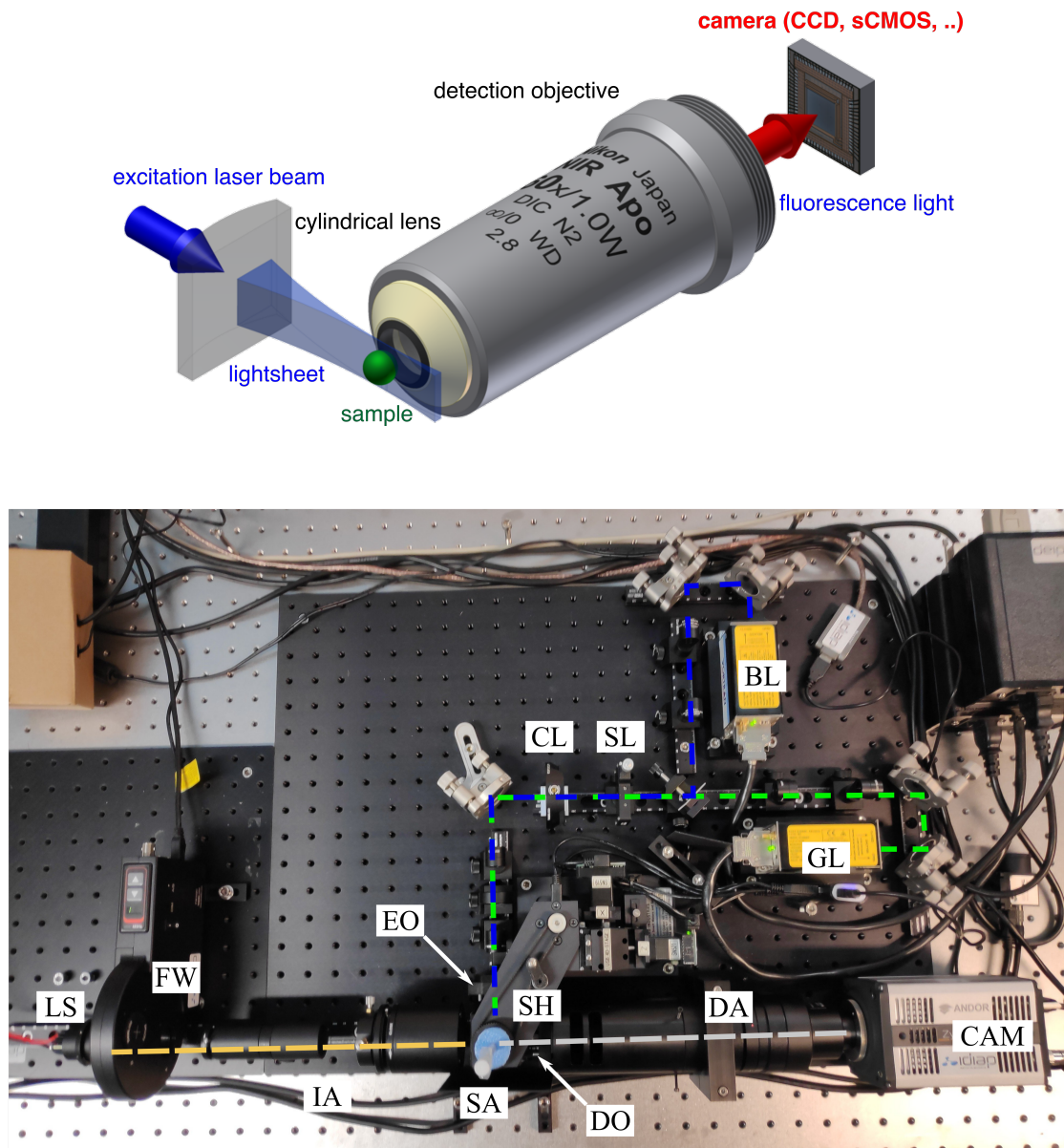


Figure 1.1 – Light-sheet microscopy illustrated. (top) Light sheet formation principle: an excitation laser beam is transformed into a thin light sheet using a cylindrical lens. The detection axis is perpendicular to the excitation axis. Image from [37]. (bottom) Our light-sheet microscope implementation, based on the OpenSpim initiative [33]. The camera (CAM) is visible on the bottom right of the image. We have a light-sheet illumination with two lasers, a 488 nm blue laser (BL) and a 561nm green laser (GL). They both pass through a slit (SL) and a cylindrical lens (CL) and are then focused on the sample (SA) held by the sample holder (SH) thanks to the excitation objective (EO). The path of both lasers is shown with the green and blue dashed lines. The detection objective (DO) then focuses the image from the sample at infinity within the detection axis (DA) and the image is formed on the camera sensor with an additional lens. We added a transmission illumination arm (IA) where a light source (LS) can be spectrally modified or dimmed using a filter wheel (FW). Two additional filters can be mounted on the detection axis (DA).

## 1.2. Motivations and contributions

they can be genetically engineered to express fluorescent proteins in specific cell types, and (v) they have the ability to regenerate their hearts when damaged [52, 53]. Figure 1.2 shows images of zebrafish embryos at various developmental stages.

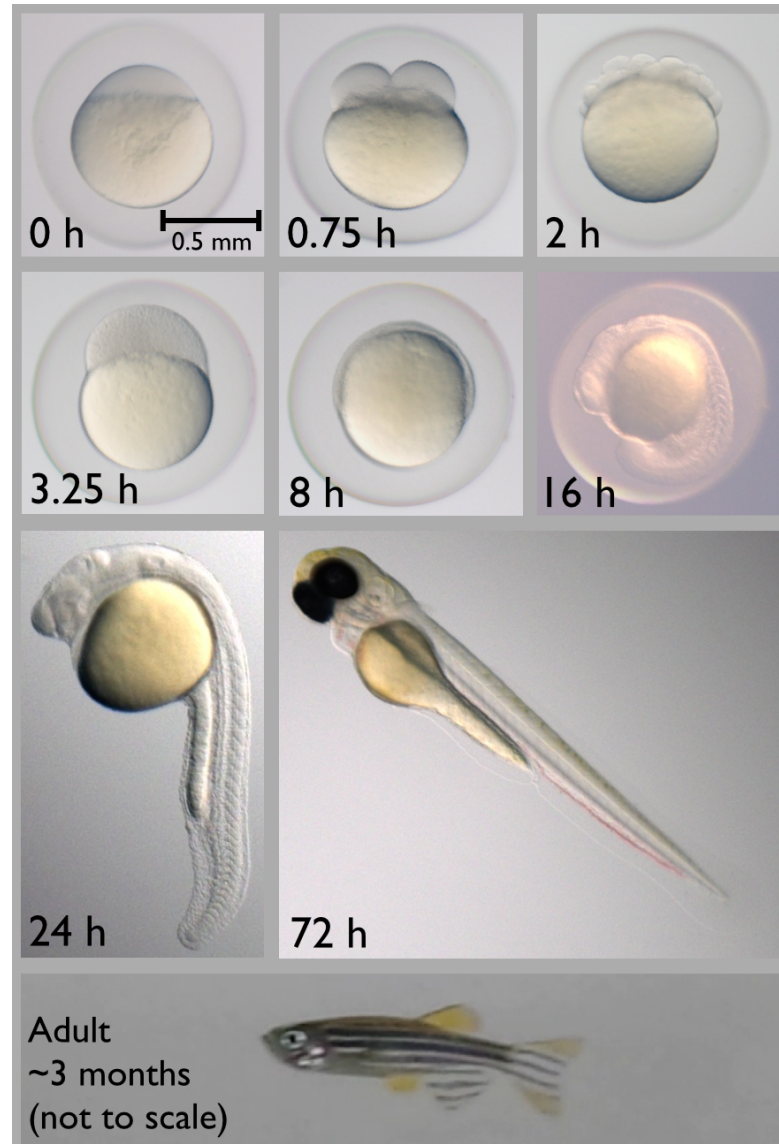


Figure 1.2 – Various stages of zebrafish embryo development. Image from [54] with kind permission of Ed Hendel.

In this thesis we focus on increasing the temporal and spectral resolutions of imaging methods for microscopy, as well as on how to improve the flexibility of microscopes.

### 1.2.1 Fast imaging and spectral imaging are ubiquitous in many areas

There are many fast and colorful processes that one may need to observe. An interesting example is imaging of live samples in biology. Live processes being mostly dynamic, observing live samples requires imaging systems that allow for fast enough imaging. For example, cell migration tracking, organ morphogenesis, and cellular dynamics, all require fast imaging. Moreover, to track these processes various color markers can be used and color carries important information. In the case of fluorescence microscopy, if a sample is labelled with multiple fluorescent protein types (called fluorophores), the ability to distinguish them is of paramount importance as it allows, for instance, separation of morphological features. In the case of transmission microscopy, color also helps to distinguish various features and can provide quantitative information, such as the oxygenation level of haemoglobin.

High resolution imaging is not limited to biology. Medical imaging also routinely relies on imaging. Diagnostics are frequently based on images. For instance, when a doctor inspects a growing foetus in its mother's womb ultra-sound imaging allows for dynamic imaging. In the case of brain surgeons, functional neuro-imaging is frequently used to diagnose any dysfunction in the brain. This imaging technique (techniques rather) is still under development, and is yet another example demonstrating the need for fast imaging. When imaging a heart to diagnose patients with short breath or chest-pain, echocardiography is used, and once again fast imaging is needed.

While our examples show how much fast imaging is needed for medical and biological applications, needs for fast imaging also exist in many other fields. In entertainment, examples include slow-motion replay of a football goal, which requires high-speed footage to be dramatic or slow-motion in movies (for example, the famous bullet-effect in the movie "Matrix"). Most smartphones allow acquiring images at a high frame-rate (up to 240 fps for the high-end ones at the time of writing this thesis).

Industrial applications also often make use of fast and spectral imaging, and there are countless examples in this area. When a car company does its crash-tests, it relies on a variety of sensors and, in particular, on high-speed imaging of the crashes. In the food industry, it is standard practice to do spectral imaging of fruits and vegetables for non-destructive inspection and detection of rotten or spoiled goods before they reach the consumer shelves. Companies building high-speed assembly lines often resort to ultra-high speed (more than 10'000 frames per second) cameras to analyze vibrations in the machines. Likewise, robots are frequently imaged at high speed, to look for vibrations and deformations.



### 1.2.2 What is the problem with the current instrumentation?

Although fast imaging solutions already exist for many applications, they often have general limitations such as requiring faster data transfer, imposing higher memory requirements, and more constraining, imposing a low exposure time to accommodate the high frame rate. Short shutter times limit the number of photons accumulating on the sensor, thus leading to a low signal-to-noise ratio (SNR). The usual solution to the latter problem is to increase the illumination power, but this cannot be done in all applications. In fluorescence microscopy, the number of photons emitted by the fluorophores can only be increased up to a certain point, after which photo-bleaching occurs. Moreover, live biological samples are sensitive to light and increasing the illumination intensity damages them.

Furthermore, as the magnification increases, motions are amplified as well, thereby increasing the observed motion blur, which is often the limiting factor in dynamic microscopy [55]. Fast imaging may then be a solution to reduce motion blur.

Moreover, sensitive cameras are usually slow and expensive. When color is needed, color cameras often sacrifice spatial resolution for spectral resolution, while images of both high spectral and spatial resolutions may be needed. Another limitation of many color cameras is that they only capture 3 hues.

In order to conduct developmental biology studies, light imaging is a tool of paramount importance. This is the *raison d'être* of this thesis: our goal is to develop methods to push further the temporal and spectral resolutions of existing light microscopes, as well as increasing their flexibility of use.

## 1.3 Related work

There are three main axes along which this thesis relates to existing works: (1) temporal super-resolution for imaging, (2) spectral imaging and (3) the use of active illumination for imaging. We give an overview here of the major methods and latest developments, which will be complemented further in each chapter of the thesis.

To increase the temporal and spatial resolution beyond what cameras can offer directly, the most common paradigm is to rely on multiple simultaneous (or parallel) observations of a signal, which are fused together to reconstruct a high-resolution version of the signal of interest [56, 57, 58, 59].

Another frequent means to do super-resolution is making assumptions about the signal itself. For instance, put forward by the extensive research on compressed sensing [60, 61, 62, 63, 64, 65, 66], one may leverage the fact that the signal has a sparse representation in a function basis

and reconstruct signals from fewer measurements than dictated by the Shannon-Nyquist criterion [67, 68, 69, 70, 71, 72]. Also, relying on the repeatable nature of the imaged motion can be taken advantage of to increase the resolution of acquired images [73, 74].

Some approaches use custom-made optical setups or cameras, together with computational methods to increase the temporal resolution [75, 76]. Generally speaking, we avoided using custom-made hardware as it makes the research results harder to reproduce and further distribute.

Controlled illumination is a core aspect of any optical microscope's performance, as demonstrated by Köhler over a century ago [5]. In particular, structured illumination has been proposed as a way to access high-frequency components of the object via multiple modulations [77, 78, 79, 80, 81, 82, 83, 84]. Using controlled lasers, it is possible to gain access to multiphoton microscopy [85, 86]. Multiphoton microscopy allows fast imaging of deep tissues [87] and as well as multispectral imaging [88, 89].

Spectral imaging recently gained in popularity in microscopy, due to the substantial amount of information that color carries [90, 91, 92, 93]. Specific to fluorescence microscopy in the presence of multiple fluorophores types, linear unmixing permits to distinguish various fluorophores with overlapping spectra [94, 95].

Due to the high potential of spectral imaging as a quantitative method, there have been many recent developments to spectral imaging [96, 97, 98, 99, 100, 101, 102, 103]. Using special probes whose spectrum depends on physical properties [104], measuring spectral information can provide physiological functional information [105].

### 1.4 Organization of the thesis

This thesis is organized as follows. In Chapter 3 we introduce a method that enables temporal super-resolution imaging by exchanging color and temporal information. The method uses a color camera as well as an active multispectral illumination to encode temporal information in the hue of the captured images. We recover the temporal information through a computational procedure (solving an inverse problem). We show applications of our method in transmission microscopy, imaging the beating heart of a zebrafish embryo. This method allows us to rapidly switch between fast imaging and color imaging, and to do both simultaneously in different regions of interest.

We extended the method of Chapter 3 in Chapter 4 by adapting the method to fluorescence microscopy. We first highlight the important differences between transmission microscopy and fluorescence microscopy, notably that the light spectrum captured by the camera cannot

be modified in the case of fluorescence microscopy, as fluorescent proteins have a fixed light emission spectrum. We then present an application of the method to the beating heart of a live zebrafish which co-expresses ubiquitous cytoplasmic green fluorescent protein (EGFP) and red fluorescent protein (mCherry). Since fluorescent labelling can be inhomogeneous, we show how to select a static calibration area and devise a new algorithm to be more robust to slight model mismatches. The derivation of the algorithm is given in Appendix A.

In Chapter 5, we introduce a method to implement temporal generalized sampling as introduced by Unser in [106]. We take advantage of the spectral unmixing procedure of Chapter 3 to compute multiple inner products simultaneously. Based on these inner products we can pre-filter the sampled signal to perform optimal sampling in a B-spline basis. We use an equivalent dual B-spline representation of the signal [107] to have finite-length pre-filters as well as signal representation basis.

We proceed in Chapter 6 where we focus on spectral super-resolution of fast repeating processes. We introduce a method to do spectral imaging of a beating heart (or any repeating process). Our method relies on the sequential acquisition of multiple movies of the beating heart, using various filters in the illumination, a post-acquisition time synchronization procedure and solving of an inverse problem to retrieve a spectral movie of the beating heart.

We finally conclude in Chapter 7 where we summarize the contributions of this thesis and present possible future work directions.



## 2 Prerequisites

We briefly remind a few concepts to the reader that will be helpful for the comprehension of the subsequent dissertation.

### 2.1 Concepts of resolution, sampling and super-resolution

#### 2.1.1 Resolution

Generally speaking, the resolution can be defined as the smallest observable change. More formally, as previously quoted, to characterize the lateral resolution of an optical system, Rayleigh's criterion states that “*two point sources are regarded as just resolved when the principal diffraction maximum of one image coincides with the first minimum of the other*”, so the minimal resolvable distance between two point sources is

$$d = \frac{1.22\lambda}{2NA}. \quad (2.1)$$

Figure 2.1 illustrates this criterion in the case of two point-sources that are first impossible to distinguish (Fig. 2.1(a)), just resolved ((Fig. 2.1(b)) and well resolved ((Fig. 2.1(c)).

In optics, systems are characterized by their *point spread function* (PSF), which is a system's impulse response function to a point-source. When using coherent light, the PSF of a point-source is that given in Figure 2.1(c) for a single source. Figure 2.2 illustrates the effect of the (spatial) PSE, in the case of a Gaussian PSE.

Optical microscopy involves three kinds of resolution: (i) spatial, (ii) temporal and (iii) spectral resolutions. Figure 2.3 displays cartoonized examples of a beating heart with low spatial (top), spectral (bottom right) and temporal resolution (bottom left).

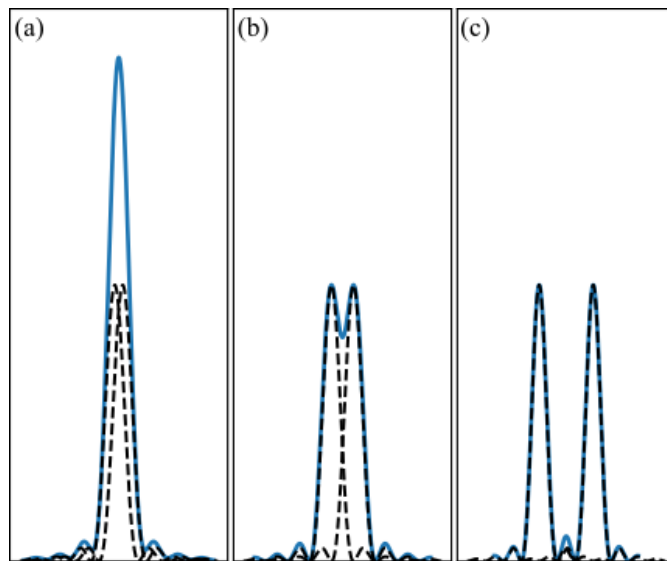


Figure 2.1 – Rayleigh criterion illustrated. (a) Two point-sources (dashed lines) are separated by less than the smallest resolvable distance and the resulting light intensity (blue) cannot be distinguished. (b) the same point-sources, when they are just resolved according to the Rayleigh criterion (2.1). (c) Two point-sources are well-resolved as they are separated by 3 times the critical distance.

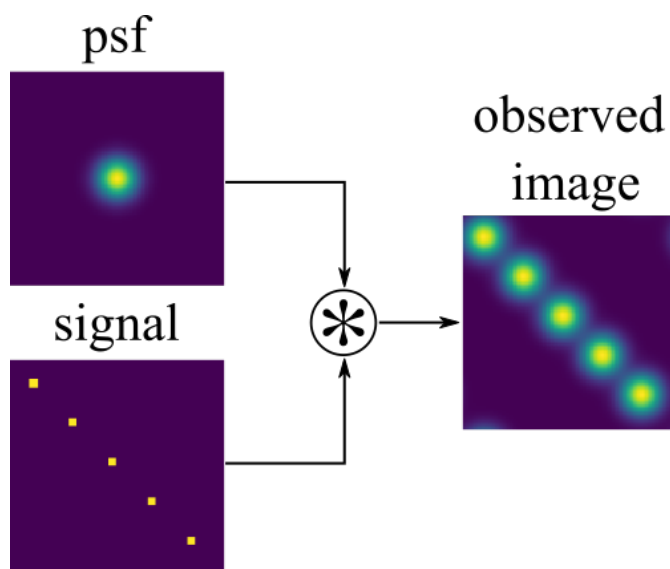


Figure 2.2 – PSF illustrated. When systems are linear shift-invariant (a general assumption in optical microscopy), the system's observation can be modelled by the original signal convoluted (shown with  $*$ ) with the PSF of the imaging system.

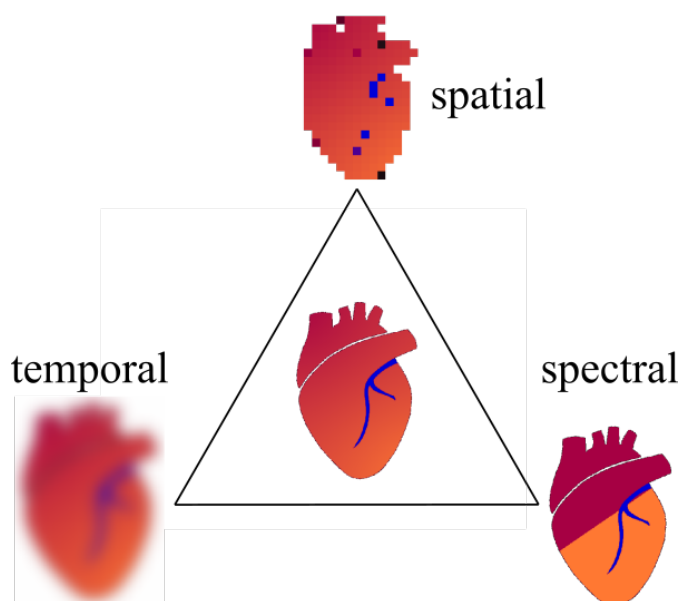


Figure 2.3 – Three kinds of resolution are involved in microscopy: (i) spatial, (ii) temporal and (iii) spectral. This thesis focuses on temporal and spectral resolution. The figure illustrates a schematized low spatial resolution image of a heart at the top, where the features of the heart are difficult to see and outline. Low temporal resolution is illustrated at the bottom left, where motion renders the image of the heart blurry. Low spectral resolution of the heart is shown at the bottom right, where instead of a color gradient from red to orange, there are only two distinct colours visible. In the middle of this triangle, a high resolution (spatial, temporal and spectral) image of the heart is sharp, fine structures as well as colours subtleties are visible.

- **Spatial resolution** of an imaging system: the smallest distance in the object plane at which two point sources produce distinguishable blobs in the image.
- **Temporal resolution**: the spatial resolution concept applies with events, two short flashes of light that can be distinguished as two separate events in a movie. The concept of resolution of an imaging system has a dual in the frequency domain (spatial or temporal) where the system's bandwidth may give an indication of its resolution.
- **Spectral resolution**: ability to resolve different spectral features, the smallest spectral difference (typically in wavelength, nm) between two distinguishable colors.

### 2.1.2 Sampling, a ubiquitous concept

To complete our introduction to resolution, we briefly describe sampling. Sampling is required to capture real-world signals, which are continuous signals by essence, and translate them into discrete sequences of numbers, called samples, which computers can manipulate.

Claude Shannon laid the foundation of sampling in his seminal paper back in 1949 [108] (see [109] for a reprint) stating that (Shannon-Nyquist theorem): “*if a function  $f(t)$  contains no frequencies higher than  $\omega_{max}$  (radian/second), it is completely determined by giving its ordinates at a series of points spaced  $T = \frac{\pi}{\omega_{max}}$  seconds apart*”. With this sampling theorem comes a reconstruction formula:

$$f(t) = \sum_{k \in \mathbb{Z}} f(kT) \text{sinc}\left(\frac{t}{T} - k\right), \quad (2.2)$$

where  $\text{sinc}(t) = \frac{\sin(\pi t)}{\pi t}$ . This theorem had a tremendous impact on the engineering communities of information theory, communications theory, and signal processing and is still widely used amongst practitioners. A common way to model sampling is by multiplying the signal  $f(t)$  with a train of shifted Dirac impulse functions  $\sum_{k \in \mathbb{Z}} \delta(t - k)$ . Thus, the sampling process makes the signal representation in the frequency domain periodic (see [106]).

This theorem assumes the sampled signal to be band-limited, which never occurs in natural signals, as a finite support in the frequency domain implies an infinite support in the time domain. If the sampled signal does not respect the *Nyquist criterion* (if it has higher frequencies than  $\omega_{max}$ ), because of the periodization of the frequency spectrum, an overlap occurs in the sampled frequencies and the signal is reconstructed with errors. This overlapping is called *aliasing*. The standard practice for sampling to avoid aliasing is the following: (1) apply low-pass filter to cut off all frequencies higher than  $\omega_{max}$ , (2) sample filtered signal with train of Diracs, (3) reconstruct continuous signal with the sinc function. As we will see later on, this approach suffers from the fact that perfect low-pass filters cannot be implemented in practice.



## 2.1. Concepts of resolution, sampling and super-resolution

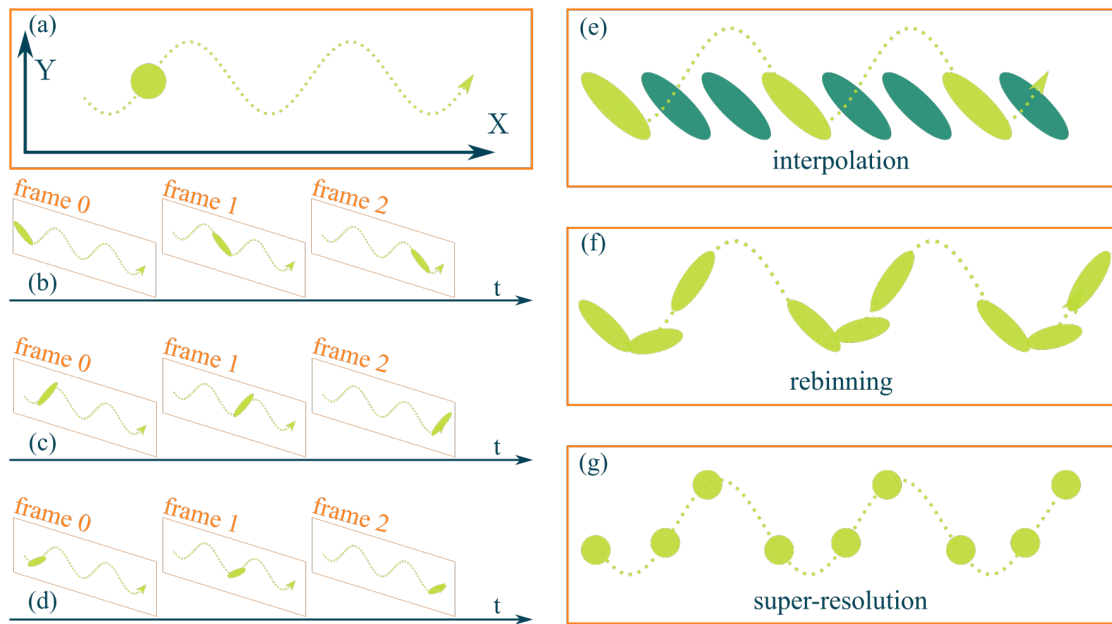


Figure 2.4 – Illustration of the concepts of interpolation, rebinning and super-resolution applied to the imaging of a moving object. (a) A round object moves in the XY plane along a sinusoidal trajectory displayed with a dashed line. (b)-(d) Images acquisition of the moving object using three imaging systems that have the same frame-rate but a temporal shift. Notice that the round object becomes elliptic, due to the motion blur. (e) Interpolation over time by using the frames acquired in (b). Notice that the ball seems to follow a straight line, due to aliasing. (f) Rebinning of all acquired frames on (b)-(d). This time the trajectory of the moving object is apparent but there is still motion blur. Moreover, the sampling rate of the rebinned sequence is not constant. (g) Super-resolution over time of the frames acquired in (b)-(d). The object is, again, round, its trajectory is visible and the sampling rate is constant.

### 2.1.3 Introduction to super-resolution

In this thesis, we seek ways to improve temporal and spectral resolutions thus improving the resolution beyond the capability of the instrument hardware by itself.

With this definition, let us introduce two more notions:

- **Interpolation:** is a method to estimate data points in between sampled data, thus it creates new data based on the measurements. This method is illustrated on Figure 2.4(e).
- **Rebinning:** when there are multiple measurements of the same dynamic sample, rebinning is the process of re-aligning all measurements on a single time serie. This process is illustrated on Figure 2.4(f).

### 2.1.4 Comparison of super-resolution with binning or interpolation

Sometimes, super-resolution is mistaken with interpolation or signal rebinning, but, as defined earlier, there are fundamental differences shown on Figure 2.4. Figure 2.4(a) presents a dynamical object that we are interested in imaging at high time-resolution. Figure 2.4(e),(f) show the effect of interpolation and rebinning respectively, while Figure 2.4(g) shows what we mean by temporal super-resolution.

When doing temporal interpolation, it is possible to increase the number of frames per second, but the interpolated signal remains subject to temporal aliasing. Figure 2.4(e), shows the result of temporal interpolation on the data acquired in Figure 2.4(b).

Signal rebinning allows to produce aliasing-free signal, as it actually increases the sampling rate, but has the major drawback that it does not handle motion blur, as shown on Figure 2.4(f).

When performing temporal super-resolution, motion blur will naturally be handled, even without any knowledge of the movement itself, since it is an artefact of the limited time-resolution of the imaging system (exposure time).

With temporal super-resolution, we intend to reduce both aliasing and motion blur, as shown on Figure 2.4(g).

## 2.2 Fluorescence microscopy

In Section 1.1 we already mentioned fluorescence microscopy, one of the most useful tools in every biologist's toolbox. It is possible to have fluorescence light emitted by a sample from specific biological features such as nuclei, membranes or selected molecules [110]. The light emission from specific molecules allows imaging small concentration of molecules with a good signal-to-noise ratio [111].

Fluorescence microscopy works by attaching fluorescent proteins called *fluorophores* (sometimes also called *fluorochromes*) to chosen molecules on a (possibly live) sample. These proteins absorb a certain light spectrum (called the *absorption spectrum*) and emit another light spectrum (the *emission spectrum*). The emission spectrum is always different than the absorption spectrum, due to the Stoke's shift [112], the emitted light has always a higher wavelength (lower frequency) than the excitation light. This shift is taken advantage of, as the excitation light can be cut off by an optical filter, the emitted light is not filtered out and can be captured on a camera.

Figure 2.5 shows the light absorption and emission spectra for a typical fluorophore, the EGFP [113], a variant of the Green Fluorescent Proteins [114, 115, 116].

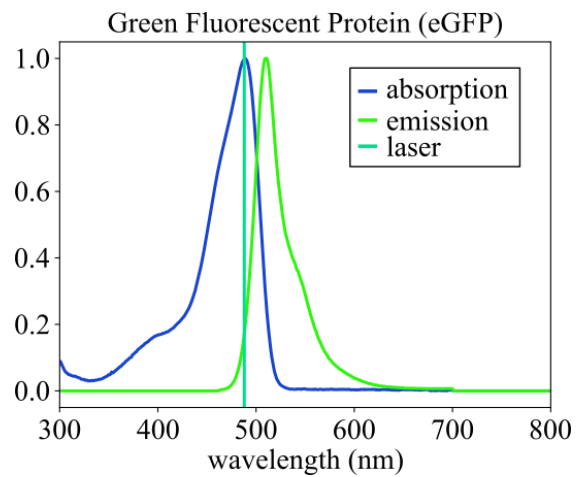


Figure 2.5 – Green fluorescent protein (GFP) absorption and emission spectra. A 488 nm laser is also shown, as it is typically used as the excitation light source for GFPs. The absorption spectrum shows a measure of the probability of absorbing the excitation light as a function of the wavelength, this is called the *cross-section* of the fluorophore.



# 3 Hue-Encoded Shutter Method for Temporal Super-Resolution Microscopy

This chapter is directly based on our publication in [117]. This paper is also the subject of a European patent application (application number EP19154253). The authors of the paper are myself, Emmanuel Pignat, Sylvain Calinon and Michael Liebling. M. Liebling and I had the original idea of the method and implemented it. E. Pignat supported me for the experiments involving robotic arms in Sections 3.5.2, 3.5.3 and 3.5.4. He also made suggestions regarding the implementation of the calibration method in Section 3.4.2, using Tensorflow. S. Calinon is the head of the *Robot Learning and Interaction Group* at the *Idiap Research Institute*, he is the thesis supervisor of E. Pignat. M. Liebling and I wrote the draft of the manuscript and all authors discussed the results and contributed to the final manuscript.

To better locate this paper in the context of the whole thesis, Figure 3.1 illustrates the effect of the method when applied to the schematized heart of Figure 2.3.

## 3.1 Abstract

Limited time-resolution in microscopy is an obstacle to many biological studies. Despite recent advances in hardware, digital cameras have limited operation modes that constrain frame-rate, integration time, and color sensing patterns. In this paper, we propose an approach

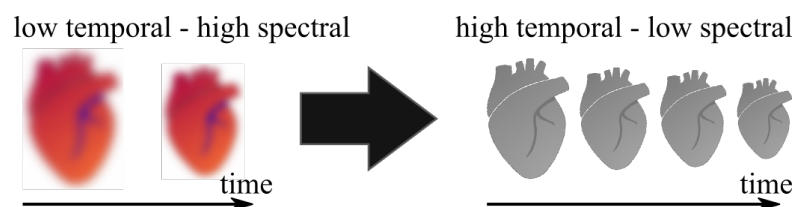


Figure 3.1 – The method presented in this chapter exchanges spectral for temporal information, allowing to increase the frame-rate by a factor 3 while reducing the color from 3 to 1 channel.

to extend the temporal resolution of a conventional digital color camera by leveraging a multi-color illumination source. Our method allows imaging single-hue objects at increased frame-rate by trading spectral for temporal information (while retaining the ability to measure base hue). It also allows rapid switching to standard RGB acquisition. We evaluated the feasibility and performance of our method via experiments with mobile resolution targets. We observed a time-resolution increase by a factor 2.8 with a three-fold increase in temporal sampling rate. We further illustrate the use of our method to image the beating heart of a zebrafish larva, allowing the display of color or fast grayscale images. Our method is particularly well-suited to extend the capabilities of imaging systems where the flexibility of rapidly switching between high frame rate and color imaging are necessary.

### 3.2 Introduction

Many biological processes are highly dynamic and a low time-resolution in microscopy seriously limits their study [55]. Several recent developments in both illumination and detection technology allow pushing towards higher frame rates. Light emitting diodes (LEDs), which are bright yet emit little heat, are both cost-effective and reliable [32]. Several open-source projects have made building custom microscopes increasingly accessible [32, 33, 34] and facilitated hardware control outside of standard operating modes [35, 36]. Despite these developments, many imaging setups remain constrained by the achievable frame-rate, integration time, and color sensing patterns, because digital cameras have limited operation modes.

In this paper, we propose to extend the temporal resolution of a conventional digital color camera (whose frames can be externally-triggered) by leveraging a multi-color LED illumination source and computational post-processing. Our method assumes that the observed object is of a single hue (such as obtained by use of a single stain or dye) and embeds time information into each acquired frame by spectrally encoding temporal light patterns that are then collected by a color camera. Following acquisition, the images undergo an unmixing procedure that increases the frame-rate and effective temporal resolution. Our approach is related or combines approaches leveraged for other imaging methods, which we briefly review below.

To increase the (temporal and spatial) resolution beyond what cameras can offer directly, several computational approaches have been proposed, often relying on multiple simultaneous observations of a signal, which are then fused to reconstruct a high-resolution version of the signal of interest [56, 57, 58, 59]. Despite the resolution gains, these methods require availability of multiple cameras, which can be hard to integrate in a standard microscopy setup, or which may not be compatible in low photon count situations. Other methods make assumptions on the signal structure itself, for instance assuming the signal has a sparse representation

in a function basis [71, 72, 69] or relying on the repeatable nature of the imaged motion [73, 74]. Alternative approaches, which require no prior assumptions include a method by Bub et al. [75], who proposed using a modified camera, whose pixels have staggered exposure times, which allows for a flexible tradeoff between time and spatial resolution. This method offers great possibilities for microscopy, yet with the drawback that it requires a modified camera, requiring low-level hardware control.

Controlled illumination is a core aspect of any optical microscope's performance, as demonstrated by Köhler over a century ago [5]. In particular, structured illumination has been proposed as a way to access high-frequency components of the object via multiple modulations [77, 78, 79, 80, 81]. The modulated signals are combined computationally, and numerical methods have focused on aspects such as taking into account experimental artefact [82], performing structured illumination without precise knowledge of the projected pattern [83], or lowering the number of required images [84]. Our proposed method leverages ideas from structured illumination, albeit in the temporal domain. Our method also relies on unmixing spectrally encoded signals, which bears similarities with multi-spectral unmixing in fluorescence microscopy [95].

In order to improve temporal resolution and reduce motion blur, several methods have been proposed that take advantage of the availability of controllable illumination sources driven by rapid controllers that work in synchrony with the camera, followed by computational post-processing. For example, Staudt et al. [118] used short light pulses (stroboscopy) to reduce motion blur (while remaining limited by the camera frame-rate) when imaging the beating heart. Gorthi et al. [119] proposed a method for linear motion deblurring for fluorescence microscopy based on the *fluttered shutter* principle [120] by using a pseudo-random temporal illumination sequence, allowing to reduce motion blur by a factor of 50. This improvement is, however, only possible in the case of linear motions, which are common in cytometry, yet might not be applicable to more general biological motions.

Other active illumination methods have also been proposed in fields other than microscopy. Shiba et al. in [121] used an active illumination to project six dense dot patterns during an image acquisition duration and recover both depth and speed of elements in the imaged scene through computation. Rangarajan et al. in [122] presented active computational imaging methods to do spatial super-resolution as well as depth-estimation, via the projection of space-varying illumination patterns.

The main contributions of the present paper are:

1. a procedure to encode temporal details by illuminating each frame with colored light patterns;

2. a reconstruction method to achieve temporal superresolution based on the encoded measurements;
3. the characterization of our method's performance and its robustness both on synthetic and experimental data.

The paper is organized as follows: in Section 3.3 we present the signal and imaging models and detail the assumptions on the image acquisition and the signal. In Section 3.4, we derive our superresolution method and present a color calibration procedure to adjust the free parameters of our method and retrieve base hues. In Section 3.5 we characterize our method in terms of resolution gain and robustness and demonstrate its applicability for imaging biological samples in microscopy in Section 3.6. We discuss these results in Section 3.7 before concluding in Section 3.8.

### 3.3 Imaging Model

We consider an imaging system consisting of  $L$  co-located illumination light sources and a color camera with  $C$  color channels. We assume that the camera has a global shutter, meaning that each pixel collects light over the same, fixed interval of time. We further consider that each light source has a fixed spectrum while the overall intensity can be varied over the duration of the camera shutter time. The timing of the illumination is linked to the camera. The imaged scene is assumed to be of a single hue and the optical parameters are assumed to be constant over the field of view. Figure 3.2 schematically depicts an example arrangement for three illumination sources and a color camera with a Bayer pattern.

Our method operates on each pixel and each frame independently. We can therefore proceed with the derivation of our method by considering a single color pixel, denoted by the vector  $\mathbf{y} = (y_1, \dots, y_C)^\top$ , whose  $C$  color components can be modeled as:

$$y_c = \int_0^E \left( \sum_{\ell=1}^L \gamma_{\ell,c} x(t) s_\ell(t) \right) dt + d_c \quad (3.1)$$

$$= d_c + \sum_{\ell=1}^L \gamma_{\ell,c} \int_0^E x(t) s_\ell(t) dt, \quad (3.2)$$

where  $x(t)$ ,  $t \in [0, E]$  is the imaged time signal (which we wish to recover) at the location in the scene corresponding to the pixel,  $E$  is the exposure duration,  $s_\ell(t) \in \mathbb{R}_0^+$  is the intensity function of the  $\ell^{\text{th}}$  active light over time,  $d_c \in \mathbb{R}_0^+$  is an electronic bias for channel  $c$  and  $\gamma_{\ell,c} \in \mathbb{R}_0^+$  is the spectral impact of the  $\ell^{\text{th}}$  light source on channel  $c$ . Within the duration of one movie frame,



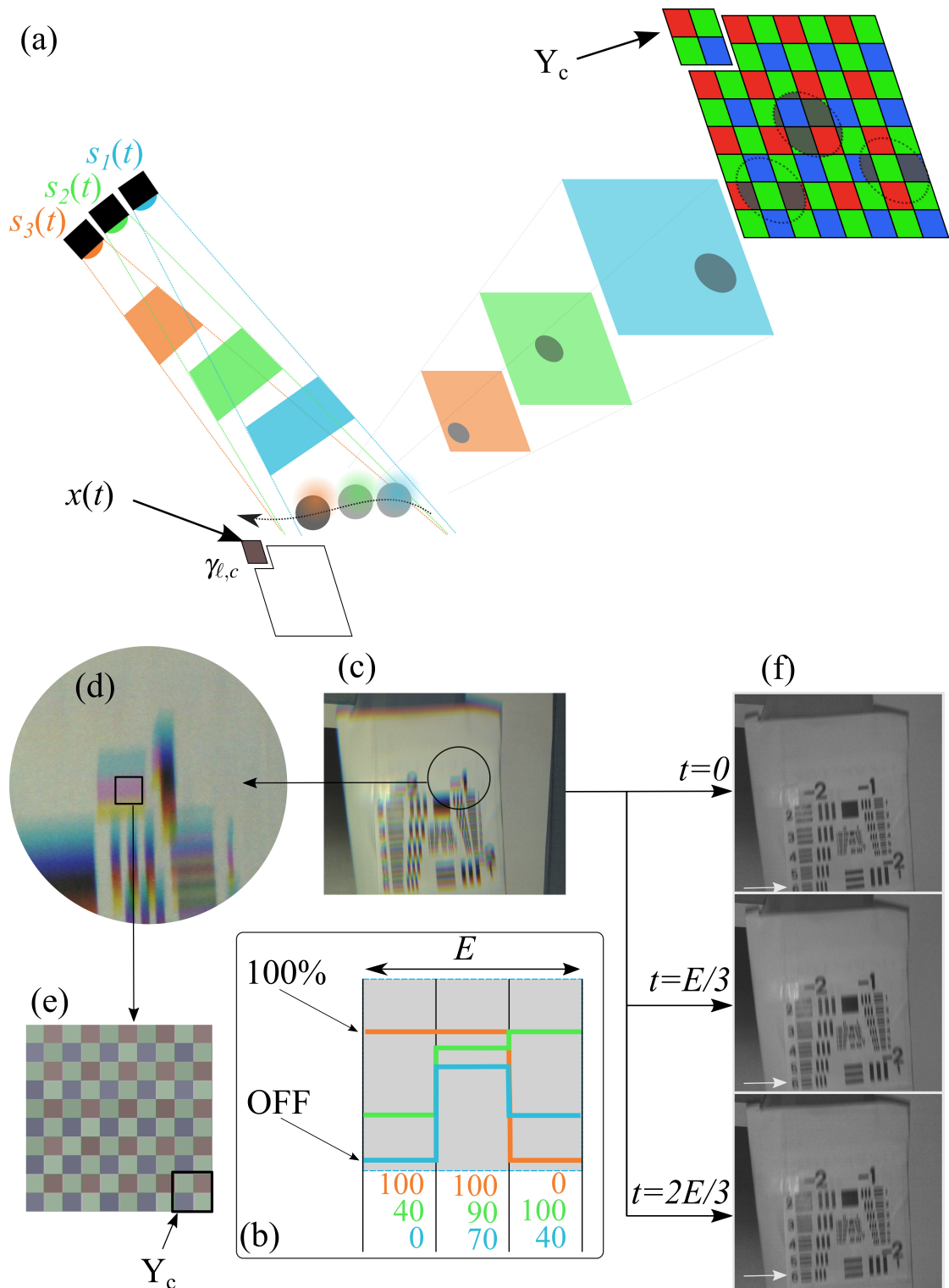


Figure 3.2 – (a) Acquisition setup. The moving sample is imaged with three active light sources  $s_i(t)$ . The projection of the scene to the camera is shown with  $x(t)$ . The color (Bayer) filter makes each pixel sensitive to a specific spectrum that is independent of the light sources. Each light source has its own time function, capturing the sample at different times and encoding this information in different spectra which is then captured by the color sensor in the hue domain. (b) Example of possible temporal functions for the three light sources. (c) Real example of acquired data with the depicted system of (a). (d)-(e) Close-ups to the real acquired data, the Bayer filter is visible. (f) Reconstruction of three grayscale frames from the acquisition shown in (c).

### Chapter 3. Hue-Encoded Shutter Method for Temporal Super-Resolution Microscopy

we model the imaged signal  $x(t)$  as a piecewise constant signal:

$$x(t) = \sum_{i=1}^Q x[i] \beta^0(Q \cdot (t - i)), \quad (3.3)$$

with  $Q$  an integer number of steps over the exposure time,  $x[i], i = 1, \dots, Q$ , the values of  $x(t)$  at each step, and

$$\beta^0(t) = \begin{cases} 1 & \text{if } 0 \leq t < \frac{E}{Q} \\ 0 & \text{otherwise,} \end{cases} \quad (3.4)$$

the causal B-spline of degree 0 (box function). Given this model for the signal  $x(t)$ , Equation (3.1) can be rewritten as:

$$\begin{aligned} y_c &= d_c + \sum_{\ell=1}^L \gamma_{\ell,c} \int_0^E \sum_{i=1}^Q x[i] \beta^0(Q \cdot (t - i)) s_{\ell}(t) dt \\ &= d_c + \sum_{\ell=1}^L \gamma_{\ell,c} \sum_{i=1}^Q x[i] \int_0^E \beta^0(Q \cdot (t - i)) s_{\ell}(t) dt \\ &= d_c + \sum_{\ell=1}^L \gamma_{\ell,c} \sum_{i=1}^Q x[i] S_{\ell}[i], \end{aligned} \quad (3.5)$$

with the average light intensity  $S_{\ell}[i]$  in the  $i^{\text{th}}$  sub-frame interval defined as:

$$\begin{aligned} S_{\ell}[i] &= \int_0^E \beta^0(Q \cdot (t - i)) s_{\ell}(t) dt \\ &= \int_{(i-1) \cdot E/Q}^{i \cdot E/Q} s_{\ell}(t) dt. \end{aligned} \quad (3.6)$$

With these notations, we can rewrite Equation (3.5) in matrix form:

$$\mathbf{y} = \mathbf{S}_Q \mathbf{\Gamma}_Q \mathbf{x} + \mathbf{d}, \quad (3.7)$$

where  $\mathbf{x} = (x[1] \ \dots \ x[Q])^{\top}$  is the vector of signal samples,  $\mathbf{d} = (d_1 \ \dots \ d_C)^{\top}$  is a bias vector, and  $\mathbf{S}_Q$  contains the time coefficients of the  $L$  lights:

$$\mathbf{S}_Q = (\mathbf{S}_Q^1 \ \dots \ \mathbf{S}_Q^{\ell} \ \dots \ \mathbf{S}_Q^L)_{C \times CQL}, \quad (3.8)$$

with:

$$\mathbf{S}_Q^{\ell} = \begin{pmatrix} (S_{\ell}[1], \dots, S_{\ell}[Q]) & \mathbb{0}_{1 \times Q} & \dots & \mathbb{0}_{1 \times Q} \\ \mathbb{0}_{1 \times Q} & \ddots & \dots & \vdots \\ \vdots & \ddots & \ddots & \mathbb{0}_{1 \times Q} \\ \mathbb{0}_{1 \times Q} & \dots & \mathbb{0}_{1 \times Q} & (S_{\ell}[1], \dots, S_{\ell}[Q]) \end{pmatrix}_{C \times CQ}. \quad (3.9)$$

The matrix  $\Gamma$  is built as:

$$\Gamma_Q = \left[ \left( \Gamma_Q^1 \quad \dots \quad \Gamma_Q^\ell \quad \dots \quad \Gamma_Q^L \right)^\top \right]_{CQL \times Q}, \quad (3.10)$$

with:

$$\Gamma_Q^\ell = \left[ \left( \gamma_{1,\ell} \mathbf{I}_Q \quad \dots \quad \gamma_{c,\ell} \mathbf{I}_Q \quad \dots \quad \gamma_{C,\ell} \mathbf{I}_Q \right)^\top \right]_{CQ \times Q}, \quad (3.11)$$

where  $\mathbf{I}_Q$  is the identity matrix of size  $Q \times Q$  and  $\mathbf{0}_{m \times n}$  a matrix with  $m$  rows and  $n$  columns of zeros (for clarity, we have indicated the dimensions of certain matrices as subscripts in a similar fashion).

## 3.4 Methods

### 3.4.1 Temporal super-resolution

The super-resolution problem is equivalent to retrieving the signal  $\mathbf{x}$  from a single color pixel  $\mathbf{y}$  by solving Equation (3.7). When the number of channels  $C$  is at least equal to the super-resolution factor  $Q$ , we propose to obtain approximate solutions in the least-squares sense by solving the minimization problem (under the assumption that the data is corrupted by additive white noise)

$$\mathbf{x}^* = \min_{\mathbf{x}} \|\mathbf{y} - \mathbf{d} - \mathbf{S}_Q \Gamma_Q \mathbf{x}\|_2^2. \quad (3.12)$$

When  $Q \leq C$  and  $Q \leq L$ , this minimization problem can be solved efficiently with a number of numerical methods (e.g. see Chapter 5.3 in [123], p. 236).

### 3.4.2 Determination of the system spectral mixing coefficients and electronics offsets

In order to retrieve  $\mathbf{x}^*$  in Equation (3.12), given the measured color pixel  $\mathbf{y}$  and the user-controlled illumination pattern  $\mathbf{S}_Q$ , the coefficients in matrix  $\Gamma_Q$  and in the bias vector  $\mathbf{d}$  must be known beforehand. We propose to determine these coefficients via a calibration procedure in which we image a static scene with a series of fixed illumination patterns that combine contributions from one or several LEDs. The static scene is illuminated with  $P$  static intensity combinations of the LEDs. These patterns are fully specified by the operator, who can choose which lights to turn on or off and who can manually select an area, comprising  $M$  pixels, on which to calibrate the system. We first consider a single pixel with a given illumination pattern and set  $Q = 1$  in Equation (3.7) to obtain:

$$\left[ \mathbf{y} \right]_{C \times 1} = \left[ \mathbf{S}_1 \right]_{C \times CL} \left[ \Gamma_1 \right]_{CL \times 1} \left[ \mathbf{x} \right]_{1 \times 1} + \left[ \mathbf{d} \right]_{C \times 1}, \quad (3.13)$$

which we rearrange as:

$$\mathbf{y} = \begin{pmatrix} \mathbf{x}\mathbf{S}_1 & \mathbf{I}_C \end{pmatrix} \begin{pmatrix} \mathbf{\Gamma}_1 \\ \mathbf{d} \end{pmatrix}, \quad (3.14)$$

where  $\mathbf{I}_C$  is the identity matrix of size  $C \times C$ . Then we combine similar equations for  $M$  pixels and  $P$  illumination patterns to form the full calibration matrix:

$$\underbrace{\begin{pmatrix} \mathbf{y}^{1,1} \\ \mathbf{y}^{1,2} \\ \vdots \\ \mathbf{y}^{1,P} \\ \mathbf{y}^{2,1} \\ \vdots \\ \mathbf{y}^{M,P} \end{pmatrix}}_{\mathbf{y}_{\text{cal}}} = \underbrace{\begin{pmatrix} x^1 \mathbf{S}_1^1 & \mathbf{I}_C \\ x^1 \mathbf{S}_1^2 & \mathbf{I}_C \\ \vdots & \vdots \\ x^1 \mathbf{S}_1^P & \mathbf{I}_C \\ x^2 \mathbf{S}_1^1 & \mathbf{I}_C \\ \vdots & \vdots \\ x^M \mathbf{S}_1^P & \mathbf{I}_C \end{pmatrix}}_{\mathbf{A}_{\text{cal}}} \begin{pmatrix} \mathbf{\Gamma}_1 \\ \mathbf{d} \end{pmatrix}, \quad (3.15)$$

where the  $x^m$  are the intensity of the  $m^{\text{th}}$  pixel of all  $M$  static calibration pixels,  $\mathbf{S}_1^p$  is the  $p^{\text{th}}$  calibration illumination pattern and  $\mathbf{y}^{m,p}$  is the measurement vector on pixel  $m$  for illumination pattern  $p$ . With this setup, all involved quantities in  $\mathbf{y}_{\text{cal}}$  and  $\mathbf{A}_{\text{cal}}$  are known, either measured or user-imposed. Note that the expression in Equation (3.14) involves  $\mathbf{\Gamma}_1$ , rather than  $\mathbf{\Gamma}_Q$ , yet even if the dimensions and structure of  $\mathbf{\Gamma}_Q$  depend on  $Q$ , its free parameters, the  $\gamma_{c,\ell}$ , are independent of  $Q$ , which allows their inference from  $\mathbf{\Gamma}_1$ .

Given these definitions and measurements, we solve for  $\mathbf{\Gamma}_1$  and  $\mathbf{d}$  in Equation (3.14) to minimize the  $\ell_1$ -norm cost:

$$e(\mathbf{\Gamma}_1, \mathbf{d}) = \left\| \mathbf{y}_{\text{cal}} - \mathbf{A}_{\text{cal}} \begin{pmatrix} \mathbf{\Gamma}_1 \\ \mathbf{d} \end{pmatrix} \right\|_1. \quad (3.16)$$

We find the solution to this cost minimization problem by using an Iteratively Reweighted Least-Squares (IRLS) method [124]. IRLS proceeds by solving, at each iteration, a weighted least-square problem:

$$\mathbf{u}^{(t+1)} = \underset{\mathbf{u}}{\operatorname{argmin}} \left\| \mathbf{W}^{(t)} \mathbf{y}_{\text{cal}} - \mathbf{W}^{(t)} \mathbf{A}_{\text{cal}} \mathbf{u}^{(t)} \right\|_2^2, \quad (3.17)$$

where  $\mathbf{W}^{(t)} = \operatorname{diag}(w_1^{(t)}, \dots, w_{MP}^{(t)})$  is a diagonal weighting matrix, whose entries  $w_k^{(t+1)}$  are updated at each iteration  $t + 1$  [125, 126]:

$$w_k^{(t+1)} = \left( \left( \mathbf{y}_{\text{cal},k} - \mathbf{A}_{\text{cal}} \mathbf{u}_k^{(t)} \right)^2 + \epsilon^{(t)} \right)^{-1/2}. \quad (3.18)$$

The weights are initialized with  $w_k^{(0)} = 1$  and  $\epsilon^{(0)} = 1$ . We follow an acceleration method similar

to that proposed by Chartrand and Yin [125], where the variable damping factor  $\epsilon^{(t)}$  is divided by 10 each time the relative change of the  $\ell_1$ -norm of the residual is smaller than  $\sqrt{\epsilon^{(t)}}/100$ , until the residual converges or  $\epsilon^{(t)}$  reaches a set minimum value ( $10^{-6}$ ). Once convergence is attained, we retrieve the values of  $\Gamma_1$  and  $\mathbf{d}$  from  $\mathbf{u}^{(t_{\text{final}})}$ . In practice, solutions we obtained with this approach were identical to those obtained by use of an exact linear programming method (CPLEX [127]). We favored our implementation for its simplicity and the possibility to make it available [128].

Although a similar approach could be used for minimizing Eq. (3.12) in order to retrieve the data, we found that for our applications, the least-squares approach, which is direct rather than iterative, is sufficient. The  $\ell_1$  norm is more robust to mismatches between the affine response model and the actual measurements. Mismatches may be due to, for example, low photon count (in dark regions), saturated pixels, or a nonlinear detector response curve. Since good calibration has a strong influence on the reconstruction quality and can be carried out offline, we favored the  $\ell_1$ -norm in Eq. (3.16) over least-squares, despite it being slower to minimize. We note that other robust norms, for which efficient algorithms exist, could be used.

### 3.4.3 Base-hue recovery and hue-dependent model-selection for non-gray samples

Although our method trades spectral information to gain temporal resolution, we can leverage our use of a color camera to collect the hue of the imaged sample during the calibration procedure of Section 3.4.2 (using white illumination), and assign the measured and normalized RGB triplet to build a color pixel  $\mathbf{x}^*[i](R \ G \ B)^\top$  from the monochromatic, temporally super-resolved reconstruction  $\mathbf{x}^*$  obtained with our method described in Section 3.4.1.

Furthermore, if the scene to be imaged is made of moving objects of any one hue among  $N$  possible hues, we can recover super-resolved images as follows. We first calibrate the system according to Sec. 3.4.2 for each one of the possible hues (indexed by  $n = 0, \dots, N - 1$ ), hence obtaining  $N$  parameter sets  $(\Gamma_Q^{(n)}, \mathbf{d}^{(n)})$  and base hue triplets  $(R^{(n)}, G^{(n)}, B^{(n)})$ . After acquiring images of a moving object (whose type or hue index  $n$  is unknown), we apply our temporal super-resolution method using each model  $(\Gamma_Q^{(n)}, \mathbf{d}^{(n)})$  in turn (e.g. on a manually selected region of interest (ROI)). We then evaluate the quality of the reconstructions  $\mathbf{x}^{*,(n)} = [x^{(n)}[1] \ \dots \ x^{(n)}[Q]]^\top$ ,  $n = 0, \dots, N - 1$  (obtained with the corresponding models  $(\Gamma_Q^{(n)}, \mathbf{d}^{(n)})$ ) by computing

$$R^{(n)} = \sum_{i=1}^{Q-1} |x^{(n)}[i] - x^{(n)}[i+1]| \quad (3.19)$$

as a measure of smoothness. The rationale behind this criterion is that only correct model

parameters will reduce flicker in regions and time-intervals where the scene is static (which we assume are present in the scene), hence decreasing  $R^{(n)}$ .

### 3.5 Experiments

#### 3.5.1 Hardware and parameters setup

We implemented the illumination with commonly available and cost effective hardware. We assembled a light source using a 6-LED chip (SLS Lighting RGBWA+UV, Aliexpress, China). The LEDs have hues red ( $\lambda \approx 620\text{nm}$ ), green ( $\lambda \approx 525\text{nm}$ ), blue ( $\lambda \approx 465\text{nm}$ ), amber ( $\lambda \approx 595\text{nm}$ ), white (broad spectrum via fluorescence), and ultra-violet ( $\lambda \approx 395\text{nm}$ ). We drove the LED via a micro-controller (Arduino Uno, Arduino, Italy), which we programmed to generate the illumination time-pattern shown on Figure 3.2(b), individually controlling each color. For the LED-camera synchronization, the micro-controller monitored the *flash* trigger output of the camera. Whenever the trigger signal transitions from low to high state, the micro-controller starts the time-sequence of the LEDs for the frame about to be recorded. The LEDs were directly powered by the controller’s outputs, without additional power amplification of the signal.

We used a CMOS color camera (Thorlabs DCC3240C, Thorlabs, Germany) with  $1280 \times 1024$  pixels, each with a standard RGGB-Bayer filter pattern ( $C = 3$ ). We used this camera both for imaging macroscopic objects, in which case we used a 12mm focal length camera objective (Navitar NMV-12M1, HR F1.4/12mm), and for microscopic samples, in which case we attached the camera to the camera port of a custom-built wide-field transmission microscope consisting of a  $20\times$  Olympus water dipping lens (Olympus Plan Fluorite UMPLFLN 20xW) combined with a 180mm tube lens (Olympus U-TLU-1-2).

We either used the LED source as-is, when illuminating macroscopic scenes, or placed it into the illumination port of the microscope, which we adjusted for Köhler illumination (transmission).

In all experiments presented here, we adjusted the exposure of our camera to  $E = 60$  milliseconds, the target over-sampling factor to  $Q = 3$ , and three LEDs per experiment, hence  $L = 3$ .

For the validation experiment in Section 3.5.2 and the beating heart data acquisition of Section 3.6.2, we used the red, green, and blue LEDs. For the robustness characterization experiment in Section 3.5.3, we used all available LEDs alternatively, by set of three. In all of these experiments, the illumination code sequences,  $S_\ell[i], i \in \{0, 1, 2\}$  corresponding to

Equation (3.6) were:

$$\begin{aligned} S_1[i] &= [1, 0, 0] \\ S_2[i] &= [0, 1, 0] \\ S_3[i] &= [0, 0, 1], \end{aligned} \tag{3.20}$$

with  $s_1(t)$  the time-function of the first,  $s_2(t)$  the second, and  $s_3(t)$  the third LED, respectively.

In Section 3.5.4, we investigate various illumination sequences that are specified in Table 3.2.

For all experiments, to calibrate  $\mathbf{d}$  and  $\Gamma_1$ , we acquired  $P = 30$  images ( $\approx 3$  calibration images per channel and per LED) of a static binary patterned sample, each with one of  $P$  different combinations of LEDs that were turned on or off (see Section 3.4.2).

### 3.5.2 Resolution improvement characterization

To quantitate the resolution improvement achievable by our method, we moved a test target (USAF resolution pattern) printed on a white cardboard paper and imaged it either: (i) with steady white light illumination; (ii) with strobed white light (one 20 ms pulse per frame); and (iii) with our proposed HESM method, followed by reconstruction.

In order to replicate the same motion in each case and thereby to allow for direct comparison, we used a robotic arm (Baxter, RethinkRobotics, Boston, MA, USA) to carry out the motion.

Under constant white light illumination (Figure 3.3 a), the resolution bars of the test target are blurred since the shutter remains open while the test target moves. With a single white light pulse per frame (Figure 3.3 b) the bars are sharp but only one image per camera frame is available. Using our method (Figure 3.3 c) we observe both sharp bars (comparable to what can be obtained with the strobed white light) and an increase in the frame-rate by a factor of three. We determined the finest resolvable resolution bar triplet in both the images obtained under white light illumination (0.25 line pairs/mm) and with our proposed HESM method (0.707 line pairs/mm). This corresponds to a 2.8-fold improvement in lateral resolution, which directly results from the improvement in temporal resolution of the same factor, given that the motion of the resolution target was uniform.

### 3.5.3 Characterization of robustness with choice of illumination hues

Our method allows, in principle, for an arbitrary choice of LED wavelength spectra for the different LEDs. In practice, however, selecting appropriate wavelengths for the LEDs given the type of imaged sample is essential to ensure the stability of the reconstruction. To illustrate

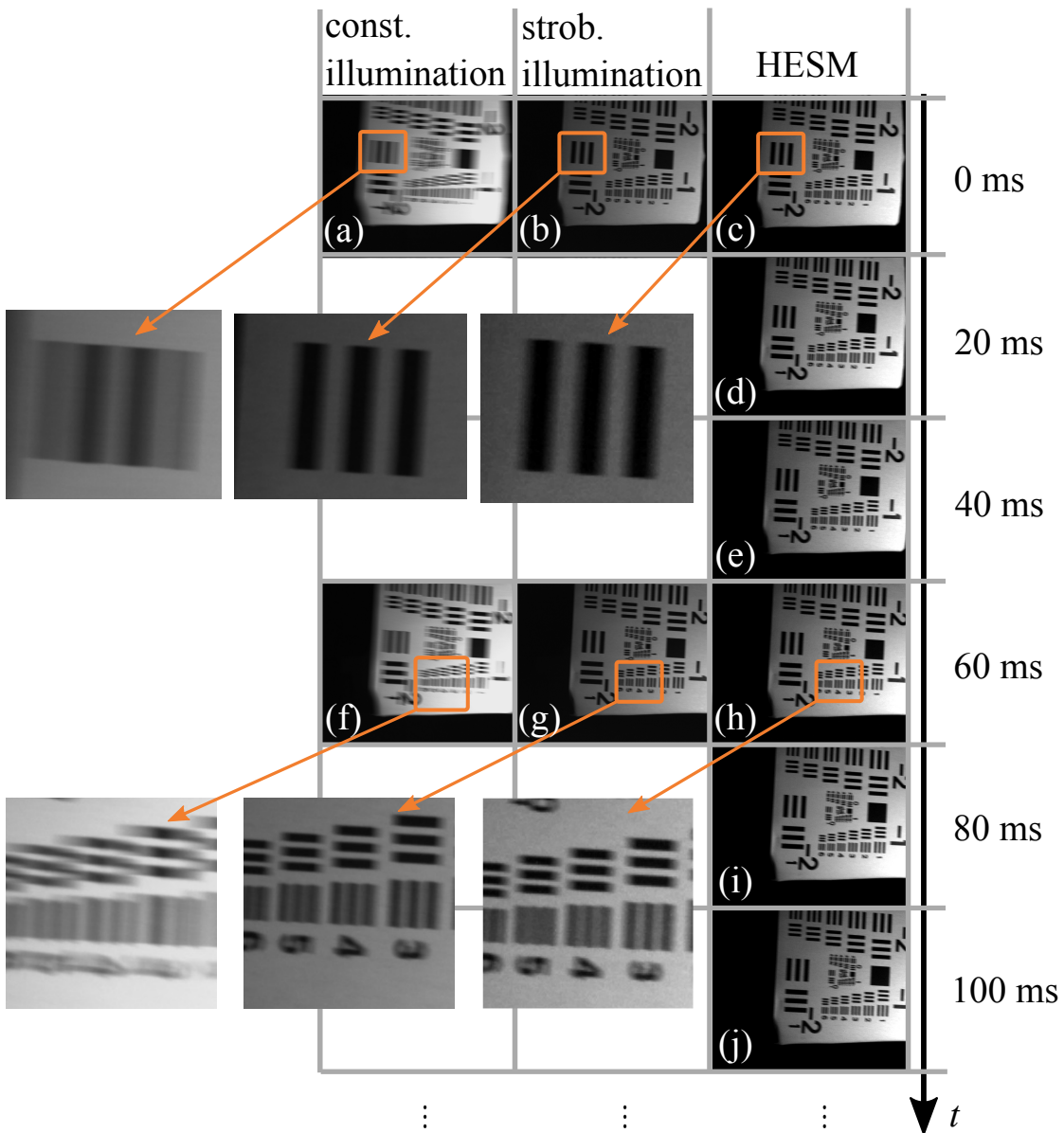






Figure 3.3 – Imaging a moving sample with (a, f) a constant white light, (b, g) a 20ms white pulse and (c, d, e, h, i, j) our proposed method (for the full movie, see [129]). The zoom on the element 1 of the group -2 of the USAF-grid (close-up in a, b, c) shows that all three methods can resolve it. It is the limit for the constant illumination. This element is 0.625  $\mu\text{m}$  wide. The detailed views on the whole group -1 (f, g, h) show that the stroboscopic illumination and our method (g, h) are able to resolve up to element 4. This corresponds to a resolution improvement factor of 2.8. Moreover, with our method operating at the same frame-rate, we have six reconstructed frames (c, d, e, h, i, j) while with the two other methods we have two acquired frames (a, b, f, g), thus we improved the frame-rate by a factor of 3.



Table 3.1 – Condition number  $\kappa$  depending on the LEDs used (see [129]).

LEDs	R-G-B	A-G-UV	B-UV-W	R-UV-B
				
$\kappa$	1.9	2.6	49.1	91.5
<b>Reconstruction</b>	good	good	noisy, flickering	noisy, flickering

this point, we explored different combinations of colors, chosen among the 6 individually addressable LEDs in our illumination head: red (R), green (G), blue (B), amber (A), white (W), and ultra-violet (UV). Specifically, we repeated the experiment of the moving target using our proposed imaging method with the following color combinations: R-G-B, A-G-UV, B-UV-W, or R-UV-B (each turned on in sequence). In order to characterize the robustness of the imaging system in each case, we calibrated the system then we calculated the conditioning number  $\kappa(\mathbf{A})$  (see Chapter 4.4 in [130], p.82) of the obtained system matrix  $\mathbf{A} = \mathbf{S}_Q \mathbf{\Gamma}_Q$ :

$$\kappa(\mathbf{A}) = \frac{\sigma_{\max}(\mathbf{A})}{\sigma_{\min}(\mathbf{A})}, \quad (3.21)$$

where  $\sigma_{\max}(\mathbf{A})$  and  $\sigma_{\min}(\mathbf{A})$  are the highest and lowest eigen-values of the matrix  $\mathbf{A}$ .

Table 3.1 gives the condition number  $\kappa$  for the 4 combinations of LEDs that we tested. See [129] for the corresponding videos. We observed that whenever the system matrix was poorly conditioned, whose likely cause we attribute to overlapping spectra of two (or three) lights in a given combination (e.g. blue and UV LEDs in the B-UW-W combination), the reconstruction was noisy and flickering. We think that there is crosstalk in the lights signal contribution, which translates into a poorly conditioned system matrix. We observed sharp reconstructions with little noise for the color combinations R-G-B and A-G-UV. The reconstructions with the two other color combinations B-UV-W and R-UV-B flickered and showed amplified noise.

### 3.5.4 The conditioning number of the system matrix depends on the illumination functions

We next investigated the influence of the illumination functions on the quality of the reconstructions. To that end, we performed an experiment similar to that in Section 3.5.3 but keeping a single set of LEDs (R-G-B) to image the same repeating motion, while varying the illumination functions. We then compared the condition number of the system matrix corresponding to each illumination pattern with the quality of the reconstruction. Table 3.2 shows the illumination intensities of the LEDs in the sub-frame time intervals for the four different cases with the corresponding condition number of the system matrix. We observed good reconstructions when the system was well-conditioned. A comparative video is provided

[129].

Table 3.2 – Condition number  $\kappa$  with various time functions.  $R_1, R_2, R_3$  are the values of the red LED respectively at the first, second and third time-steps of the whole exposure time (see [129]).

$\begin{pmatrix} R_1 & R_2 & R_3 \\ G_1 & G_2 & G_3 \\ B_1 & B_2 & B_3 \end{pmatrix}$	$\begin{pmatrix} 1 & 0.5 & 0 \\ 0.15 & 0 & 1 \\ 0 & 1 & 0 \end{pmatrix}$	$\begin{pmatrix} 1 & 0.5 & 0 \\ 0.15 & 0 & 1 \\ 0 & 1 & 0.15 \end{pmatrix}$	$\begin{pmatrix} 1 & 0.5 & 0 \\ 0.15 & 0.5 & 1 \\ 0.5 & 1 & 0.15 \end{pmatrix}$	$\begin{pmatrix} 1 & 0.5 & 1 \\ 0 & 0.5 & 1 \\ 0.5 & 1 & 0.85 \end{pmatrix}$
$\kappa$	1.9	2.6	5.9	9.4
<b>Reconstruction</b>	good	good	good	noise, flicker

## 3.6 Applications

### 3.6.1 Model selection applied to two samples

To demonstrate our method’s ability to recover both the hue of an object and a temporally super-resolved sequence, we imaged two paper cards, one whose hue was white and the other off-white. In both cases, our method could retrieve both a temporally-super-resolved image sequences as well as assign RGB values for the base-color, directly from the raw images (Figure 3.4 b,c).

### 3.6.2 Fast imaging of the beating heart

To illustrate the applicability of our HESM method for biological microscopy, we imaged the beating heart of a live 4 days post fertilization (dpf) old zebrafish larva mounted in agarose gel, with a wide-field microscope under transmitted illumination.

Zebrafish (wild-type AB zebrafish strain (Zebrafish International Resource Center) were raised under standard laboratory conditions (14/10 hour light/dark cycle, fish water of the system (ZEBTEC Techniplast Aquatic Solution) at 26.5°C temperature, 500  $\mu$ s conductivity, and pH 7.3) in a facility approved by the Veterinary Service of the State of Valais (Switzerland). Fertilized eggs were collected and the embryos raised at 29°C in standard E3 medium in an incubator (Termaks B8054), supplemented by 0.003% 1-phenyl 2-thiourea (PTU) from 24 hours post fertilization (hpf) to prevent pigmentation. For imaging, we embedded 4 dpf larvae, anesthetized with 0.1% tricaine (ethyl 3-aminobenzoate methanesulfonate salt, Sigma), in low melting agarose.

Following raw image acquisition (see hardware and parameter setup, above), we selected an ROI over which we applied our method, keeping the rest of the images in color. Figure 3.5 shows a single frame of Visualization 5 ([129]), where color imaging allows clearly visualizing

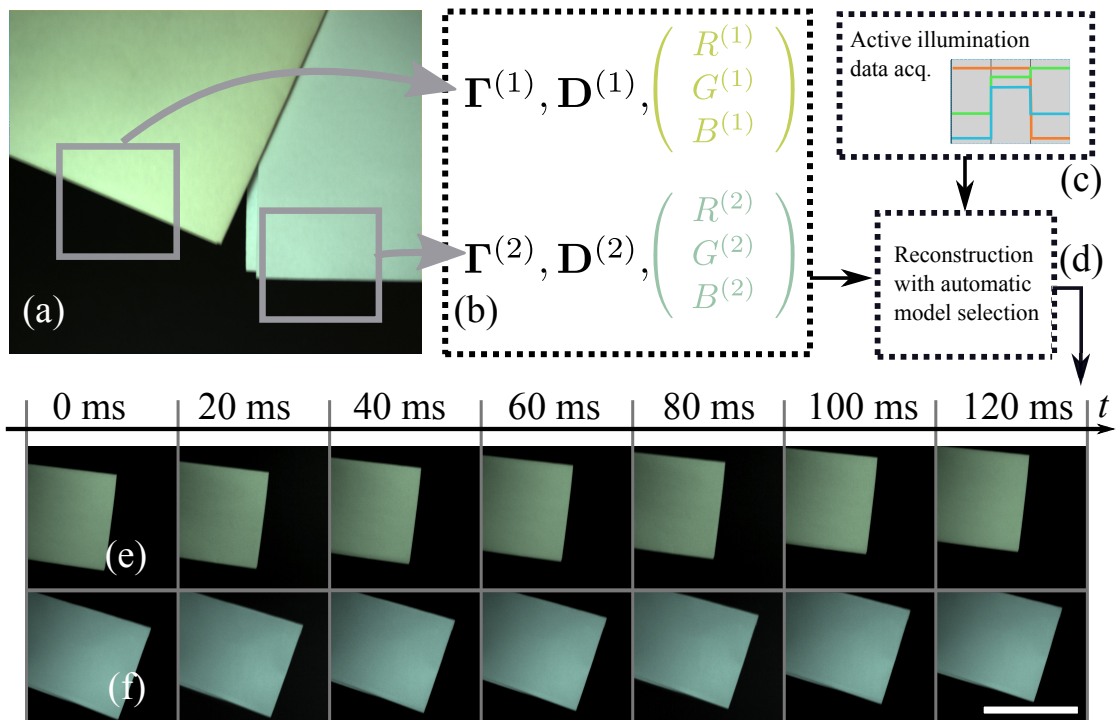


Figure 3.4 – When any of several objects with different, but known, hues enters the field of view, the system matrix adapted to the object can be automatically selected. (a) Color image of a static scene, with two kind of papers illuminated by a white light. The gray areas show the calibration ROIs. (b) Each sample has a corresponding calibrated set of parameters  $\Gamma$  and  $\mathbf{d}$  as well as the sample hue. (c) Data acquisition of a dynamic scene with the active illumination. (d) Reconstruction with model selection as explained in Section 3.4.3. (e, f) Two reconstructions with our method after model selection, using RGB LEDs and reconstructing the hue of the samples from the raw data acquired with our method (see [129]). Scale bar: 5 cm.

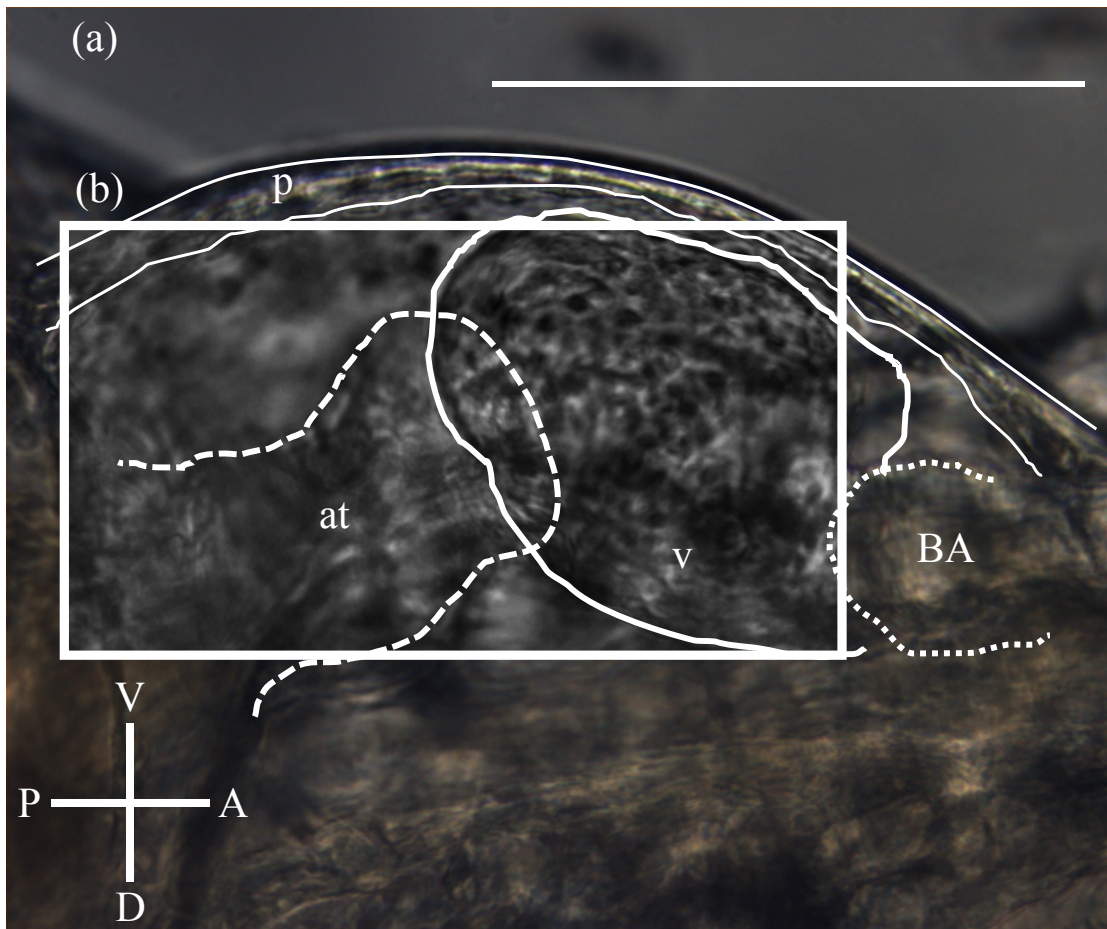


Figure 3.5 – Flexible color and fast grayscale imaging of the beating heart in a 4 days post fertilization zebrafish larva. (a) Single frame of an RGB color movie, with (b) ROI with reconstructed grayscale (no hue was measured beforehand, gray reconstruction) movie at threefold increased frame-rate. See [129] Visualization 5 for the full movie. Anatomical features visible include the ventricle (*v*), the atrium (*at*), the bulbus arteriosus (*BA*) and the pericardium (*p*). Orientation is indicated as V: ventral, D: dorsal, A: anterior, P: posterior. Scale bar:  $100\mu\text{m}$ .

cells within the heart wall of both the atrium and ventricle, which are blurred in the color images. Visualization 5 [129] first shows only color imaging of the beating heart, then it shows reconstructions from our method within an ROI and finally a comparison side by side of standard color imaging and our method, both on the same ROI. Our method therefore offers the flexibility of either using RGB or fast monochrome imaging.

### 3.7 Discussion

The hardware implementation of our method has only few hard design requirements. In particular, frame acquisition and illumination must be in synchrony, which is straightforward

to implement provided the camera has a trigger output. Given variability in hardware clocks and data transfer, independently running the illumination and acquisition systems results in rapid asynchrony and departure from the acquisition model (making it difficult to invert the system matrix). Beyond synchronization, given the frame rate of our camera (60 frames per second), neither the clock-time of our micro-controller (16 MHz) nor the rise time of our LEDs (20 ns) appeared to be limiting our method.

In order to calibrate our system as described in Section 3.4.2, it is necessary to manually select an ROI. We observed that the best results were obtained when calibration ROIs were chosen among a wide range of intensities. Our method requires a static sample (or scene) for calibration, ideally with a variety of intensities. Since acquiring calibration images is fast, many images of identical regions can be acquired fairly rapidly, which allows to limit the influence of noise, in particular in darker regions. We empirically found that acquiring  $P = 30$  images gave good calibration results and used that number for all experiments in Section 3.5.

The results in Section 3.5.2 show a time-resolution improvement of a factor  $\sqrt{8} \approx 2.8$  with a temporal sampling improvement by a factor 3. This factor depends on the number of channels available and using additional channels (e.g. through wavelength splitting and use of multiple cameras) higher resolution factors might be achievable. Less motion blur can be obtained by shortening the illumination pulses yet without improvement of the frame-rate, at the cost of a higher peak-intensity (which is sometimes undesirable in microscopy) and at the risk of producing aliasing. Longer-duration pulses are less prone to aliasing and might help preserve live samples as their peak intensity can be lower for a given camera integration time.

Although the model presented in Section 3.3 is non-specific regarding the precise illumination functions, the discrete formulation in Equation (3.7) reveals that our model becomes ill-posed should the matrix  $\mathbf{S}_Q \mathbf{\Gamma}_Q$  not be full rank, i.e. if  $\text{rank}(\mathbf{S}_Q \mathbf{\Gamma}_Q) < Q$ . This provides us with a tool for verifying that a proposed illumination function does not lead to an ill-posed system. For example, should data from a particular channel be missing,  $Q$  should be lowered such as to have  $Q \leq C$  and the matrices  $\mathbf{S}_Q$  adapted accordingly. Similarly, the matrix  $\mathbf{\Gamma}_Q$  should be well-conditioned, which depends on the sample itself, the color-filters of the camera, and the spectrum of the lighting. The spectrum absorbed and reflected by the sample and then acquired by the camera should form a matrix of rank  $Q$ , when calibrating with the procedure in Section 3.4.2. With the condition number  $\kappa$  (Section 3.5.3), we have a means of predicting the quality of reconstructions with our method given the sample, the LEDs, and the chosen camera. The results in Section 3.5.4 suggest that a condition number above 10 should be avoided, in order to guarantee a good reconstruction. For a given matrix  $\mathbf{\Gamma}_Q$  (specified by the sample, LED, and detection spectra) the matrix  $\mathbf{S}_Q$  containing the temporal patterns could be optimized for  $\mathbf{S}_Q \mathbf{\Gamma}_Q$  to have maximal rank, an NP-hard problem which we have not pursued here

### Chapter 3. Hue-Encoded Shutter Method for Temporal Super-Resolution Microscopy

---

We investigated the impact of the illumination hues in Section 3.5.3. Since the camera captures transmitted or reflected light, the same conclusions apply to changing the hue of the sample, rather than the illumination.

Simply using more lights would not necessarily produce a more stable system matrix. Instead, chasing the proper combination of lights does. A simple case for choosing the number of LEDs, channels, and super-resolution factor, is to set  $L = C = Q$  (of course one must still ensure that the choice of lights and illumination functions produces well-conditioned matrices, as discussed above).

In practice, temporal flickering may remain in the reconstructed videos, depending on how well the system's matrix  $\mathbf{S}_Q \mathbf{\Gamma}_Q$  matches dynamic conditions. Calibration and experimental conditions may differ, for example, because calibration is carried out in regions different than those imaged. Furthermore, LED rise and fall times during calibration and imaging may differ as the LEDs' electronic current drivers can be frequency-dependent

For single-hue objects, the possibility of recovering the base hue simultaneously to reconstructing temporally super-resolved image sequences (as shown in Section 3.4.3) is particularly appealing as this advantage comes without requiring an increase in the bandwidth of the system. This capability is preserved even in the case of multiple objects with different hues, via the model selection scheme we proposed in Section 3.4.3. Furthermore, for applications in microscopy, where often only a single camera can be mounted, making rapid switching to a different camera or view-port unfeasible, our method brings clear practical advantages: (i) the same camera can be used both for color and fast imaging as demonstrated in Section 3.6.2 and (ii) the motion blur can be reduced when acquiring stacks in continuous scanning mode. While the former may be particularly attractive for building versatile imaging systems, the latter may be particularly relevant for applications that require fast inspection, such as for screening or flow cytometry. We also foresee that the improved frame-rates and temporal resolution could be beneficial for object tracking applications, a point that we may investigate in the future.

Since the wavelength of the photons emitted by a fluorophore are independent of the excitation wavelength, our method would not be applicable on samples labeled with a single fluorophore. However, our method could be applied for imaging structures simultaneously co-labeled with two or more fluorophores: while the individual emission spectra shape would remain unchanged (except for scaling), as their combined emission intensity (and therefore the resulting combined spectrum) will vary with the relative excitation intensities of the illumination sources our method could, in principle, provide similar benefits to fluorescence imaging.

We provide the code, data, and instructions to reproduce results in this paper [128].

## 3.8 Conclusion

We introduced a general computational imaging method to carry out temporal super-resolution with a color camera and a set of multi-spectral active illumination sources. Each frame includes multiple copies of the signal at various times, encoded in the hue of the image. The computational procedure retrieves a high time-resolution signal, along with the base-hue, under the assumption that the imaged sample has a single color. We showed a direct method to characterize the robustness of the method, depending on the sensing and illumination spectra, as well as the base-hue of the imaged sample. We experimentally showed a temporal resolution improvement of a factor 2.8 combined with a three-fold increase of the frame-rate. We illustrated our method with an application exhibiting both color imaging and fast grayscale (on a chosen ROI) of the beating heart, showing its applicability to bio-microscopy.





## 4 Temporal super-resolution fluorescence light-sheet microscopy via a hue-encoded shutter

This chapter is directly based on our paper [131] currently under review. This paper is also the subject of a European patent application (application number EP19154253). The authors of the paper are myself, Alexander Ernst, Nadia Mercader and Michael Liebling. M. Liebling and I had the original idea of the method and implemented it. A. Ernst provided us with the zebrafish for the experiments in Section 4.4. Prof. N. Mercader is with the Institute of Anatomy of the University of Bern, she is the thesis supervisor of A. Ernst. M. Liebling and I wrote the draft of the manuscript and all authors discussed the results and contributed to the final manuscript.

To better locate this paper in the context of the whole thesis, Figure 3.1 illustrates the effect of the method when applied to the schematized heart of Figure 2.3.

### 4.1 Abstract

Studying dynamic biological processes, such as heart development and function in zebrafish embryos, often relies on multi-channel fluorescence labeling to distinguish multiple anatomical features, yet also demands high frame rates to capture rapid cell motions. Although a

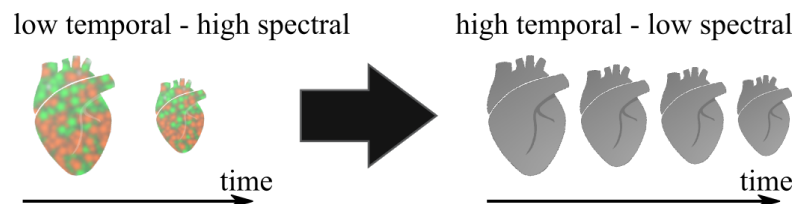


Figure 4.1 – The method presented in this chapter exchanges spectral for temporal information, in the presence of multiple co-localized fluorophores, allowing to increase the frame-rate by a factor 2 while reducing the color from 3 to 1 channel.

## Chapter 4. Temporal super-resolution fluorescence light-sheet microscopy via a hue-encoded shutter

---

recently proposed method for imaging dynamic samples in transmission or reflection allows to conveniently switch between color imaging or boosting the frame rate by use of spectrally-encoded, temporally-modulated illumination sequences and a hue-encoded shutter (hue-encode shutter method, HESM), the technique is not applicable directly in fluorescence microscopy, where the emitted light spectrum is mostly independent of the excitation wavelength. In this paper, we extend HESM by using samples labeled with multiple fluorophores, whose emission signal can either be used to distinguish multiple anatomical features when imaged in multi-channel mode or, if the fluorophores are co-localized in a dynamic tissue, to increase the frame rate via HESM. We detail the necessary steps to implement this method in a two-color light-sheet microscope to image the beating heart of a zebrafish embryo. Specifically, we propose an adapted laser modulation scheme for illumination, we identify caveats in choosing a suitable multi-color fluorophore labeling strategy, and derive an  $\ell_1$ -regularized reconstruction technique that is sufficiently robust to handle the low signal-to-noise ratio and labeling inhomogeneities in the fluorescence images at hand. Using the case of a beating heart in a zebrafish embryo, we experimentally show an increase in the frame rate by a factor two while preserving the ability to image static features labeled in distinct channels, thereby demonstrating the applicability of HESM to fluorescence. With a suitable illumination setup and fluorescent labeling, the method could generalize to other applications where flexibility between multiple channel and high-speed fluorescence imaging is desirable. For fluorophores that are not co-localized, the imaging system is similar to a conventional light sheet microscope.

### 4.2 Introduction

Fluorescence microscopy is a tool used in many biological studies. It is possible to have fluorescence light emitted by a sample from specific biological features such as nuclei, membranes, or selected molecules [110]. In addition to the need for distinctly labeling anatomical, cellular, or subcellular features, many live biological processes are highly dynamic and a high temporal resolution in imaging is required to study them [55]. Although a recently proposed method for imaging dynamic sample in transmission or reflection allows to conveniently switch between color imaging or boosting the frame rate by use of a spectrally encoded illumination and a hue-encoded shutter method (HESM), the technique is not applicable directly in fluorescence microscopy, where the emitted light spectrum is mostly independent of the excitation wavelength.

In this paper, we propose to extend the hue-encoded shutter method presented in [117] to fluorescence microscopy and to apply it to light-sheet microscopy [21]. The method in [117] increases the flexibility of microscopes by allowing to rapidly switch between color imaging and fast imaging, or to do both simultaneously, within regions of interest. Briefly, that method

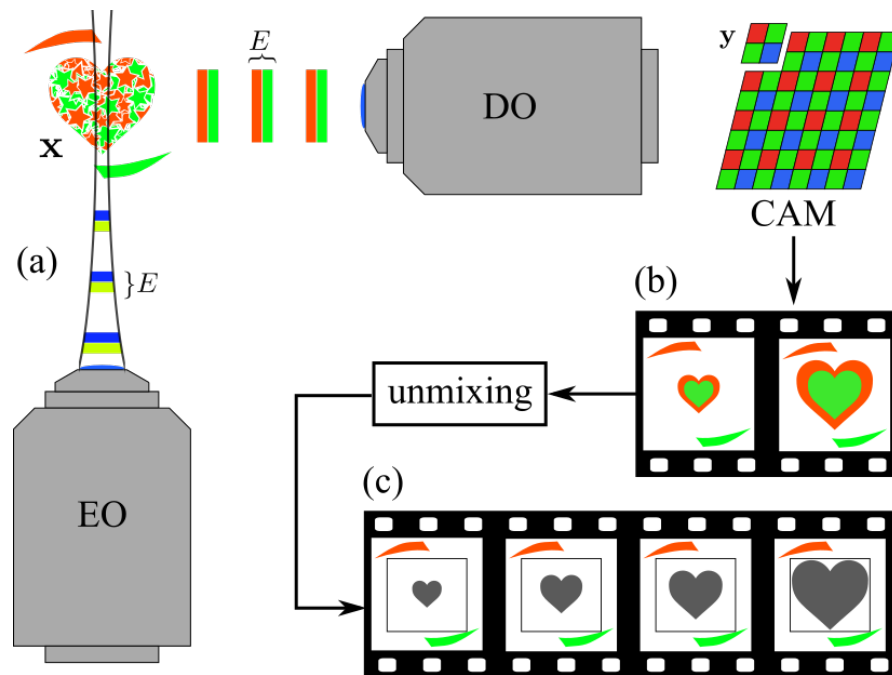


Figure 4.2 – Hue-encoded shutter for fluorescence light-sheet microscopy. (a) The excitation objective (EO) transmits consecutive pulses of different wavelengths within the exposure time  $E$  of one frame. The sample ( $x$ ) contains co-localized fluorophores (e.g. green and red fluorescent proteins) that respond to the excitation by emitting fluorescent light. The sample may also contain static regions that can be labeled with a single fluorophore type. The color sensor of the camera (CAM) captures the light emitted over the entire exposure time through the detection objective (DO). (b) Acquired (raw) multi-channel images (c) Our proposed method converts the color frames to multiple monochrome frames at a higher frame rate (here, by a factor 2) in a region of interest that contains dynamic features. The color information can be preserved in static regions outside of the region of interest.

uses a multi-color LED illumination source that is synchronized to a color camera. The scene (which is assumed to be monochromatic) is illuminated with a temporally-varying hue at a sub-frame rate frequency. The individual color frames are then processed to convert the color channels into multiple (monochrome) time frames. The monochrome requirement of [117] cannot be translated directly to fluorescence microscopy, as the spectral signature of the illumination is lost in the excitation-emission process at the heart of fluorescence. To overcome this limitation, we propose to use multiple co-localized fluorophore species with different emission spectra. The overview of the proposed method is presented in Figure 4.2.

Improving temporal or spatial resolution of microscopes has been tackled by many different approaches. We briefly review some that are of particular interest or use related concepts.

Several temporal super-resolution methods directly capitalize on strong prior knowledge of the signal itself, for example that sample motion is repetitive [73, 74] or that the signal is sparse

## Chapter 4. Temporal super-resolution fluorescence light-sheet microscopy via a hue-encoded shutter

---

in some basis [71, 72, 69]. Other approaches do not require any prior knowledge on the signal. Bub et al. [75] used a modified camera with individually addressable pixels to stagger exposure times. This method fits well for fluorescence microscopy, but requires a modified camera, which may not be widely available. Wagnert et al. [76] presented a method to instantaneously acquire full volumes of isotropic resolution thanks to two light-field imagers. While limited to small fields of view and having a lower spatial resolution than light-sheet microscopy, their method shows great potential as whole volumes can be acquired at camera frame rate, despite requiring a dedicated setup.

Our method takes advantage of temporally patterned illumination. With illumination long known to be an essential factor to a microscope's performance (as shown by Köhler [5]), the field of structured illumination microscopy has demonstrated the possibility of improving spatial resolution beyond the limits of the acquisition device [77, 78, 79, 80, 81, 132]. These methods mostly target spatial resolution improvements, often at the cost of temporal resolution, since they require multiple modulated images be merged into a higher spatial resolution image. Methods that specifically seek to improve temporal resolution by taking advantage of fast modulable illumination sources include the coded illumination method by Gorthi et al. [119], who perform motion deblurring for fluorescence microscopy using the *fluttered shutter* principle [120]. This approach is limited to linear motion deblurring. Yet other approaches, such as that of Dillavou et al. in [133] assume that the imaged sample is binary (either black or white) and use the dynamical range of a camera to drastically increase its frame rate. This strong assumption on the signal might, however, limit applicability to fluorescence microscopy.

Our method allows to do either color imaging or fast imaging in fluorescence microscopy without the limitations of the aforementioned methods as it does not require multiple or other custom modified cameras, neither do we require the signal to be sparse, repetitive, binary, or following any particular (linear) motion.

The main contributions of the present paper are (i) the adaptation of the method in [117] to fluorescence microscopy; (ii) an improved temporal super-resolution reconstruction algorithm to compensate for slight model mismatches; (iii) demonstration of the applicability to light-sheet microscopy for biological applications.

The paper is organized as follows. In Section 4.3, we present the signal and imaging models and detail the assumptions on the image acquisition and the signal and derive the algorithm to perform temporal super-resolution. In Section 4.4, we demonstrate our method in practice by performing frame-rate doubling in light-sheet microscopy of the beating heart of a double-labeled, 2 days post-fertilization old zebrafish embryo. We finally discuss our experiments and conclude in Section 4.5.

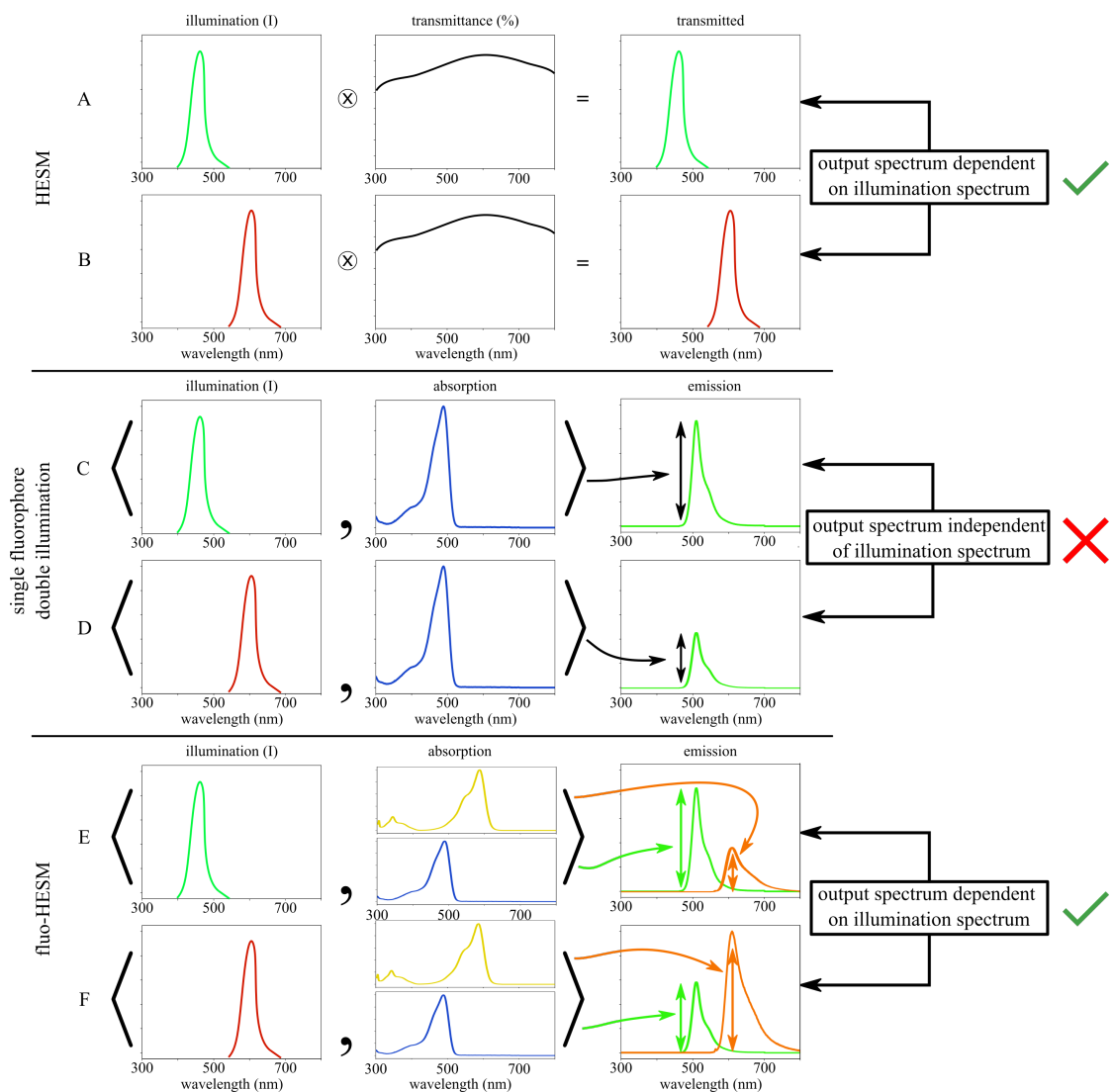


Figure 4.3 – Fluo-HESM requires co-localized multi-color fluorescent labeling. (Top row) HESM [117] assumes a bright field microscopy setup, where the illumination light is transmitted through (or reflected by) a sample then captured by an RGB camera. The transmitted (or reflected) spectrum directly depends on the combination of the illumination spectrum and the sample’s spectral transmittance. HESM relies on using a temporally-variable spectrum in the illumination, which can be decoded following capture with an RGB camera. (Middle row) If using a single fluorophore and two different illumination sources (C and D), the emission from the sample only changes in overall intensity, but the shape of the emission spectrum remains unchanged. Hence, temporal modulation of the illumination spectrum would not univocally modulate the spectral shape of the emission and HESM could therefore not be used as-is to improve the frame-rate. (Bottom row) In this paper, we propose to use two light sources E and F and a sample labeled with two co-localized fluorophore species such that the combined emitted light spectrum is directly dependent on temporal modulation patterns of the illumination spectrum, making the use of HESM to improve the frame rate possible.

### 4.3 Methods

Before we delve into the details of our proposed method, we briefly recall assumptions of the HESM method developed in [117] and the limitations that prevent it from being directly applicable to fluorescence microscopy. In [117], the light captured by the camera (Fig. 4.3 A, B) was assumed to be either reflected by the imaged scene or transmitted through a sample. This implied that the light spectrum measured by the camera was that of the illumination light source modulated by the spectral sample response. To follow a monochromatic object with higher temporal resolution, temporal variations could be encoded spectrally in the illumination pattern by using light sources of different hues. In the case of fluorescence microscopy with a single type of fluorophore (Fig. 4.3 C, D), while the emitted light (which results from the fluorophores' relaxation following their excitation by the incoming light) has an overall intensity that depends on the excitation light via the molecules' spectral absorption properties, its spectrum only depends on the emission properties of the fluorophore but not on the spectrum of the excitation. Hence, the spectrum captured by the camera does no longer depend on the light source used, which precludes the possibility of using HESM in a way similar to the brightfield case. Our proposed way to extend HESM to fluorescence involves the use of multiple co-localized fluorophores (Fig. 4.3 E, F). Although each fluorescent species' individual emission spectrum is independent of the illumination spectrum, the fluorophores' *combined* emission spectrum depends on the spectral overlap of the illumination with the absorption curve of each fluorophore. An added challenge for the fluorescence case is that fluorophores typically have broad and overlapping emission spectra, which makes it more difficult to isolate their contributions in distinct RGB channels as could be done with narrow-band illuminations in the case of transmission HESM. This overlap, therefore, requires an unmixing step.

#### 4.3.1 Imaging model

The fluorescence imaging setup we consider is made of a color camera with  $C$  channels and  $L$  lasers of different wavelengths (Fig. 4.2). We further consider a dynamic sample  $\mathbf{x}(t)$  labeled with  $F$  different, co-localized fluorophore species. We write the intensity measured in the  $c^{\text{th}}$  channel of a single pixel, during the  $k^{\text{th}}$  acquisition at time  $t_k$ , as:

$$y_{c,k} = \int_{t_k}^{t_k+E} \sum_{\ell=1}^L \sum_{f=1}^F \gamma_{c,f} b_{f,\ell} s_{\ell}(t) x(t) dt + d_c, \quad (4.1)$$

where  $E$  is the exposure time of the camera,  $s_{\ell}(t)$  the time-varying intensity function of the  $\ell^{\text{th}}$  laser,  $b_{f,\ell}$  is the absorption cross section of the  $f^{\text{th}}$  fluorophore to the  $\ell^{\text{th}}$  laser,  $\gamma_{c,f}$  is the sensitivity of the  $c^{\text{th}}$  color channel to the  $f^{\text{th}}$  fluorophore emission spectrum and  $d_c$  is

an offset from the sensor's electronics. Similarly to the model in [117], we assume that the temporal signal of interest lies in the space spanned by shifted B-splines of degree 0, i.e.:

$$x(t) = \sum_{i \in \mathbb{Z}} x[i] \beta^0((t-i)Q), \quad (4.2)$$

where  $Q$  is the super-resolution factor (i.e.  $x(t)$  takes  $Q$  different values over the time of an exposure time  $E$ ) and  $\beta^0(t)$  is the indicator function over the interval  $[-\frac{1}{2}, \frac{1}{2}]$ . We can rewrite Equation (4.1) as:

$$\begin{aligned} y_{c,k} &= d_c + \sum_{\ell=1}^L \sum_{f=1}^F \gamma_{c,f} b_{f,\ell} \int_{t_k}^{t_k+E} s_{\ell}(t) \sum_{i=0}^{Q-1} x[t_{k,i}] \beta^0\left(\left(t - \frac{E}{Q}i\right)Q\right) dt \\ &= d_c + \sum_{\ell=1}^L \sum_{f=1}^F \gamma_{c,f} b_{f,\ell} \underbrace{\sum_{i=0}^{Q-1} x[t_{k,i}] \int_{t_k + \frac{E}{Q}i}^{t_k + \frac{E}{Q}(i+1)} s_{\ell}(t) dt}_{s_{\ell}[t_{k,i}]}, \end{aligned} \quad (4.3)$$

where  $t_{k,i}$  is the index for the values of  $x[\cdot]$  and  $s_{\ell}[\cdot]$  at time  $t_k + \frac{E}{Q}i$ . We adopt a matrix notation to write Eq. (4.3) for the full system:

$$\mathbf{y}_k = \mathbf{S}\mathbf{\Gamma}\mathbf{x}_k + \mathbf{d}_0, \quad (4.4)$$

where  $\mathbf{\Gamma} \in \mathbb{R}^{LCQ \times Q}$  expresses both the response of the fluorophores to the excitation light ( $b_{f,\ell}$ ) and the sensitivity of the camera's sensor to the emitted fluorescent light ( $\gamma_{c,f}$ ),  $\mathbf{S} \in \mathbb{R}^{C \times LCQ}$  is the matrix built by computing the integral in Eq. (4.3) and by shifted zero-padded vectors of time-functions for each laser,  $\mathbf{x}_k = [x[t_{k,0}], x[t_{k,1}], \dots, x[t_{k,Q-1}]]^{\top}$  is the unknown vector of  $Q$  values of  $x(t)$  during  $E$ , and  $\mathbf{d}_0 \in \mathbb{R}^{C \times 1}$  is the offset vector [134].

As a concrete example (which is the case we will consider in our experiments) we set  $C = 3$ ,  $L = 2$ , and  $Q = 2$ . We choose to set the illumination temporal functions of the  $L = 2$  lights as  $s_1 = [1, 0]$  and  $s_2 = [0, 1]$ . That is, each light source will be switched on for half of the exposure time, consecutively. In this setting, the matrix  $\mathbf{S}$  is written as  $\mathbf{S} = \begin{pmatrix} \mathbf{S}^1 & \mathbf{S}^2 \end{pmatrix}$  and (see [117] for further details):

$$\mathbf{S}^1 = \begin{pmatrix} \boxed{s_1[0]} & \boxed{s_1[1]} & 0 & 0 & 0 & 0 \\ 0 & 0 & \boxed{s_1[0]} & \boxed{s_1[1]} & 0 & 0 \\ 0 & 0 & 0 & 0 & \boxed{s_1[0]} & \boxed{s_1[1]} \end{pmatrix} = \begin{pmatrix} \boxed{1} & \boxed{0} & 0 & 0 & 0 & 0 \\ 0 & 0 & \boxed{1} & \boxed{0} & 0 & 0 \\ 0 & 0 & 0 & 0 & \boxed{1} & \boxed{0} \end{pmatrix} \quad (4.5)$$

is the matrix expressing the first light source's temporal activation pattern. Similarly,

$$\mathbf{S}^2 = \begin{pmatrix} \boxed{s_2[0]} & \boxed{s_2[1]} & 0 & 0 & 0 & 0 \\ 0 & 0 & \boxed{s_2[0]} & \boxed{s_2[1]} & 0 & 0 \\ 0 & 0 & 0 & 0 & \boxed{s_2[0]} & \boxed{s_2[1]} \end{pmatrix} = \begin{pmatrix} \boxed{0} & \boxed{1} & 0 & 0 & 0 & 0 \\ 0 & 0 & \boxed{0} & \boxed{1} & 0 & 0 \\ 0 & 0 & 0 & 0 & \boxed{0} & \boxed{1} \end{pmatrix} \quad (4.6)$$

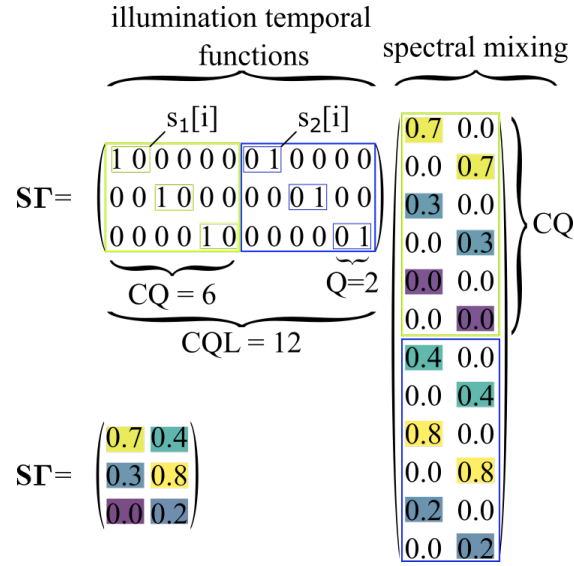


Figure 4.4 – Forward matrix  $\mathbf{S}\mathbf{\Gamma}$  combines temporal illuminations patterns of two lasers and the combined absorption and emission responses of the two fluorophores, together with the spectral response of the camera. Notice that the left part of the matrix  $\mathbf{S}$ , boxed in green, contains repetitions of the temporal function of the green laser:  $s_1[i]$  and the right part of  $\mathbf{S}$  contains the same information for the blue laser. We also framed in green, respectively blue, the part that corresponds to the green, respectively blue, laser in the  $\mathbf{\Gamma}$  matrix which expresses the efficiency of each fluorophore to the lasers combined with the sensitivity of the camera to the fluorescence emission spectra.

is the matrix expressing the second light source's temporal activation pattern. We recall that  $\mathbf{S}_1, \mathbf{S}_2 \in \mathbb{R}^{C \times CQ=3 \times 6}$  and  $\mathbf{S} \in \mathbb{R}^{C \times CQL=3 \times 12}$ . Our example further leads to  $\mathbf{\Gamma} = \left( (\mathbf{\Gamma}^1)^\top \quad (\mathbf{\Gamma}^2)^\top \right)^\top$  with  $\mathbf{\Gamma}^\ell$ ,  $\ell = 1, 2$ , the spectral mixing matrix for the  $\ell^{\text{th}}$  light source:

$$\mathbf{\Gamma}^\ell = \begin{pmatrix} (\gamma_{1,1} b_{1,\ell} + \gamma_{1,2} b_{2,\ell}) \mathbf{I}_2 \\ (\gamma_{2,1} b_{1,\ell} + \gamma_{2,2} b_{2,\ell}) \mathbf{I}_2 \\ (\gamma_{3,1} b_{1,\ell} + \gamma_{3,2} b_{2,\ell}) \mathbf{I}_2 \end{pmatrix}, \quad (4.7)$$

where  $\mathbf{I}_2$  is the identity matrix of size  $2 \times 2$ . We recall that  $\gamma_{c,f}$  is the spectral impact of the  $f^{\text{th}}$  fluorophore on the  $c^{\text{th}}$  channel, and that  $b_{f,\ell}$  is the response of the  $f^{\text{th}}$  fluorophore to the  $\ell^{\text{th}}$  light. Thus,  $(\gamma_{2,1} b_{1,1} + \gamma_{2,2} b_{2,1})$  is the compound contributions from both fluorophores reacting to the first illumination source as captured by the camera's second channel. Figure 4.4 further illustrates these quantities and displays the values corresponding to the experimental setting in Section 4.4.



**Require:**  $\rho, \lambda, \epsilon, k_{\max}, \mathbf{A}, \mathbf{y}, \mathbf{d}, \mathbf{T}$   
 $\mathbf{u}^0 = \mathbf{0}_{MQ \times 1}$ ;  
 $\mathbf{z}^0 = \mathbf{0}_{MQ \times 1}$ ;  
 $k = 0$ ;  
**while**  $\|\mathbf{x}^{k+1} - \mathbf{x}^k\|_2 < \epsilon$  **and**  $k < k_{\max}$  **do**  
     $\mathbf{x}^{k+1} = (\mathbf{A}^\top \mathbf{A} + \rho \mathbf{T}^\top \mathbf{T})^{-1} (\mathbf{A}^\top (\mathbf{y} - \mathbf{d}) + \mathbf{T}^\top (\rho \mathbf{u}^k - \mathbf{z}^k))$ ;  
     $\mathbf{u}^{k+1} = S_{\lambda/\rho}(\mathbf{T} \mathbf{x}^{k+1} + \mathbf{z}^k)$ ;  
     $\mathbf{z}^{k+1} = \mathbf{z}^k + \mathbf{T} \mathbf{x}^{k+1} - \mathbf{u}^{k+1}$ ;  
     $k = k + 1$ ;  
**end**  
with  $S_{\lambda/\rho}(s_i) = \begin{cases} s_i - \lambda/\rho & \text{if } s_i > \lambda/\rho \\ s_i + \lambda/\rho & \text{if } s_i < -\lambda/\rho \\ 0 & \text{if } |s_i| < \lambda/\rho \end{cases}$ , the *soft threshold operator* [135].

**Algorithm 1:** ADMM to solve the problem presented in Equations (4.9) and (4.10)

### 4.3.2 Temporal super-resolution from hue encoded signal

In [117] we performed temporal super-resolution by solving

$$\mathbf{x}_k^* = \underset{\mathbf{x}_k}{\operatorname{argmin}} \|\mathbf{y}_k - \mathbf{d}_0 - \mathbf{S}\mathbf{T}\mathbf{x}_k\|_2^2 \quad (4.8)$$

for every acquired frame, where  $\mathbf{d}_0$  and  $\mathbf{T}$  were obtained via calibration. We solved Eq. (4.8) for each pixel and each acquired frame independently, without any dependency between consecutive frames. While this approach performs well as long as the hue is homogeneous over the imaged scene, we observed that fluorophore labeling can be inhomogeneous, as illustrated in Figure 4.6.

To make the method in [117] more robust to model mismatches, we propose to add a regularization term over time which introduces a dependency over consecutive frames (temporal dependency). Given the model presented in Eq. (4.4), the vector  $\mathbf{d}_0$  and matrix  $\mathbf{T}$  obtained through calibration [117] and a sequence of  $M$  acquired color pixels  $\mathbf{y} = [\mathbf{y}_0^\top, \mathbf{y}_1^\top, \dots, \mathbf{y}_{M-1}^\top]^\top \in \mathbb{R}^{MC \times 1}$ , we want to reconstruct the temporal high-resolution signal  $\mathbf{x} = [\mathbf{x}_0^\top, \mathbf{x}_1^\top, \dots, \mathbf{x}_{M-1}^\top]^\top \in \mathbb{R}^{MQ \times 1}$  with a temporal super-resolution factor of  $Q$ . We propose to solve

$$\mathbf{x}^* = \underset{\mathbf{x}}{\operatorname{argmin}} \frac{1}{2} \|\mathbf{y} - \mathbf{d} - \mathbf{A}\mathbf{x}\|_2^2 + \lambda \|\mathbf{T}\mathbf{x}\|_1, \quad (4.9)$$

where  $\mathbf{T} \in \mathbb{R}^{MQ \times MQ}$  is a first-order derivative matrix,  $\lambda \in \mathbb{R}_+$  is a free parameter and  $\mathbf{d} \in \mathbb{R}^{MC \times 1}$  is  $\mathbf{d}_0$  stacked  $M$  times. The matrix  $\mathbf{A} \in \mathbb{R}^{MC \times MQ}$  is a block-diagonal matrix built by repeating  $\mathbf{S}\mathbf{T}$  along the diagonal  $M$  times. The regularization is known as *Total Variation* [136] and promotes piecewise-constant solutions, which is natural in time series of images as it preserves sharp edges. Equation (4.9) has the generalized LASSO form [137] and can be solved with the

## Chapter 4. Temporal super-resolution fluorescence light-sheet microscopy via a hue-encoded shutter

---

Alternating Direction Method of Multipliers (ADMM) [138, 135], an efficient choice among other possible methods [137, 139, 140]. The ADMM considers a problem equivalent to that in Eq. (4.9),

$$\begin{aligned} & \text{minimize} && \frac{1}{2} \|\mathbf{y} - \mathbf{d} - \mathbf{Ax}\|_2^2 + \lambda \|\mathbf{u}\|_1, \\ & \text{such that} && \mathbf{T}\mathbf{x} = \mathbf{u} \end{aligned}, \quad (4.10)$$

and builds the *augmented Lagrangian* defined as

$$\begin{aligned} \mathcal{L}(\mathbf{x}, \mathbf{u}, \mathbf{y}) = & \|\mathbf{y} - \mathbf{Ax} - \mathbf{d}\|_2^2 + \lambda \|\mathbf{u}\|_1 \\ & + \mathbf{z}^\top (\mathbf{T}\mathbf{x} - \mathbf{u}) + (\rho/2) \|\mathbf{T}\mathbf{x} - \mathbf{u}\|_2^2, \end{aligned} \quad (4.11)$$

where  $\rho > 0$  is a penalty parameter,  $\mathbf{u}$  is a *primal* variable (as well as  $\mathbf{x}$ ) and  $\mathbf{z}$  is a *dual* variable, also called *Lagrangian multiplier*. The ADMM algorithm consists of iterative steps in which the gradient of the augmented Lagrangian is set to zero for the primal variables [135]. At each iteration  $k$ , we alternate between solving a least-squares problem with fixed regularization weights and updating the regularization parameters (Lagrange multipliers). The global regularization weight  $\lambda$ , which balances the relative importance of the data and regularisation terms, is fixed during the entire process (we set its value empirically but it could be set using an L-curve method [141, 142]). The iterations stop when a maximal number of iterations  $k_{\max}$  has been reached or when the difference between consecutive solutions for  $\mathbf{x}^k$  is lower than a given value  $\epsilon \in \mathbb{R}_+$ . Algorithm 1 provides the corresponding pseudo-code in our case.

### 4.4 Experiments

We used our implementation of a light sheet microscope (based on OpenSPIM [33]), with two lasers (Stradus, Vortran Laser Technology) of wavelengths 488nm and 561nm to generate the excitation illumination light sheet. A four-dimensional stage (USB 4D-STAGE, Picard) held the sample. The detection axis consisted of a 20 $\times$ /0.5 water immersion microscopy lens (UMPLFLN 20 $\times$ W, Olympus) coupled to a 180 mm tube-lens (U-TLU-1-2, Olympus), terminated by a 1.2 mega pixels CMOS color camera equipped with an RGGB Bayer filter (DCC3240C, Thorlabs Instruments). The lasers and camera were electronically synchronized using a micro-controller (Arduino Due, Arduino, Italy). The micro-controller monitored the *flash* output of the camera and controlled the lasers using their *ON/OFF* electrical input, similarly to the electronics scheme provided in [128].

We conducted experiments on more than one fish sample, and there were differences in fluorescent proteins expression between different samples. In order to have acceptable SNR in the acquired images, we adjusted the exposure time of the camera, hence different frame-rates in the following experiments.

#### 4.4.1 Temporal super-resolution light-sheet imaging of the beating heart of a zebrafish

To illustrate the potential of our method, we tested whether it was applicable to imaging the beating heart of a zebrafish embryo. To that end, we chose zebrafish that co-express ubiquitous cytoplasmic green fluorescent protein, EGFP, and red fluorescent protein, mCherry [143] (two co-localized fluorophores,  $F = 2$ ). We embedded the embryos on a glass bottom dish in 1% low melting agarose and acquired 30 frames ( $M = 30$ ) with our RGB camera ( $C = 3$ ); setting the super-resolution factor to  $Q = 2$ , the two lasers ( $L = 2$ ) were controlled so that they were each switched on for half of the exposure time (consecutively), so that we had  $s_1[i] = [1, 0]$  and  $s_2[i] = [0, 1]$ ,  $i \in \{0, 1\}$ . Figure 4.5 shows two consecutively acquired frames (Fig. 4.5(a),(e)), all color channels of the acquisitions (Fig. 4.5(b)-(d), (g)-(h)), and the corresponding four reconstructed frames (Fig. 4.5(i)-(l)). Note that, as discussed in Fig. 4.4, the blue layer (Fig. 4.5(d),(h)) contains very little energy. Our method was therefore capable of doubling the frame rate. Here, we had  $F = 2$ , which limited the frame rate increase to  $Q = 2$ , but with additional fluorophore species and acquisition channels, higher  $Q$  could be considered. The matrix  $\mathbf{\Gamma}$  and the vector  $\mathbf{d}$  were obtained with the calibration procedure in [117], using the code available online [128]. The area used for calibration is shown in Figure 4.6(d). Figure 4.4 illustrates how the matrix  $\mathbf{A} = \mathbf{S}\mathbf{\Gamma}$  is built. We observe that the green laser has a high impact (first value, 0.7) on the red channel of the camera, which is due to the green laser mostly exciting the red fluorophores and the ensuing red fluorescent light will mostly be captured on the red channel of the camera. Similarly, the blue laser has a high impact on the green channel of the camera (value of 0.8), as it mostly excites the green fluorophores. Finally, note that none of the lasers really impact the blue channel, since there are no blue fluorophores. The values displayed on Figure 4.4 are the ones obtained after calibration and were used for the following experiments.

#### 4.4.2 Homogeneity of the fluorescent co-expression ratio

Our method requires that the imaged sample shows consistent fluorescent co-expression. We set out to make sure that the (static) calibration area and the (dynamic) heart area have indeed homogeneous and matching green and red fluorescent protein expression levels. To that end, we computed the red over green ratio (R/G) for each pixel on the images we acquired to compute the calibration, displayed on Fig. 4.6(b). We then computed the R/G histograms over various areas to compare them (Fig. 4.6(c'), (d') and (e')).

Figure 4.6 shows an acquired color image where the lasers were temporally controlled as explained in Figure 4.4. The ventricle (V), atrium (At) and pericardium (p) are outlined. In the pericardium on Fig. 4.6(a), some patches appear green, while the heart appears orange. This

## Chapter 4. Temporal super-resolution fluorescence light-sheet microscopy via a hue-encoded shutter

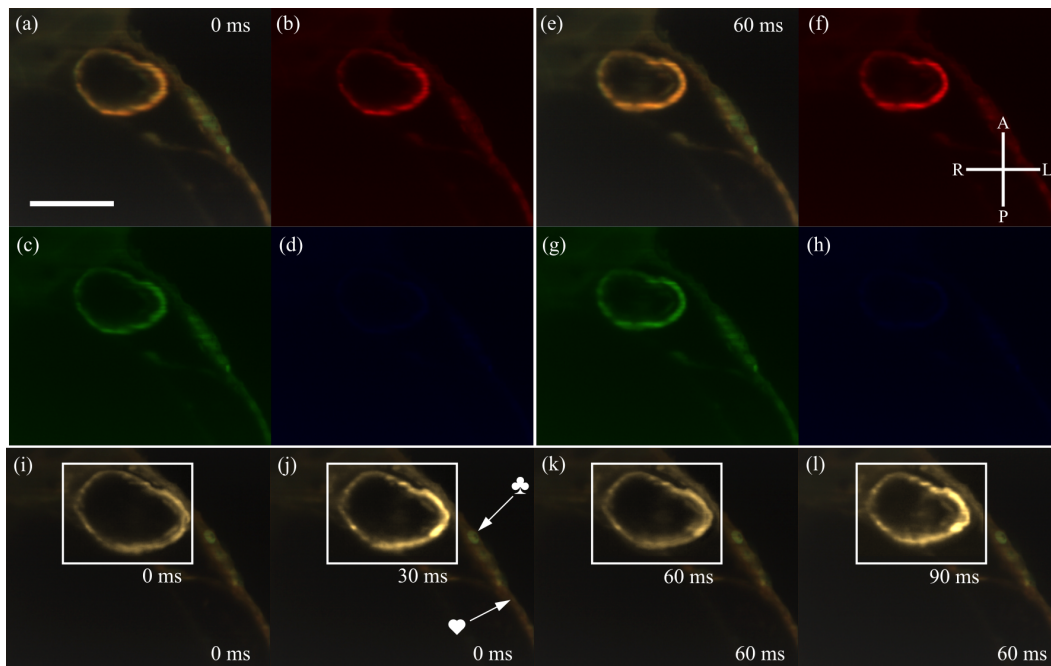


Figure 4.5 – Fluo-HESM allows simultaneous fast imaging of the beating heart and color imaging of its surroundings. (a),(e) two consecutive acquired frames. (b)-(d), respectively (f)-(h) are the red, green and blue layers of the image in (a), respectively (e). (i)-(l) reconstructed frames using Algorithm 1 with  $\lambda = 0.001$ . The super-resolution factor is 2, hence for two acquired frames, we observe 4 reconstructed frames. Note that there are 60 milliseconds between the two acquired frames (a) and (e) and 30 milliseconds between the super-resolved region in frames (i)-(l), framed in a white rectangle. Outside of this region, our method allows keeping the color information. On (j), we marked two regions with drastically different colors, green ( $\heartsuit$ ) and orange ( $\clubsuit$ ). To highlight the link between this data and the schematic of Figure 4.2, (a) and (e) on this figure correspond to Fig. 4.2 (b) and (i)-(l) to Fig. 4.2 (c). See [129] Visualizations 1 and 2 for the full movie. Fish orientation indicated: anterior (A), posterior (P), right (R) and left (L). Scale bar:  $100 \mu\text{m}$ .

is better seen on Fig. 4.6(b), comparing (c), (d) and (e) and their corresponding histograms on (c'), (d') and (e').

Inhomogeneities in the co-expression of red and green fluorescent proteins are visible over the sample (for example Fig. 4.6(e) and (e') compared to Fig. 4.6(d) and (d')). Given this expression variability (which is common from individual to individual or within the sample), it is thus important to choose a motionless calibration area (Fig. 4.6(d) and (d')) that exhibits similar R/G ratio than that of the dynamic phenomenon of interest, like the beating heart (Fig. 4.6(c) and (c')). Even with a careful choice, slight differences in the histogram remain (compare (c') and (d')). This justifies the use of an algorithm that is sufficiently robust to mismatches than a plain least-squares method without regularization. We further investigated this aspect in Section 4.4.4.

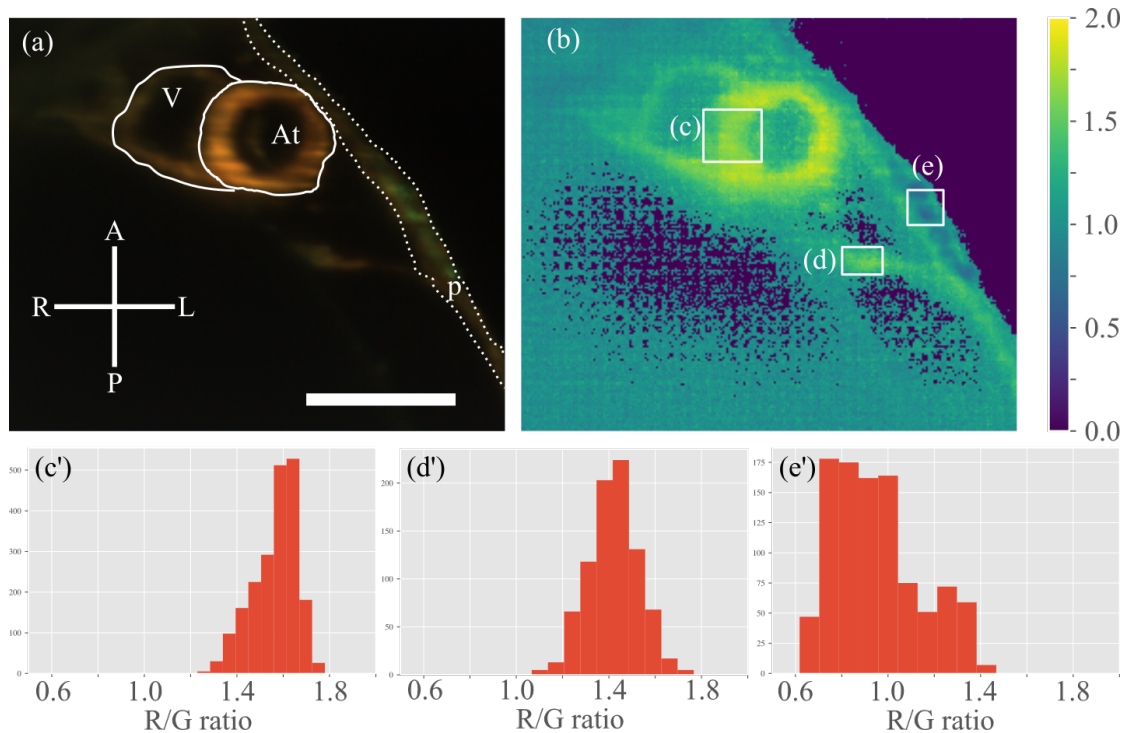


Figure 4.6 – A static region is required to calibrate our method. The region must also have a similar red over green (R/G) ratio than in the heart. (a) Hue-encoded light-sheet image of a 2 days post-fertilization zebrafish heart. The ventricle (V), the atrium (At) and the pericardium (p) are outlined. (b) The ratio R/G of each pixel on the image in (a). Notice that the ratio R/G is not homogeneous over the whole image. In order to calibrate our method, we need a static region with the same ratio R/G as in the heart; it is shown in (d). (d') shows the histogram of values within (d). Similarly, (c') and (e') show histograms of their corresponding regions (c) and (e). Notice that the calibration region (d) has a histogram similar to that of the heart (c), with a maximum centered around 1.5. The histogram in (e') is obviously different to that in (c') and (d'), so our method would require another calibration to be used in the area of (e). Fish orientation indicated: anterior (A), posterior (P), right (R) and left (L). Scale bar:  $100\mu\text{m}$ .

### **4.4.3 Combined fast and color imaging on the beating heart of a zebrafish**

We applied Algorithm 1 only in the region comprising the beating heart. In this way we could maintain the color information in static areas and do fast imaging where needed. Since we require the imaged sample (in this case, the heart) to be homogeneously labeled for temporal super-resolution, after Algorithm 1 we can virtually assign the (single) hue back to the reconstructed images. Figure 4.7 shows two frames where we have temporal super-resolution reconstructed frames only in a region of interest (Fig. 4.7(c)) and where the acquired hue is preserved in static areas (Fig. 4.7(a) and (b)).

### **4.4.4 ADMM compared to least-squares without regularization**

As observed in Section 4.4.2 and Figure 4.6, there can be inhomogeneities in the co-expression ratios of the fluorescent proteins over the sample. We investigated whether the algorithm we introduced in Section 4.3 (ADMM) is more robust to these variations than the least-squares method (LSTSQ) without regularization of [117]. To that end, we compared reconstructions obtained using either ADMM or LSTSQ with the same input data. Figure 4.7(d) shows a comparison of both reconstructions at the same location, where the heart beats. The cardiac period is visible in both plots yet the ADMM reconstruction is smoother with sharp transitions maintained, unlike the LSTSQ reconstruction. This behavior is to be expected with the Total-Variation regularization. In Figure 4.7(e), we compared ADMM and LSTSQ reconstruction at a location where the imaged sample is mostly static. There the reconstructions is expected to be nearly constant, which is indeed the case for the ADMM reconstruction, while the LSTSQ reconstructions oscillates, most likely because of a slight image model mismatch.

For the ADMM reconstruction, the processing time for 45 time-points on a single pixel (i.e. 90 reconstructed time-points) was  $\approx 1.7$  milliseconds on a MacBook Pro 2018 (2.9 GHz 6-Core Intel Core i9, 32 Gb RAM). The code is in standard Python 3. We believe that with GPU programming, separating the processing of each individual pixel, and some tweaking, the code could run in real-time.

### **4.4.5 Impact on the reconstruction of 3D volumes of the beating heart**

Light-sheet microscopy is a well-established tool for developmental studies thanks to its high spatio-temporal resolution and its low level of induced optical damage to the sample [144]. Furthermore, it has good sectioning capabilities, which we took advantage of to produce a dynamic 3D+time volume series (XYZ + time). We acquired movies of optical sections at different depths within the sample, applied our temporal super-resolution method to each individual movie, then temporally registered consecutive (in  $z$ ) movies for the heartbeat to

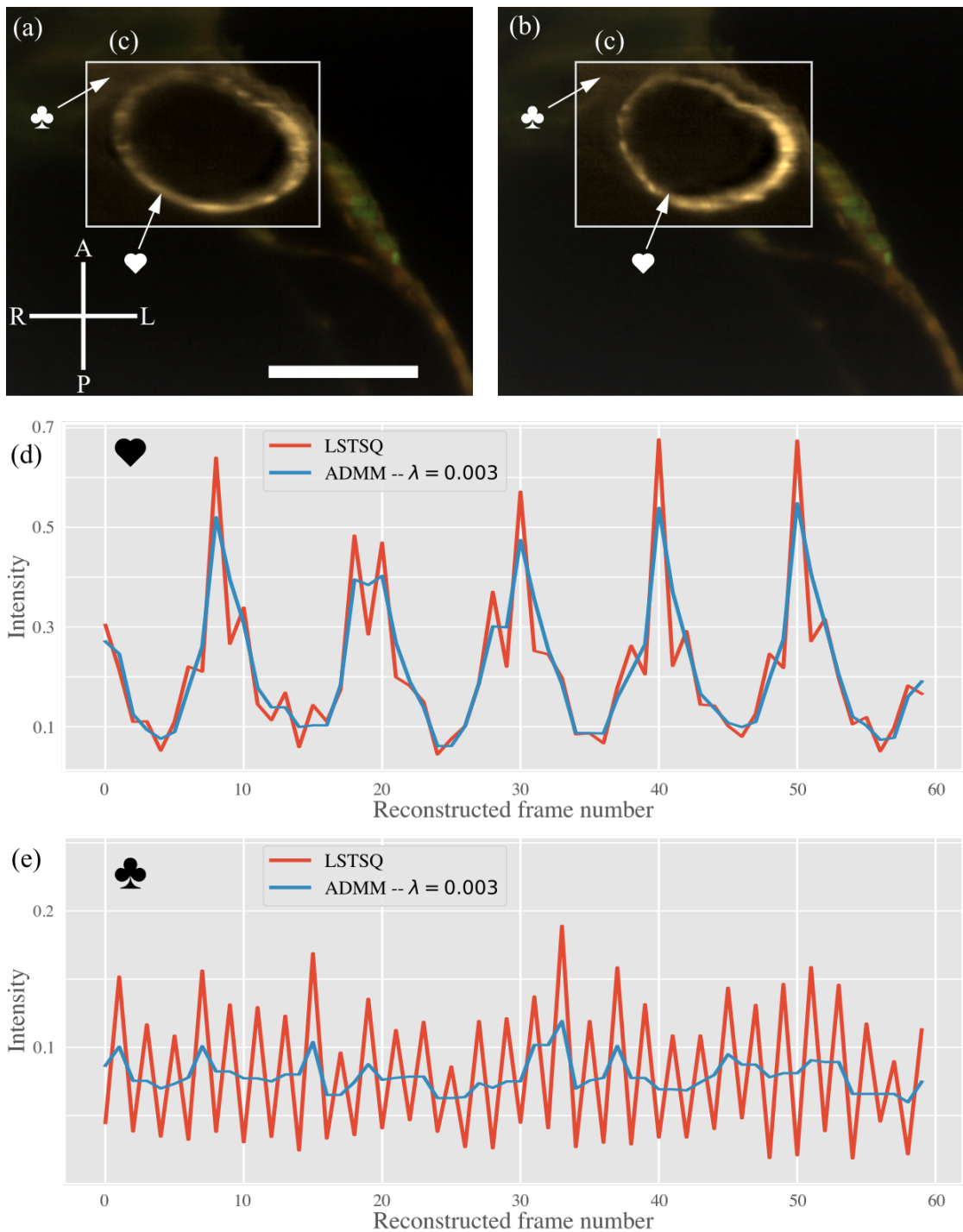


Figure 4.7 – Fluorescence microscopy is robust to fluorescence labeling inhomogeneities thanks to the temporal  $\ell_1$  regularization. (a)-(b) Composite color images and temporal super-resolution reconstructions. The dynamic area of the scene (c), with the beating heart, has been manually selected and inside of (c), the frame rate is twice that of outside. This illustrates the ability to choose between fast single hue imaging and slow color imaging. (d) Reconstructions at the location shown on (c) with a heart symbol (♥) using least-squares (without regularization, LSTSQ) or ADMM. The TV regularization we used in Eq. (4.9) favors piecewise constant reconstructions and preserves sharp edges. (e) Reconstructions at the location shown on (c) with a club symbol (♣) using LSTSQ or ADMM. At this location, there is little motion of the sample, and the LSTSQ reconstructions oscillate a lot, while the ADMM reconstructions show little motion, justifying the use of ADMM over LSTSQ. Within (c), we assigned a hue to the reconstructed images, which we measured at calibration. Scale bar:  $100\mu\text{m}$ . See [129] Visualization 3 for the full movie.

## Chapter 4. Temporal super-resolution fluorescence light-sheet microscopy via a hue-encoded shutter

---

be synchronous in all slices. For the temporal registration, we used a dynamic programming method [145]. The method finds the best warping function of a temporal series onto another one by maximizing the sum of normalized mutual information between all frames of both time-series, which has already been shown to be well-suited for cardiac images [146, 147, 148]. Visualization 4 in [129] shows a 3D+time rendering that highlights the raw data, where motion is encoded within the color channels, and the doubled frame rate reconstruction.

### 4.4.6 Roadmap to higher super-resolution factors

In this paper, we presented a method to double the frame-rate of imaging in fluorescence microscopy. According to our model, the temporal super-resolution factor is determined by the rank and conditioning number of matrix  $A$  in Eq. (4.9). The rank is upper-bounded by both  $C$ ,  $F$ , and  $L$  (respectively the number of color channels, the number of co-localized fluorophores and the number of lasers at our disposal), so to have a super-resolution factor of, say,  $Q = 3$ , we would need at least three color channels, three co-localized fluorophores and three lasers.

Also, the conditioning number of the matrix  $A$  provides a means to predict the quality of the reconstructions, as we have illustrated in [117]. If the chosen fluorophores have too close light emission spectra, this conditioning number will increase, hence lowering the quality of the reconstruction. In [110], Shaner et al. provide insights on how to choose fluorescent proteins and optical filters for maximal spectral separation, which improves the conditioning of our system. A recommended setup of [110] would have so little spectral cross-talk that we could have  $Q = 3$  with close to a perfect conditioning number, hence good quality reconstructions at three times the frame-rate. This setup recommends using three bandpass detection filters centered at 480 nm (bandpass width 40 nm), 575 nm (bandpass width 25 nm) and 675 nm (bandpass width 130 nm) and the following three co-localized fluorophores: Cerulean (center wavelength of emission 475 nm), mOrange (center wavelength of emission 562 nm) and mPlum (center wavelength of emission 649 nm).

## 4.5 Discussion and Conclusion

In this paper, we investigated whether a hue-encoded shutter method (HESM) to improve the temporal resolution [117] could be applied to fluorescence microscopy. We showed that despite the physical differences between fluorescence (where the illumination spectrum cannot be inferred from the emission spectrum) and light absorption or reflection properties (which directly modulates the illumination spectrum to produce the transmitted or reflected light), HESM can still be used in fluorescence microscopy, provided one can use temporally modulated illumination, a color camera, and samples labeled with co-localized fluorophores



in the dynamic regions where a frame rate boost is desired. We showed imaging of the beating heart of a zebrafish labeled with co-localized red and green fluorescent proteins at twice the acquisition frame rate on a light-sheet microscope, with the ability to preserve the hue-information in static areas. Although we experimentally showed an increase of the frame rate by a factor of 2, our method is general enough that it should allow for higher factors if additional co-localized fluorescent species, lasers, and color channels are available as discussed in Section 4.4.6.

Our use of a low SNR RGB camera leads to the performance of the current implementation of our method to be below that of the highest frame-rates achievable with dedicated high-sensitivity cameras (100–200 fps) built into some light-sheet microscope implementations, we foresee that the use of alternative imaging components (light splitting and multiple high-speed cameras) could lead to even higher frame rates.

A key element that we introduced in this paper for the HESM approach to be sufficiently robust in practice, is the temporal regularization, which can cope with sample labeling inhomogeneities and low signal quality inherent to fluorescence imaging, as shown in Figure 4.7 (d). We further observed that two aspects are particularly important when selecting a fluorescent sample for HESM: (1) the co-localized fluorescent labels should be as homogeneous as possible in the dynamic regions and (2) a static area with a labeling ratio sufficiently similar to the dynamic region is required to calibrate the system. This means that a sample where only moving cells are labeled would not be suitable to our method, as the calibration could not be performed.

In Section 4.4.3, we illustrated the versatility afforded by our method (either slow color imaging or fast monochrome imaging), by applying it to a region of interest surrounding the beating heart of a zebrafish, while preserving the acquired color images outside of the region. Furthermore, the added possibility of using fluorescence opens the use of HESM to sectioning methods that rely on fluorescence (such as light-sheet microscopy). We illustrated the benefits of a doubled frame rate in the reconstruction of the beating heart in four dimensions (3D + t).

Our method is generic enough that it could potentially speed-up other fluorescence microscopy methods, provided samples with co-localized fluorophores can be generated and multiple lasers can be modulated in time at high-speed, in synchrony with the color camera.



# 5 Generalized temporal sampling with active illumination in optical microscopy

This chapter is directly based on our publications in [149] and [150]. The authors are myself and Michael Liebling.

To better locate this paper in the context of the whole thesis, Figure 5.1 illustrates the effect of the method when applied to the schematized heart of Figure 2.3.

## 5.1 Abstract

Generalized sampling is a flexible framework for signal acquisition, which relaxes the need for ideal pre-filters. Nevertheless, implementation remains challenging for dynamic imaging applications because it requires simultaneously measuring multiple overlapping inner-products and because only positive signals (intensities) can be measured by cameras. We present a method to collect videos of monochromatic objects by projecting the incoming signal at each pixel in a temporal B-spline space of degree 0, 1, or 2 by using a conventional RGB camera and a modulated three-color light source for illumination. Specifically, we solve the basis function overlap problem by multiplexing the acquisition in different color ranges and use B-spline pieces (which are positive) as projection kernels of a biorthogonal projection-expansion bases pair. The steps to recover signal samples include spectral unmixing and inverse filtering. Reconstructions we obtained from simulated and experimentally-acquired microscopy data demonstrate the feasibility of our approach.

## 5.2 Introduction

Observing phenomena in live biological samples in microscopy requires sufficient time-resolution [55]. Besides the development of faster and more sensitive cameras and clever

## Chapter 5. Generalized temporal sampling with active illumination in optical microscopy

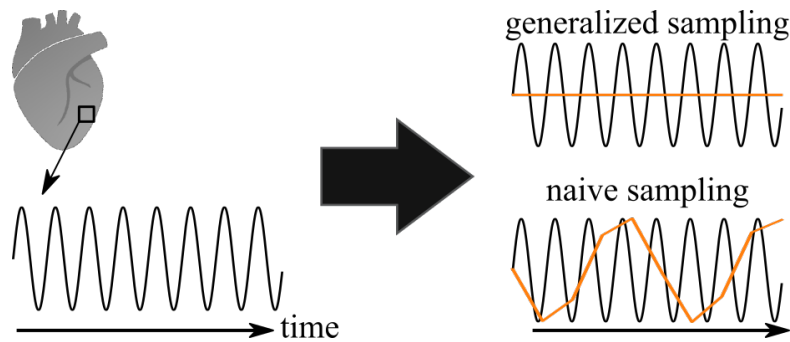


Figure 5.1 – The method presented in this chapter performs temporal generalized sampling imaging. The effect of a sampling scheme are not obvious alone, so we compare generalized sampling with a naive sampling scheme where the Nyquist criterion is not respected. The simulated reconstructions are shown in orange. In the case of generalized sampling, the high-frequency signal is reconstructed as its average value. In the case of naive sampling, we observe aliasing as the reconstructed signal seems to follow a low frequency sine curve.

pixel rebinning methods [75], various sensing and computational approaches to increase the temporal resolution of microscopes have been proposed. Some rely on multiple observations of a signal [56, 57, 58, 59] or make clever use of the signal structure itself, e.g. its sparsity in a known basis [71, 72, 69] or its repeatable nature [73, 74]. The ability to modulate the illumination rapidly in a controlled and cost-effective way (in particular, with LED-based illuminators [32]) also opens the way for promising methods. For instance, short light pulses (stroboscopy) have been used to reduce motion blur [118] or the *fluttered shutter* principle [120, 119] uses a pseudo-random temporal illumination sequence to computationally improve the temporal resolution.

Despite the above developments, many imaging systems still rely on direct image acquisition, which is vulnerable to aliasing if the imaged signal contains frequencies higher than the Nyquist frequency, since perfect low-pass filters cannot be implemented in practice. Generalized sampling [106] offers a framework to implement sampling operations that relaxes the need for ideal filters. Applications that build upon this framework have been proposed in optics [151] or to sample signals with a finite rate of innovation on multiple channels [152].

Due to the shift-invariant nature of generalized sampling, the implementation of pre-filters in time can be problematic because of the temporal overlap of the inner product kernels. Indeed, if the pre-filter used is longer than a unit of time (sampling interval), several inner-products must be carried out simultaneously, which requires a multiplexed acquisition approach. Moreover, in standard (incoherent light) optical imaging applications, only the intensity of the light, which is always positive can be measured. While modulation is possible by illuminating the sample with a variable intensity over time, this illumination suffers from the same positivity limitations (only positive illumination functions can be considered). In this

paper, we present an approach to overcome the above positivity and multiplexing limitations to carry out generalized sampling in the context of optical microscopy imaging. We propose to use active multicolor illumination and a color camera for collection, allowing spectral multiplexing and ideal prefiltering of the signal. Specifically, we modulate the illumination signal over time with independent signals in different color channels of the illumination lamps, which produces modulated signals whose integration by a camera shutter can be converted to the inner product between the signal and the prefilter kernel. Following recovery of these coefficients and reconstruction of the signal in the projection basis' dual basis, we obtain samples of the incoming signal, projected on the space spanned by a shift-invariant B-spline basis.

This paper is organized as follows. In Section 5.3, we provide a formal description of our problem. In Section 5.4, we derive our method. In Section 5.5, we illustrate our approach on both synthetic signals and from data collected on a transmission wide-field microscope. Finally, we conclude in Section 5.6.

### 5.3 Problem statement

We consider a continuous-time signal  $f(t)$ , of which we want to estimate the least-squares approximation  $\tilde{f}(t)$  in the shift-invariant space spanned by B-splines of degree  $n$ ,  $V = \{\beta^n(\cdot - k), k \in \mathbb{Z}\}$ , which can be obtained via a biorthogonal projection[106]:

$$\tilde{f}(t) = \sum_{k \in \mathbb{Z}} \underbrace{\langle f, \mathring{\beta}^n(\cdot - k) \rangle}_{c[k]} \beta^n(t - k), \quad (5.1)$$

with

$$\langle f, g \rangle = \int_{-\infty}^{\infty} f(t)g(t)dt \quad (5.2)$$

and where  $\mathring{\beta}^n(t)$  is the dual B-spline[107], a function which, in addition to satisfying,

$$\langle \beta^n(\cdot - \ell), \mathring{\beta}^n(\cdot - k) \rangle = \delta[\ell - k], \quad (5.3)$$

also spans the subspace  $V$  (and is therefore unique).

A practical system should therefore provide the measurements  $c_k$ , which correspond to weighted integrals of the input signals. There are two issues when implementing this. First, the  $\mathring{\beta}^n$  have infinite support and hence overlap in time (except for degree  $n = 0$ ), which requires some way of splitting the input signal to perform the inner products in parallel, and, second, the signals in this setting are light intensities, which have to be positive.

To implement the projection settings, we consider a conventional imaging system with a

## Chapter 5. Generalized temporal sampling with active illumination in optical microscopy

---

camera that has  $C$  color channels (e.g. an RGB pixel of a color camera corresponds to  $C = 3$ ). We further assume that the system has  $L$  light sources that uniformly illuminate the scene, each with a different, yet possibly overlapping, color spectrum. The intensity of each light source can be controlled as a function of time and independently. These functions can only be positive (as light intensities are necessarily positive) and their duration should be less than the integration time of each of the camera's frames. We model the imaging system by taking into account the crosstalk that arises from the use of broadband light sources and wide camera (RGB) filters. For a single pixel at time  $k$ , we simultaneously measure the intensities  $y_c[k]$  in channels  $c = 1, \dots, C$ :

$$\begin{pmatrix} y_1[k] \\ \vdots \\ y_C[k] \end{pmatrix} = \begin{pmatrix} \gamma_{1,1} & \cdots & \gamma_{1,L} & d_1 \\ \vdots & \ddots & \vdots & \vdots \\ \gamma_{C,1} & \cdots & \gamma_{C,L} & d_C \end{pmatrix} \begin{pmatrix} a_1[k] \\ \vdots \\ a_L[k] \\ 1 \end{pmatrix} \quad (5.4)$$

or in condensed form:

$$\mathbf{y} = \mathbf{\Gamma} \mathbf{a}, \quad (5.5)$$

where the matrix  $\mathbf{\Gamma}$  contains the crosstalk mixing terms (including an affine offset  $d_c$ ) and the coefficients  $a_\ell[k]$  are the inner products:

$$a_\ell[k] = \langle f, s_\ell(\bullet - k) \rangle. \quad (5.6)$$

where  $s_\ell(t)$  are the positive illumination functions, whose support covers the sensor exposure interval.

With this formulation, the problem of recovering the samples  $c[k]$  in Equation (5.1) from measurements  $y_c[k]$ , can be broken down into the following sub-problems:

1. find suitable illumination functions  $s_\ell$  (in particular, positive and with a finite support) such that the sequence  $c[k]$  can be derived from the multi-channel sequence  $a_\ell[k]$ .
2. determine the coefficients  $c[k]$  from the coefficients  $a_\ell[k]$  (via inverse filtering)
3. determine the coefficients  $a_\ell[k]$  from the  $y_c[k]$  (via spectral unmixing).

We detail these steps in the section below.

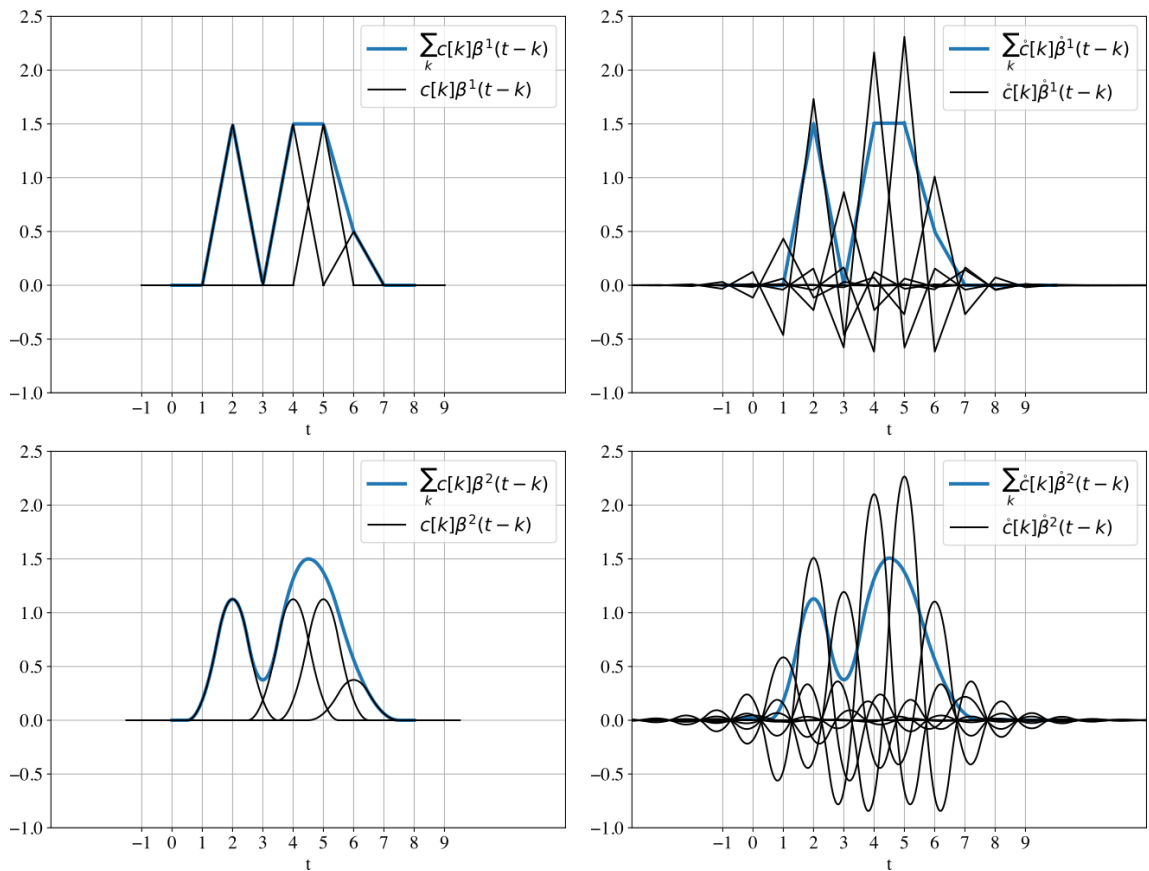


Figure 5.2 – Equivalent basic and dual B-spline representations of the same signal for degrees  $n = 1$  (top row) and  $n = 2$  (bottom row). Notice that both represented signals (in blue in all plots) are equivalent, i.e.  $\sum_k c[k]\beta^n(t-k) = \sum_k \hat{c}[k]\hat{\beta}^n(t-k)$ , while the basic B-spline representation uses functions of finite support.

## 5.4 Methods

### 5.4.1 Multi-color B-spline segments as prefilter kernels

Our goal is to compute the inner products in Eq. (5.1) via active illumination by choosing illumination functions  $s_\ell(t-k)$  appropriately. The challenge of this task is that we cannot use  $s_\ell(t-k) = \hat{\beta}^n(t-k)$  directly (which would be the natural choice) because the dual of a B-spline is not positive for all  $t$  (except when  $n = 0$ ) and  $s_\ell(t)$  being a light intensity, it must be positive. We work around this problem by using an equivalent representation of the projection described in Equation (5.1) and illustrated in Figure 5.2, by switching the role of the dual bases [107] namely:

$$\tilde{f}(t) = \sum_{k \in \mathbb{Z}} \langle f, \hat{\beta}^n(\cdot - k) \rangle \beta^n(t-k) = \sum_{k \in \mathbb{Z}} \langle f, \beta^n(\cdot - k) \rangle \hat{\beta}^n(t-k). \quad (5.7)$$

## Chapter 5. Generalized temporal sampling with active illumination in optical microscopy

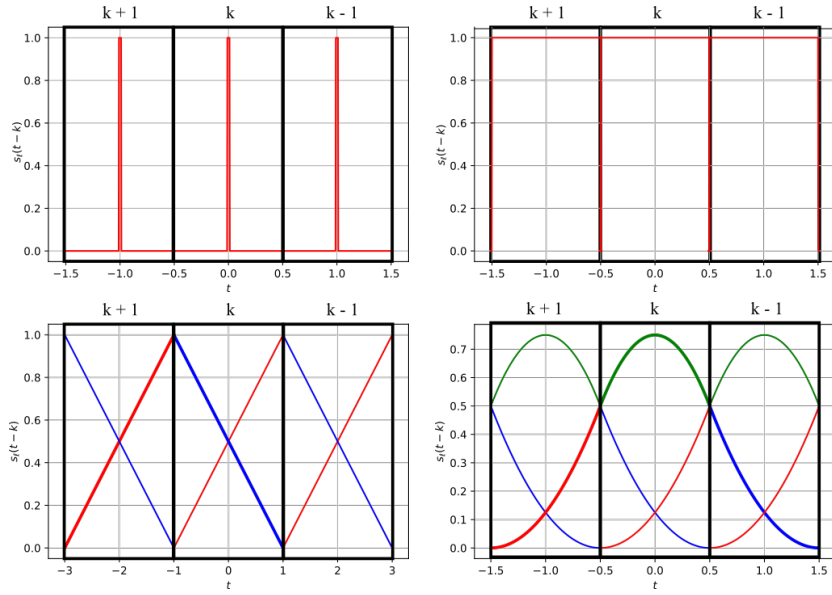


Figure 5.3 – Illumination functions  $s_\ell(t - k)$  over three frames for stroboscopic imaging (top left),  $n = 0$  (top right),  $n = 1$  (bottom left), and  $n = 2$  (bottom right). The color of the line corresponds to the color of the illumination light. For  $n = 1$  and  $n = 2$  (bottom plots), multiple frames are involved to compute a single coefficient  $\hat{c}[k]$  from the coefficients  $a_\ell$ .

Specifically, the coefficients in the dual B-spline basis are given by:

$$\hat{c}[k] = \langle \beta^n(\cdot - k), f \rangle = \int_{-\frac{n+1}{2}}^{\frac{n+1}{2}} \beta^n(t - k) f(t) dt, \quad (5.8)$$

where we note that all involved functions are positive and, since the B-spline have a finite support, the inner-product can be computed over a finite interval. Nevertheless, since the support of B-splines of degree  $n$  is  $n + 1$ , we have  $n + 1$  shifted B-splines that overlap in the signal representation at any given time (see Figure 5.2) making the sequential computation of the  $\hat{c}[k]$  problematic. In order to still acquire several inner products simultaneously, we spectrally multiplex the measurements according to Equation (5.4), by splitting each B-spline into  $n + 1$  regions, which gives the following illumination functions  $s_\ell(t)$ , for  $n$  illumination sources ( $\ell = 1, \dots, n$ ); for  $n = 0$ , we have

$$s_1(t) = \beta^0(t); \quad (5.9)$$



for  $n = 1$ , we have:

$$s_1(t) = \begin{cases} \beta^1(t) = 1 - t, & 0 < t < 1 \\ 0, & \text{otherwise,} \end{cases} \quad (5.10)$$

$$s_2(t) = \begin{cases} \beta^1(t - 1) = t, & 0 < t < 1 \\ 0, & \text{otherwise;} \end{cases} \quad (5.11)$$

and for  $n = 2$ , we have

$$s_1(t) = \begin{cases} \beta^2(t + 1) = \frac{1}{2}(\frac{1}{2} - t)^2 & -1/2 < t < 1/2 \\ 0, & \text{otherwise,} \end{cases} \quad (5.12)$$

$$s_2(t) = \begin{cases} \beta^2(t) = \frac{3}{4} - t^2, & -1/2 < t < 1/2 \\ 0, & \text{otherwise,} \end{cases} \quad (5.13)$$

$$s_3(t) = \begin{cases} \beta^2(t - 1) = \frac{1}{2}(\frac{1}{2} + t)^2 & -1/2 < t < 1/2 \\ 0, & \text{otherwise,} \end{cases} \quad (5.14)$$

where

$$\beta^2(t) = \begin{cases} \frac{1}{2}(\frac{3}{2} - |t|)^2, & \frac{1}{2} < |t| < \frac{3}{2} \\ \frac{3}{4} - t^2, & |t| \leq \frac{1}{2} \\ 0, & \text{otherwise.} \end{cases} \quad (5.15)$$

Figure 5.3 shows the illumination functions over three consecutive acquired frames for  $n = 0$ ,  $n = 1$ , and  $n = 2$ . The color of the line corresponds to the color of the illumination. Notice that in order to reconstruct  $\hat{c}[k]$  we have to combine measurements over multiple frames (see the bold lines in Fig. 5.3 for  $n = 1$  and  $n = 2$ ).

The red illumination is light 1 ( $a_1$ ), the blue illumination is light 2 ( $a_2$ ) and the green illumination is light 3 ( $a_3$ ). For degrees  $n = 0, 1$  and 2 the coefficients  $\hat{c}[k]$  can be recovered from  $a_\ell[k]$  as described below (assuming mirror boundary conditions).

**Degree  $n = 0$ :**

$$\hat{c}[k] = a_1[k] \quad (5.16)$$

**Degree  $n = 1$ :**

$$\hat{c}[k] = \begin{cases} a_1[k] + a_2[k + 1], & 0 \leq k < K - 1 \\ 2a_1[K - 1], & k = K - 1 \end{cases} \quad (5.17)$$

**Degree  $n = 2$ :**

$$\hat{c}[k] = \begin{cases} a_1[k-1] + a_3[k] + a_2[k+1], & 1 \leq k < K-2 \\ a_2[0] + a_3[0] + a_2[1], & k = 0 \\ a_1[K-1] + a_1[K-1] + a_1[K-2], & k = K-1 \end{cases} \quad (5.18)$$

### 5.4.2 Spectral unmixing

The spectral unmixing procedure is similar to the setting described in [117]. Specifically, we recover the vector  $\mathbf{a}$  by solving the minimization problem:

$$\mathbf{a}^* = \min_{\mathbf{a}} \|\mathbf{Y} - \mathbf{d} - \Gamma \mathbf{a}\|_2^2. \quad (5.19)$$

### 5.4.3 Converting to samples

We obtain the basic B-spline representation through filtering of the coefficients in the dual-spline representation [107]:

$$c[k] = (b^{2n+1})^{-1} * \hat{c}[k]. \quad (5.20)$$

We can further obtain samples by carrying out interpolation

$$\tilde{f}[k] = \tilde{f}(t)|_{t=k} = c * b_1^n[k], \quad (5.21)$$

where

$$b_1^n[k] = \beta^n(t)|_{t=k}. \quad (5.22)$$

## 5.5 Experiments

### 5.5.1 Reconstructions from synthetic data

We conducted an experiment to illustrate the impact of the chosen sampling basis. We generated a 1D signal containing shifted B-splines of various degrees, shown on Figure 5.4. We then simulated active sampling using B-splines of degrees 0 to 2 as pre-filters. Figure 5.4 shows the reconstructions obtained by sampling the signal on the top left of the figure. We observe that the B-splines in the sampled signal are perfectly reconstructed when the pre-filter is of the same degree than the B-spline. We also see overshooting and ringing after sharp transitions, for degrees  $n \geq 1$ .

We set out to investigate the effect of our method in the presence of high frequencies, which we compared to a stroboscopic imaging system. We generated a 1D temporal chirp signal and

$$\beta^0(t-5) + \beta^1(t-10) + \beta^2(t-15) + \beta^3(t-20)$$

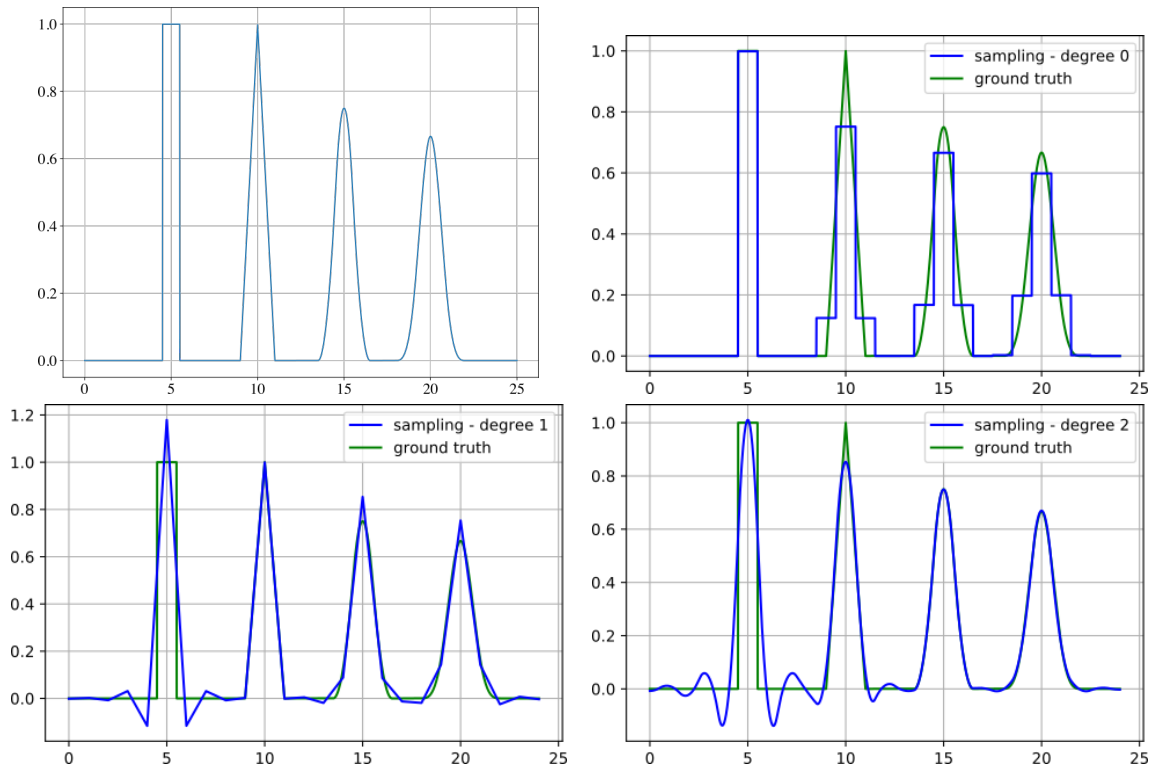


Figure 5.4 – Shifted B-splines of degrees 0, 1 and 2. We observe that each B-spline is perfectly reconstructed when the sampling is done with B-splines of the same degree.

## Chapter 5. Generalized temporal sampling with active illumination in optical microscopy

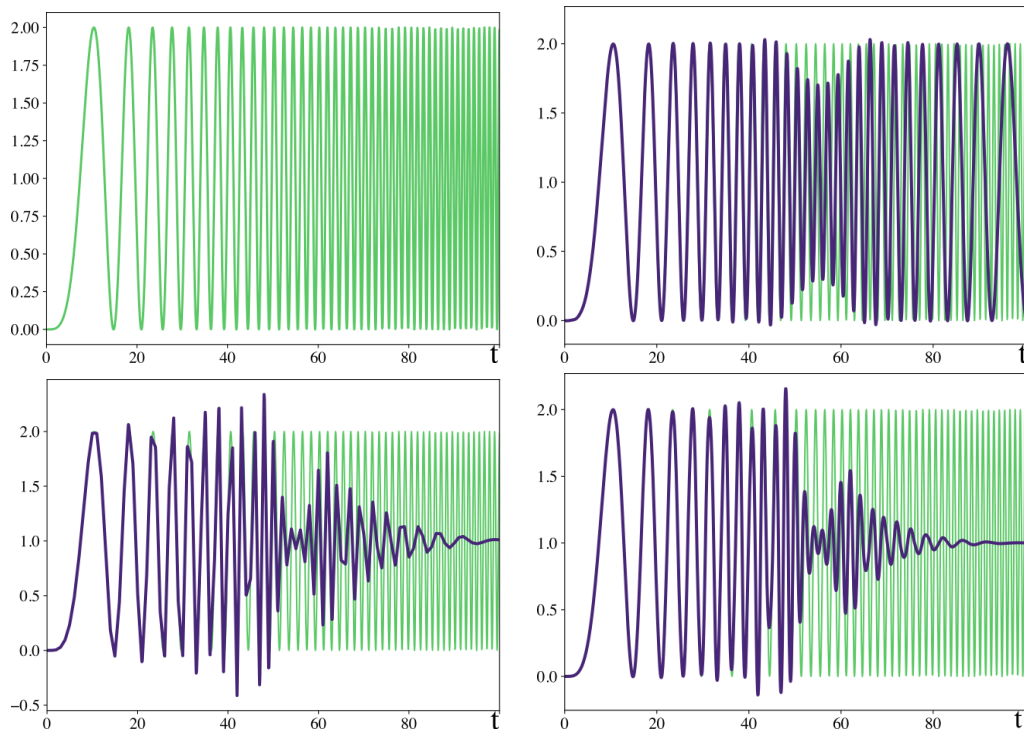


Figure 5.5 – Sampling simulations of the signal  $f(t) = 1 + \sin(\frac{t^2}{35} + \frac{\pi}{2})$  (top left). We simulated stroboscopic imaging (top right) and generalized sampling with B-splines of degree 1 (bottom left) and 2 (bottom right). Notice that the B-spline sampling reconstructions for high frequencies ( $t \geq 80$ ) goes to the average of the signal, while the stroboscopic imaging shows aliasing.

simulated sampling with B-splines of degree 2 as well as stroboscopic imaging. The signal and sampling simulations are shown on Fig. 5.5, where we notice that stroboscopic imaging is strongly subject to aliasing, while generalized sampling by projection on B-spline bases gracefully handles higher frequencies.

### 5.5.2 Rotating chirp

We used a printed black and white grid that we rotated using a stepper motor (Nema 14, Bipolar, Stepper Online, China) controlled by a micro-controller (Arduino Due, Arduino, Italy) through a power driver module (L298N dual H-bridge driver chip, Electronicmodule Store, China). We incrementally increased the grid's rotation speed by steps, while acquiring images with either stroboscopic illumination or using the illumination functions shown in Figure 5.3. The exposure time was set to  $E = 200ms$ . We then used the method presented in Section 5.4.1 to reconstruct image series and compared them to those obtained via stroboscopic imaging (Figure 5.6). Fig. 5.6(a)-(d) show acquired images using either stroboscopic imaging (a) or

B-spline sampling with degrees 0 to 2 (b)-(d). Fig. 5.6(e) shows a graph with all reconstructions over time at the same location, marked with a cross (“X”) on (a)-(d). Fig. 5.6(f)-(i) show reconstructed images when the grid was rotating at high speed. We can see strong temporal aliasing in (f) as the grid appears to be almost static over consecutive frames, although it has undergone multiple rotations. On Fig. 5.6(g)-(i), the rotating grid takes the aspect of a uniform gray disk, with minor intensity variations where aliasing is slightly visible. This experiment shows that the sampling scheme presented in Section 5.4.1 does not allow for perfect sampling, which would be free of aliasing and motion-blur. Nevertheless, the pre-filter is optimal for the sampling in the bases in which we sample (project) the imaged signal, hence the reconstructions of (g)-(i) are the optimal representations of the signal in our chosen B-spline bases. In other words, even if our reconstructions are not perfect, they are more reliable than that of Fig. 5.6(f). Similarly to the experiment in Section 5.5.1, we can see that the reconstructions on Fig. 5.6(e).

### 5.5.3 Microscopy

We set out to investigate if our method could be implemented in optical microscopy. Specifically, we considered bright field and fluorescence (light-sheet) microscopy. We further investigated the feasibility of using this method for in vivo imaging of dynamic processes, specifically, to image the beating heart of zebrafish embryos.

#### Hardware and parameters setup

For bright-field microscopy (experiments in Section 5.5.4), we implemented the illumination scheme with commonly available and cost-effective hardware. We assembled a light source using a 6-LED chip (SLS Lighting RGBWA+UV, Aliexpress, China). We drove the red ( $\lambda \approx 620\text{nm}$ ), green ( $\lambda \approx 525\text{nm}$ ) and blue ( $\lambda \approx 465\text{nm}$ ) LEDs via a micro-controller (Arduino Uno, Arduino, Italy), which we programmed to generate the illumination time-pattern shown on Figure 5.3, individually controlling each color. For the LED and camera synchronization, the micro-controller monitored the *flash* trigger output of the camera. Whenever the trigger signal transitions from low to high state, the micro-controller starts the time-sequence of the LEDs for the frame about to be recorded. The LEDs were directly powered by the controller’s outputs, without additional power amplification of the signal.

For fluorescence microscopy (experiments in Section 5.5.5), we used an implementation of the OpenSPIM light-sheet microscope [33], with two lasers (Stradus, Vortran Laser Technology) of wavelengths 488nm and 561nm to generate the excitation illumination light sheet. Again, we used a micro-controller (Arduino Uno) to modulate the laser intensities over time, using pulse-width modulation control on their fast ON/OFF electrical connexion to generate the

## Chapter 5. Generalized temporal sampling with active illumination in optical microscopy

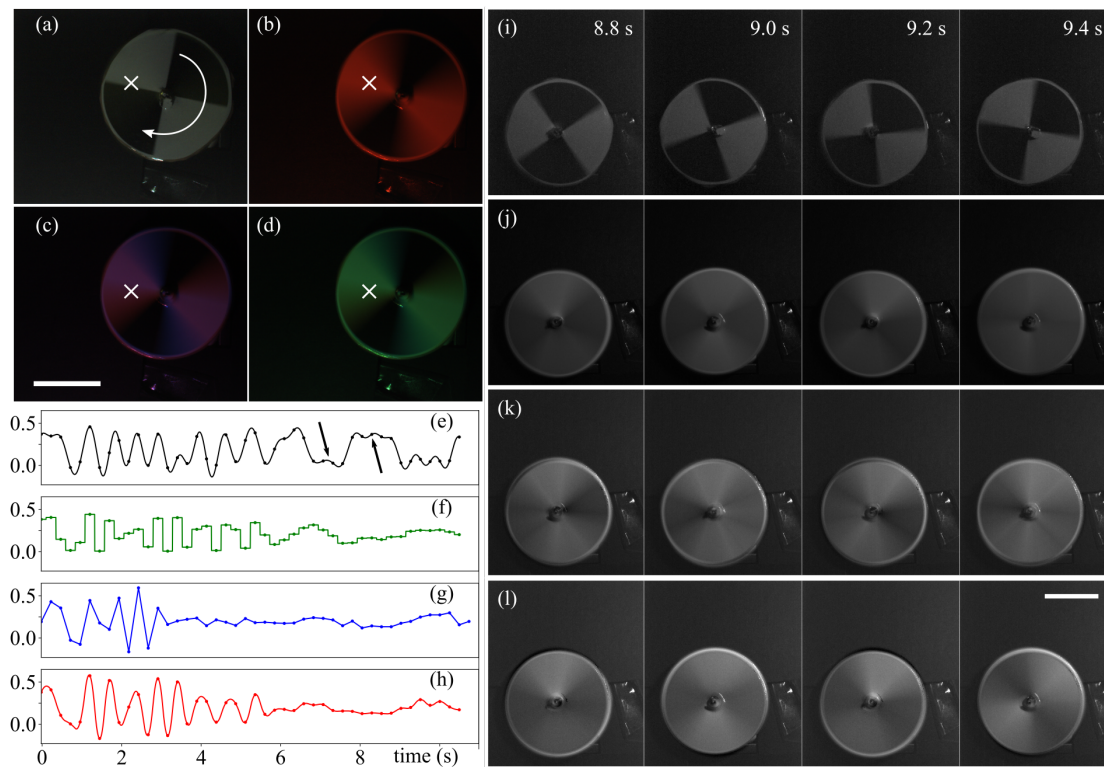


Figure 5.6 – Rotating grid imaged using various sampling methods. The grid is visible on (a). (a)-(d) acquired images at the same speed and position of the grid. The rotating arrow in (a) shows the rotation direction. The speed was increasing with the time. (a) was acquired with a stroboscopic illumination. (b)-(d) were acquired using B-splines as pre-filters of order 0 (b), 1 (c) and 2 (d). (e)-(h) show all reconstructions over time at the same location marked with an “X” on (a)-(d). Notice that on (e) (stroboscopic case), for  $t > 6$ , the plot oscillates between the maximal and minimal values (corresponding to white and black in the image), indicated with black arrows, while in (f)-(h) (generalized sampling cases), the plots tends to the average value (grey in the images). (i) images acquired with the stroboscopic illumination when the grid was rotating fast. Strong aliasing is visible, as between consecutive frames the grid appears to have moved very little, while it has made more than one rotation between each frame. (j) reconstructions with B-spline pre-filters of degree 0. (k) reconstructions with B-spline pre-filters of degree 1. (l) reconstructions with B-spline pre-filters of degree 2. The images in (j)-(l) show little to no aliasing: the rotating grid becomes a uniform gray disk, as is consistent with the simulation in Figure 5.5. Full movie available online [129], Visualization 1. Scale bars: 2 cm.

illumination functions in Figure 5.3 up to degree 1 (the highest degree achievable with only 2 lasers).

For both the bright-field and fluorescence experiments, we used a CMOS color camera (Thorlabs DCC3240C, Thorlabs, Germany) with  $1280 \times 1024$  pixels and a standard RGGB-Bayer filter pattern. We attached the camera to the camera port of our microscope (for both transmission and light-sheet microscopy) consisting of a  $20\times$  Olympus water dipping lens (Olympus Plan Fluorite UMPLFLN  $20\times$ W) combined with a 180mm tube lens (Olympus U-TLU-1-2) and terminated by a  $0.5\times$  zoom lens (Olympus U-TV0.5XC-3).

For imaging, we embedded 3 dpf zebrafish larvae, anesthetized with 0.1% tricaine (ethyl 3-aminobenzoate methanesulfonate salt, Sigma), in low melting agarose.

#### 5.5.4 Generalized sampling of the beating heart of the zebrafish under transmission microscopy

To illustrate the applicability of our method for biological bright field microscopy, we imaged the beating heart of the zebrafish larva with transmission illumination. We first acquired images of the beating heart using stroboscopic imaging then repeated the acquisition using the generalized sampling method from Section 5.4 with degrees 0, 1, and 2. The exposure time was set to  $E = 60ms$ . Figure 5.7 shows 3 consecutive images either acquired with a strobed illumination (Fig. 5.7(a)) or using temporal generalized sampling (Fig. 5.7(b)-(d)).

Although the strobed illumination (Fig. 5.7(a)) produces slightly sharper images, this approach is subject to aliasing at high frequencies. This means that even though the image appears sharper, one cannot trust the observed motions to be representative of the actual motion sequence of the heart. Although the images obtained with our proposed method (Fig. 5.7(b)-(d)) exhibit stronger motion blur than those obtained with strobed light, one can be confident that the perceived motion is accurate.

#### 5.5.5 Generalized sampling of the beating heart of the zebrafish on light-sheet fluorescent microscopy

We set out to investigate whether our generalized sampling method is applicable to fluorescence microscopy. To take advantage of the temporally-modulated color illumination, we imaged a zebrafish that co-expresses ubiquitous cytoplasmic green fluorescent protein, EGFP, and red fluorescent protein, mCherry [143, 131]. Taking advantage of the fluorophores being co-localized we computed the inner products in Eq. (5.8) simultaneously and used the method of Section 5.4 to perform temporal generalized sampling.

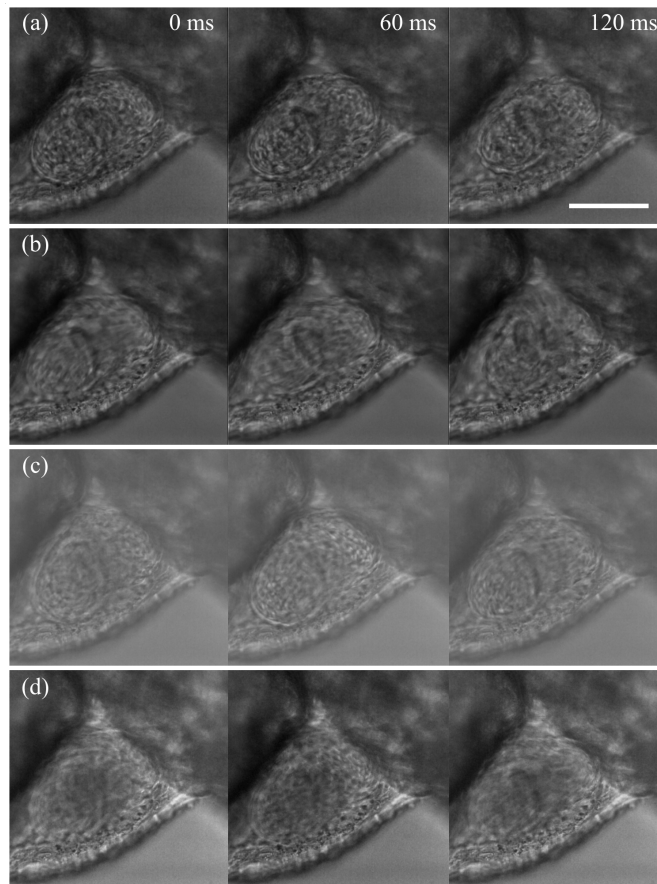


Figure 5.7 – Generalized sampling of a 3 dpf zebrafish beating heart under transmission microscopy. (a) Three consecutive frames of stroboscopic imaging. (b)-(d) Three consecutive reconstructed frames using our method in Section 5.4 for B-spline sampling of degrees 0 (b), 1 (c), and 2 (d). There are no obvious differences between (a)-(d), (a) is slightly sharper than (b)-(d) due to the short light pulse. Full movie in Visualization 2 [129]. Scale bar: 100  $\mu\text{m}$ .

We acquired images of the beating heart of the zebrafish first using stroboscopic imaging, then, via the generalized sampling method from Section 5.4 with degrees 0 and 1. The exposure time was set to  $E = 60\text{ms}$ . Since we had only two lasers and two fluorophores in our system, only generalized sampling up to degree 1 was possible.

Figure 5.8 shows 3 consecutive images acquired with either the strobed illumination (Fig. 5.7(a)) or our method (Fig. 5.7(b),(c)).

Similarly to the experiment in Section 5.5.4 for transmission microscopy, the strobed illumination produces slightly sharper images. However, the strobed image sequence is subject to stronger aliasing.



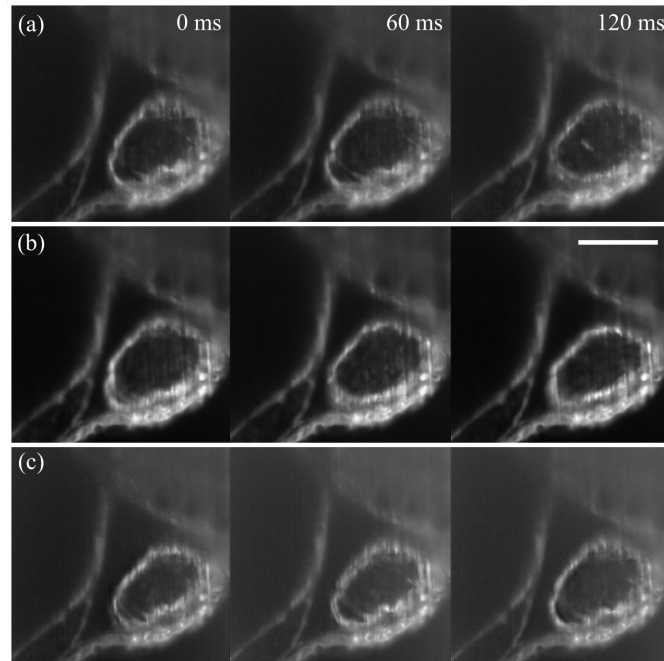


Figure 5.8 – Generalized sampling of a 3 dpf zebrafish beating heart under light-sheet fluorescence microscopy. (a) Three consecutive frames of stroboscopic imaging. (b),(c) Three consecutive reconstructed frames using our method in Section 5.4 for B-spline sampling of degrees 0 (b) and 1 (c). There are no obvious differences between (a)-(c), while the reconstructions in (b) and (c) can be trusted more than (a). Full movie in Visualization 3 [129]. Scale bar:  $100\ \mu\text{m}$ .

## 5.6 Conclusion

We presented a method to perform temporal generalized sampling in optical microscopy. Our approach allows for the use of implementable pre-filters that have finite temporal support and that verify the positivity constraint. Via our proposed spectral multiplexing approach, we could compute multiple inner products simultaneously and, after spectral unmixing, retrieve each individual inner product. Our method leverages the equivalence between basic and dual B-spline representations [107]. Since our method follows the projection framework of generalized sampling, it offers the prospect of avoiding aliasing despite not using ideal pre-filters.

Although the experiments on the beating zebrafish heart of Section 5.5.3 show sharper images using strobed illumination, our method increases the trust one can have in videos as insufficient frame-rate results in motion blur instead, which is visible even in still frames. Using our method, sharp image sequences are therefore more likely to be devoid of temporal aliasing.

Higher degree B-splines have a higher approximation power [153, 154]. Therefore, as high a

## Chapter 5. Generalized temporal sampling with active illumination in optical microscopy

---

degree as possible would be preferable. The highest achievable degree, in our experimental setting with an RGB color camera, was 2 since we could compute no more than three simultaneous inner products. While this paper focused on implementing B-spline pre-filters, our method of computing multiple inner products simultaneously could be extended to other sensing methods, provided the modulation functions are positive and have finite support.

Our experimental implementation relies on a global shutter camera. That is, all pixels share the same integration time and no light is captured by the sensor during the readout (when the image is transferred from the camera to the computer). On the camera we used, this readout time is about 3 milliseconds for images of resolution 500x500 pixels. This implies that the partition of unity [106] condition is not strictly respected. Nevertheless, in practice, this did not visibly affect our method. Some rolling shutter cameras permit continuous exposure of the sensor, where lines are sequentially exposed and transferred to the computer, but would require additional adaptation to take this exposure sequence into account.

# 6 Multi-Spectral Widefield Microscopy of the Beating Heart through Post-Acquisition Synchronization and Unmixing

This section is directly based on our publication in [148]. The authors are myself, Linda Bapst-Wicht, Daniel Schorderet and Michael Liebling. M. Liebling and I had the original idea of the method and implemented it. L. Bapst-Wicht provided us with the zebrafish embryos for the experiment in Section 6.5.2 and she wrote the first paragraph about fish breeding in Sec. 6.5.2. Prof. D. Schorderet is with the *Institut de Recherche en Ophthalmologie*, Sion, Switzerland. He is the supervisor of L. Bapst-Wicht. M. Liebling and I wrote the draft of the manuscript and all authors discussed the results and contributed to the final manuscript.

To better locate this paper in the context of the whole thesis, Figure 6.1 illustrates the effect of the method when applied to the schematized heart of Figure 2.3.

## 6.1 Abstract

Multi-spectral imaging allows distinguishing biological structures. For cardiac microscopy, available devices are either too slow or require illumination intensities that are detrimental to the sample. We present a method for spectral super-resolution imaging of samples whose motion is quasi-periodic by sequentially acquiring movies in wavelength ranges with filters of overlapping bands. Following an initial calibration procedure, we synchronize and unmix the movies to produce multi-spectral sequences. We characterized our approach to retrieve the transmittance of a colored microscopic target whose motion we controlled, observing measurements within of 10% that of a reference spectrometer. We further illustrate our approach to observe the beating embryonic zebrafish heart, demonstrating new possibilities for studying its development.

## Chapter 6. Multi-Spectral Widefield Microscopy of the Beating Heart through Post-Acquisition Synchronization and Unmixing

---

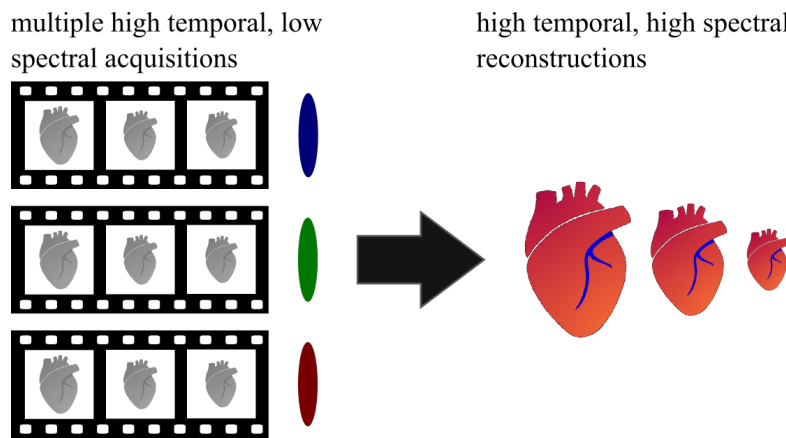


Figure 6.1 – Our method in this chapter performs spectral imaging of the beating heart by combining multiple videos acquired with various filters.

### 6.2 Introduction

Live cardiac imaging in the developing heart is a complex task as the heart beats while it develops and illumination must be limited to prevent damage to the sample. Multi-spectral imaging could benefit the study and differentiation of cardiac structures but as the available light is limited, multi-spectral imagers require operation times that are too slow for cardiac applications.

We propose a method to perform multi-spectral imaging of the beating heart by acquiring a set of movies of the beating heart over multiple heartbeats, each recording a signal filtered in different (and possibly overlapping) range of wavelengths. From these multi-channel data, we build a single multi-spectral movie of the beating heart through temporal registration of the movies followed by color unmixing to yield non-overlapping wavelength ranges (Fig. 6.2).

The importance of multi-spectral imaging in wide-field (non-fluorescence) microscopy and biomedical imaging has been identified in the past. Aach et al. [155] detected cancerous cells through spectral imaging. Blasinski et al. [156] have shown that spectral imaging improves the classification accuracy of ablated heart tissue using machine learning.

Spectral cameras typically acquire multiple images sequentially with narrow-band filters or split the incoming light onto multiple sensors, based on the wavelength [157]. While the first solution makes the imaging process slow, hence unsuitable to image dynamic sample, the second solution trades spatial resolution or signal intensity for spectral resolution. Also, building such cameras requires high opto-mechanical precision and little flexibility for the end user to adjust to particular wavelength ranges.

To overcome these limitations, methods to achieve spectral imaging through computational

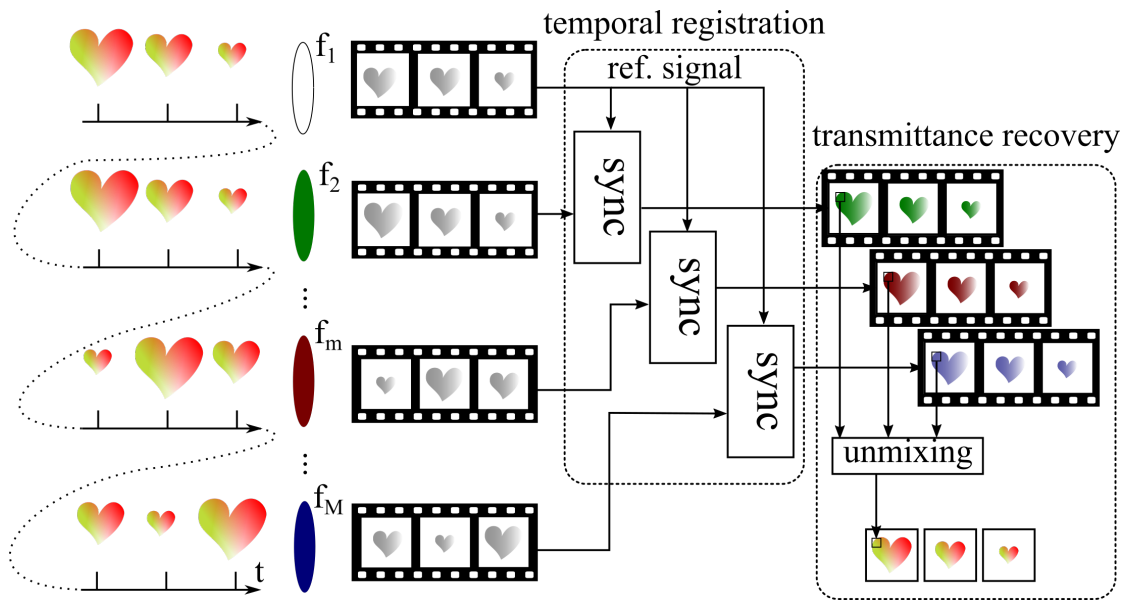


Figure 6.2 – Overview of the method: (1) we acquire  $M$  movies of a live beating heart with  $M$  different filters, where the first filter is an all-pass that serves as registration reference; (2) we register all acquired movies to the reference sequence; (3) we perform unmixing pixel-by-pixel in order to retrieve a multispectral movie of the beating heart.

approaches with less constraining hardware have been proposed. For example, multiple observations of the same scene, observed through a set of colored filters are combined to reconstruct a multi-spectral view [158, 159, 160]. Other approaches have considered spectral imaging as an interpolation or a learning process, using priors on the signal to be reconstructed [161, 162, 71].

Here, we build upon the former class of methods (direct unmixing) that we combine with the multi-channel synchronization step described in Ohn et al. [147] for cardiac imaging of multiple fluorescence channels imaged one after the other, with a brightfield movie as the common reference to synchronize movies collected in 6 bands.

The contributions of this work are (i) presentation of a pipeline to sequentially collect and process multi-spectral images of the beating heart (described in Sections 6.3 and 6.4), (ii) characterization of the proposed approach on a controlled dynamic microscopy sample (Section 6.5) and (iii) demonstration of the applicability for imaging the beating heart of a zebrafish (Section 6.5.2). We discuss results and conclude in Section 6.6.

### 6.3 Problem Statement

We consider a multispectral,  $T$ -periodic signal  $s$  such that:

$$s(\mathbf{x}, \lambda, t) = s(\mathbf{x}, \lambda, t + T), \quad \text{for all time } t \in \mathbb{R}, \quad (6.1)$$

where  $\mathbf{x} = (x_1, x_2)$  are spatial coordinates and  $\lambda$  the wavelength. The signal  $s$  represents the transmissivity of a sample to incoming light over time. We further consider  $M$  movies:

$$y_m[\mathbf{k}, \ell] = \sum_{\lambda_1, \dots, \lambda_N} a_m[\lambda_n] s(\mathbf{k}\Delta x, \lambda_n, \ell\Delta t + \tau_m) + c, \quad (6.2)$$

with pixels indexed by  $\mathbf{k} = (k_1, k_2) \in \mathcal{K} = \{0, \dots, K_1\} \times \{0, \dots, K_2\}$ , frames indexed by  $0 \leq \ell < L$ ,  $\Delta x$  and  $\Delta t$  the sampling steps in space and time, respectively. The factors  $a_m$  incorporate the combined effect of illumination source, bandpass filters (indexed by  $m \in \{1, \dots, M\}$ ), and the spectral response and gain of the camera.  $c$  is a scalar offset of the camera and  $\tau_m$  is a delay that describes the fact that we acquire movies with different filters in different cardiac cycles, starting at an arbitrary (non-triggered and unknown) cardiac phase. We further assume that the movie duration covers at least a full heartbeat, i.e., we have  $L > T/\Delta t$ .

The problem we address is to determine an estimate  $\tilde{s}$  of the multi-spectral transmission function of the sample  $s$  such that  $\tilde{s}[\mathbf{k}, \lambda_n, \ell] \approx s(\mathbf{k}\Delta x, \lambda_n, \ell\Delta t)$ , for  $\mathbf{k} \in \mathcal{K}$ ,  $\lambda_n \in \{\lambda_1, \dots, \lambda_N\}$  and  $0 \leq \ell < \lfloor T/\Delta t \rfloor$  given the  $M$  movies  $y_m[\mathbf{k}, \ell]$  in Equ. (6.2).

### 6.4 Methods

Our methods cover the determination of the unknown time-delays between channel acquisitions ( $\tau_m > T$ ), spectral unmixing to invert Equ. (6.2), and a calibration procedure to determine the factors  $a_m[\lambda_n]$ .

#### 6.4.1 Temporal registration of movies acquired with different filters

Since we collect the spectral response (channels) in different cardiac cycles without any caring signal, before we can merge the channels to obtain the spectral transmission we first need to temporally synchronize the movies.

We proceed to the registration using a method described before by Liebling et al. [145] and, in particular, Ohn et al. [146, 147] for the problem of synchronizing microscopy image series of the beating heart imaged of differing contrasts. Briefly, for each of the  $M$  movies  $y_m$  corresponding to the  $M$  channels, the method determines the shifts  $\tau_m$  such that the  $P$  frames that we aim to reconstruct (and which cover a cardiac heartbeat) maximize the normalized

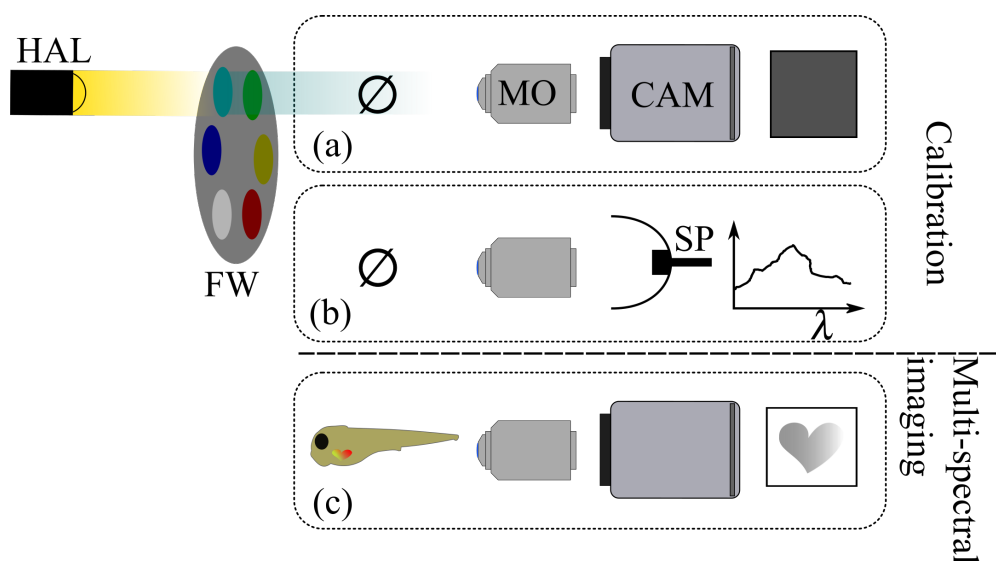


Figure 6.3 – Setup for the acquisition of data; MO: microscope objective, HAL: halogen lamp, CAM: camera, SP: spectrometer, FW: filter wheel. For the calibration, we both use (a) a camera or (b) a spectrometer at the measuring end of the setup, with no setup. After calibration, the system may be used for spectral imaging with dynamic samples (c).

mutual information between the movie of the channel to be registered, shifted by a candidate shift, and the reference channel (which we take to be a movie acquired using a broadband illumination):

$$\tilde{\tau}_m = \operatorname{argmin}_{\tau} \sum_{\ell=1}^P \operatorname{NMI}(y_m[\cdot, \ell - \tau / \Delta t], y_0[\cdot, \ell]), \quad (6.3)$$

where  $\operatorname{NMI}(a, b)$  is the normalized mutual information [163, 146] between two images. After we determine the estimates  $\tilde{\tau}_m$ ,  $1 \leq m \leq M$ , we apply them to obtain synchronized movies  $\tilde{y}_m[\mathbf{k}, \ell] = y_m[\mathbf{k}, \ell - \tilde{\tau}_m / \Delta t]$ ,  $\mathbf{k} \in \mathcal{K}$  and  $0 \leq \ell < P$ .

### 6.4.2 Spectral imaging/unmixing

Given synchronized movies in  $M$  channels, we can consider the spectral recovery problem as a point-wise problem and we drop the spatial ( $\mathbf{k}$ ) and temporal ( $\ell$ ) dependency for brevity. Our aim is to reconstruct a discrete transmission spectrum  $\mathbf{s} = (s_{\lambda_1}, \dots, s_{\lambda_N})^\top = (s(\lambda_1), \dots, s(\lambda_N))^\top$ . We start by describing the acquisition model in more detail, considering our imaging system that consists of a monochrome camera, an illumination source, and  $M$  interchangeable filters (Fig. 6.3). Combining the effect of the wavelength-dependent light source emission intensity  $e_{\lambda_n}$ , transmissivity  $f_{m, \lambda_n}$  of the  $m^{\text{th}}$  filter and the spectral response  $g_{\lambda_n}$  of the camera, the

## Chapter 6. Multi-Spectral Widefield Microscopy of the Beating Heart through Post-Acquisition Synchronization and Unmixing

---

measured intensity at a pixel is:

$$y_m = c + \sum_{\lambda_1, \dots, \lambda_N} \underbrace{g_{\lambda_n} e_{\lambda_n} f_{m, \lambda_n}}_{a_m[\lambda_n]} s_{\lambda_n}, \quad (6.4)$$

where we identified the factors  $a_m[\lambda_n]$  of Equ. (6.2). In matrix form, with  $\mathbf{y} = (y_1, \dots, y_M)^\top$ , we can write:

$$\mathbf{y} = \mathbf{F}\mathbf{G}\mathbf{s} + \mathbf{c}, \quad (6.5)$$

with

$$\mathbf{F} = \begin{pmatrix} f_{1, \lambda_1} e_{\lambda_1} & \dots & f_{1, \lambda_N} e_{\lambda_N} \\ \vdots & \ddots & \vdots \\ f_{M, \lambda_1} e_{\lambda_1} & \dots & f_{M, \lambda_N} e_{\lambda_N} \end{pmatrix}, \quad (6.6)$$

$$\mathbf{G} = \text{diag}(g_{\lambda_1}, \dots, g_{\lambda_N}), \quad \mathbf{c} = c \mathbf{1}_{M \times 1}.$$

With these notations, we formulate the problem of retrieving an estimate of the spectral transmittance  $\tilde{\mathbf{s}}^*$  of the sample can be formulated as the solution to a minimization problem:

$$\tilde{\mathbf{s}}^* = \underset{\mathbf{s}}{\text{argmin}} \|\mathbf{y} - \mathbf{c} - \mathbf{A}\mathbf{s}\|_{\ell_1} \quad (6.7)$$

where  $\mathbf{A} = \mathbf{F}\mathbf{G}$ . We solve this problem using a simplex method [164] with the additional constraints that  $0 \leq \tilde{s} \leq 1$ . Detailed information about how to solve Equation (6.7) is given in the Appendix B.

### 6.4.3 Calibration of the imaging system

Before solving Equation (6.7), we must calibrate the system to populate matrices  $\mathbf{F}$  and  $\mathbf{G}$ . We use a spectrometer to directly measure the combined spectral response of each filter with the light source spectrum (Fig. 6.3 (b)) and populate the  $M$  rows of  $\mathbf{F}$ . To calibrate  $\mathbf{G}$ , we place the camera in the acquisition setup (Fig 6.3 (a)) and sequentially acquire  $M$  images with an empty sample holder ( $s_{\lambda_n} = 1$  in Equation (6.4)):

$$\underbrace{\begin{pmatrix} y_{1, \text{cal}} \\ \vdots \\ y_{M, \text{cal}} \end{pmatrix}}_{\mathbf{y}_{\text{cal}}} = \begin{pmatrix} \mathbf{F} & \mathbf{1}_{M \times 1} \end{pmatrix} \text{diag}(g_{\lambda_1}, \dots, g_{\lambda_N}, c) \mathbf{1}_{N \times 1} = \begin{pmatrix} \mathbf{F} & \mathbf{1}_{M \times 1} \end{pmatrix} \underbrace{\begin{pmatrix} g_{\lambda_1} & \dots & g_{\lambda_N} & c \end{pmatrix}}_{\mathbf{g}_{\text{cal}}}^\top. \quad (6.8)$$



To retrieve  $\mathbf{g}_{\text{cal}}^*$ , we solve (with constraint  $0 \leq \mathbf{g}_{\text{cal}}^* \leq 1$ ):

$$\mathbf{g}_{\text{cal}}^* = \arg \min_{\mathbf{g}} \left\| \mathbf{y}_{\text{cal}} - \begin{pmatrix} \mathbf{F} & \mathbf{1}_{M \times 1} \end{pmatrix} \mathbf{g} \right\|_{\ell_1}. \quad (6.9)$$

The algorithm used to solve Equation (6.9) is given in the Appendix B.

## 6.5 Results

We used the transmission line of an OpenSPIM microscope [33], equipped with a condenser and illuminator (Fig. 6.3). We used a halogen light source (Decostar, Osram), a band-pass filter set (*FKB-VIS-40*, Thorlabs) with 5 filters (*FB500-40*, *FB550-40*, *FB600-40*, *FB650-40*, *FB700-40*, Thorlabs) mounted on a 6-position filter wheel (*FW102CNEB*, Thorlabs). The sample was held by a four dimensional stage (*USB 4D-STAGE*, Picard). We used a  $20 \times / 0.5$  water immersion microscopy lens (*UMPLFLN 20xW*, Olympus) coupled to a 180 mm tube-lens (*U-TLU-1-2*, Olympus), a 4Mpixels CMOS camera (*Zyla 4.2 sCMOS*, Andor, Oxford Instruments) and a single pixel CCD spectrometer (*CCS100*, Thorlabs).

### 6.5.1 Experimental validation

**Static validation:** We evaluated the performance of our multi-spectral imaging method by placing color filters (*E009*, *E010*, *E022*, *E036*, *E053*, *E075* filters, *E-colors* set, Rosco Laboratories) in the sample holder and comparing the recovered spectra with those measured directly with the spectrometer. We observed a median error of around 10%.

**Dynamic validation:** we laser-printed a color pattern on a transparency that we mounted on the sample holder (Fig. 6.4(a)). We first reconstructed the transmittance from measurements carried out with the sample at rest (Fig. 6.4(c)). Next, we collected movies of the target displaced laterally with the positioning stage of the microscope, repeating the same motion for each filter, hence generating a pseudo-periodic signal (Fig. 6.4(d)). The recovered spectra in the static and dynamic case concur (Fig. 6.4(b)).

### 6.5.2 Spectral imaging of the beating heart of a zebrafish

To illustrate the potential of our method in practice, we image the heart of a live zebrafish larva. All experiments were approved by the Veterinary service of the State of Valais (Switzerland). We raised and kept zebrafish (wild-type AB zebrafish strain (Zebrafish International Resource Center) under standard laboratory conditions (14/10 hour light/dark cycle, fish water of the system (ZEBTEC Techniplast Aquatic Solution) at  $26.5^\circ\text{C}$  temperature,  $500 \mu\text{s}$  conductivity, and pH 7.3). We raised embryos at  $29^\circ\text{C}$  in standard E3 medium in an incubator (Termaks B8054),

**Chapter 6. Multi-Spectral Widefield Microscopy of the Beating Heart through Post-Acquisition Synchronization and Unmixing**

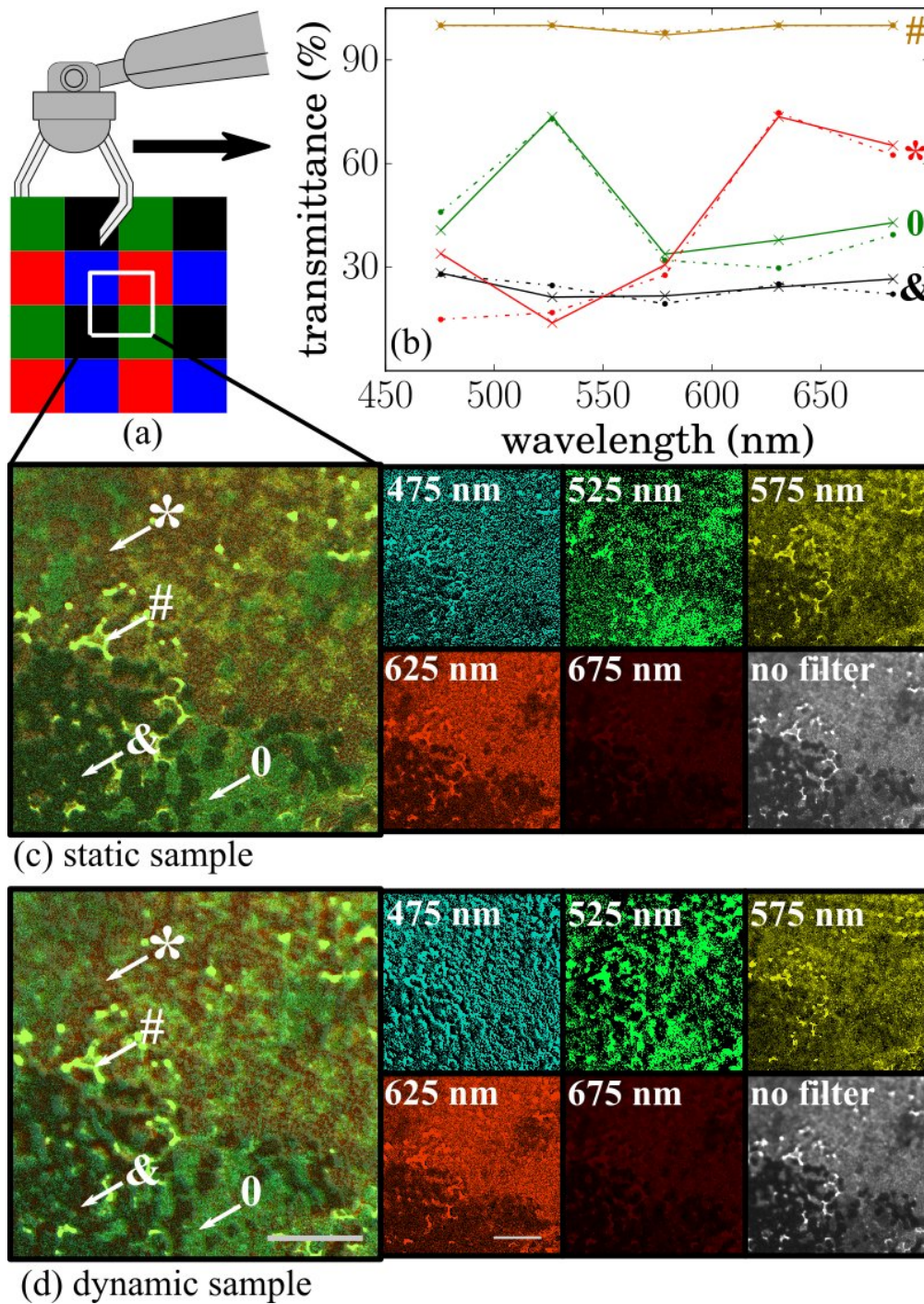


Figure 6.4 – Experimental validation. (a) color target mounted on a motorized sample holder. (b) Spectral transmission calculated in four points from static (solid curve) and dynamic data (dashed curve). (c)-(d) RGB-colored reconstruction, five unmixing wavelength ranges, and acquired bright-field image in (c) static case and (d) dynamic case. Scale bars are 50  $\mu\text{m}$ .

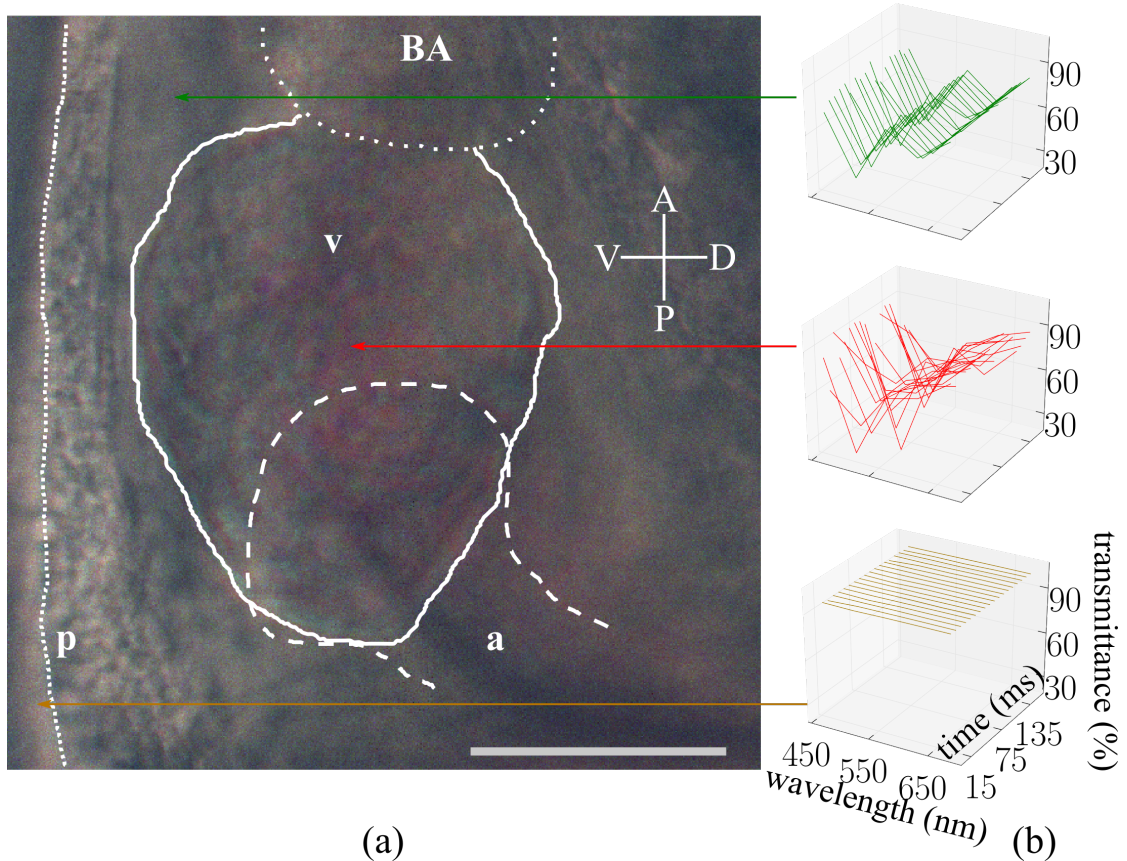


Figure 6.5 – (a) Color rendering of the reconstructed multi-spectral zebrafish heart. The atrium (a), ventricle (v), bulbus arteriosus (BA), and pericardium (p) are outlined. (b) Spectral transmittance computed at times covering a full cardiac period. Scale bar is 100  $\mu\text{m}$ . Full movie is available online [129].

supplemented by 0.003% 1-phenyl 2-thiourea (PTU) from 24 hours post fertilization (hpf) to prevent pigmentation. For imaging, we embedded 48 hpf larvae (hatched from chorion), anesthetized with 0.1% tricaine (ethyl 3-aminobenzoate methanesulfonate salt, Sigma), in low melting agarose for imaging until aged 5 days post fertilization at most. We reconstructed both a color movie and transmittance spectra in multiple areas of the heart (Fig. 6.5) clearly showing spectral variations (background, red blood cells, cardiac tissue).

## 6.6 Discussion and Conclusion

We observed median errors on the recovery of transmittance data around 10%, with averages around 30% due to higher errors at low wavelength ranges where the illumination source provides insufficient intensity. In addition to images with high signal-to-noise (which requires illumination of consistent intensity in all wavelength ranges), for Equations (6.8) and (6.9) to

## **Chapter 6. Multi-Spectral Widefield Microscopy of the Beating Heart through Post-Acquisition Synchronization and Unmixing**

---

be well-posed we must have  $N + 1 \leq M$  (we must have at least one more filter than wavelength range to be recovered) and the filter band should be such that  $F$  has high rank (small overlap between filters). A critical point of the method is the temporal registration of the acquired movies. Poorly synchronized movies lead to worse spectral recovery. In conclusion, we presented and characterized a practical method to perform dynamic multi-spectral microscopy of samples with periodic motion. Results from the beating heart of a zebrafish larva show the potential applicability for studying cardiac dynamics and differentiating tissues and cells.

# 7 Conclusions

In this thesis, we investigated methods to increase temporal resolution, spectral resolution, and flexibility of microscopes by enabling rapid switching between color and fast imaging. We also explored methods to limit temporal aliasing and, thus, increase trust in the observed dynamics.

All our methods rely on the use of active illumination and computational procedures and they are particularly well suited for microscopy as they are simple to implement on existing microscopes with cost-effective hardware.

Moreover, we presented real data, with live samples, which we acquired on our imaging platform for all of our publications, demonstrating the applicability of our methods to microscopy.

## 7.1 Main contributions of the thesis

In Chapter 3 we presented a computational imaging method leveraging a color camera and a multi-spectral active illumination. Each frame includes multiple copies of the signal at various times, encoded in the hue of the image. The computational procedure retrieves a high time-resolution signal, along with the base-hue, under the assumption that the imaged sample has a single color. We characterized our method using robotic arms to generate a repeating sample and presented a temporal super-resolution factor of 2.8 with a threefold increase of the frame rate. Thanks to HESM, it becomes easy to rapidly switch between color imaging and fast imaging, or to do both simultaneously in different regions of the image. One should use a color camera and an active multi-spectral illumination that can be simple LEDs, following instructions and code provided online [128].

We adapted the method of Chapter 3 to fluorescence microscopy in Chapter 4, dubbed fluo-HESM. We presented an increase of the imaging frame rate of a factor 2. Provided that one can

generate a sample with multiple co-localized fluorophores and temporally modulate excitation lasers at high speed, which can be trickier than just the LEDs in Chapter 3, fluo-HESM is also relatively simple to implement. It has the possibility to further speed-up well-established fast fluorescence microscopy techniques, while maintaining the ability to do color imaging within regions of interest.

In Chapter 5, we presented a method to perform temporal generalized sampling in optical microscopy. Our approach allows for the use of implementable pre-filters with finite support and verifying the positivity constraint. We presented an applied way to perform generalized temporal sampling in a B-spline basis, and our work can be extended to other bases as long as the positivity constraint (measured light intensity can only be positive) is respected and pre-filters are of finite support.

Finally, in Chapter 6 we proposed a method to perform spectral imaging of repeating processes. The method relies on a simple data acquisition procedure followed by temporal registration and solving of an inverse problem. We characterized the method on static samples and showed a median error of around 10% by comparing reconstructions from our method with measurements from a spectrometer, and validated the method comparing static reconstructions with dynamic ones of the same sample. We applied this method to the beating heart of a zebrafish larva to demonstrate the potential applicability for studying cardiac dynamics and differentiating tissues and cells. The method could easily be extended to fluorescence microscopy to perform linear unmixing fluorescence in presence of a potentially high number of fluorophore species.

## 7.2 Further research outputs

The multi-disciplinary nature of my thesis topic required me to set up the infrastructure to demonstrate the feasibility of the theoretical ideas in practice.

### **Set up of a light-sheet microscopy platform**

A key component to carry out my experiments was the ability to have a fully customizable instrument available. An important part of my time was therefore devoted to building a light-sheet microscope, based on the OpenSPIM project [33]. We were fortunate to the mechanical shop at the “Base aérienne de Sion” (Switzerland), who kindly manufactured custom parts, necessary to building the microscope.

My original setup is now further being developed by other lab members towards the goal of obtaining a more versatile instrument. Our choice of using an open microscope design, allowed me to make the specifications of the software and hardware necessary to replicate my experiments directly available to this community [128].

### 7.3 Proposed Future work

In this thesis, we pushed the capabilities of microscopes by increasing temporal or spectral resolution, by increasing their operating flexibility, and by mitigating temporal aliasing in image sequences. These contributions could have direct implications for other application and benefit from further extensions. We list some possible future work below.

#### **Calibration-free hue-encoded shutter method**

The methods of Chapters 3 and 4 both require calibration on a static part of the sample. This can probably be avoided by making assumptions, typically that the imaged scene should on average be slowly moving. Finding any suitable criterion that depends on the sample, typically that its temporal Total Variation should be as low as possible, Equation 3.12 can be solved using a variational approach and solving for the parameters in  $\mathbf{d}_0$  and  $\mathbf{\Gamma}$  as well as finding the best solution  $\mathbf{x}$ .

#### **Machine learning for the inverse problem solving**

In Chapters 3 and 4, a forward model is built, assuming linearity which is likely incorrect. A deep learning model could be trained to learn the non-linear relation between the color camera, a set of active illuminations, and a dynamic sample. This would also take care of the calibration.

In preliminary works, I adapted a widely-used image segmentation convolutional neural network, called U-Net [165], for regression as shown on Figure 7.1. I could train this network to perform the least-squares inversion of Eq. (3.12) by simulating acquired data using calibration parameters from Chapter 3. I trained the network using three different calibrations and the test-reconstructions obtained, simulating acquisition with any of the three models show promising results.

I further believe that a similar network can be adapted and trained to output, from a series of RGB images, another series of RGB images with a three-fold increase of the frame-rate. This would be a major step forward as it would acquire color images with an active multi-spectral illumination and reconstruct 3-times the number of acquisitions, without losing the color information.

#### **Compressed sensing of the heart with random codes and sorting**

In Chapters 4 and 6, we sequentially acquire various beats of a heart and treat each acquisition as parallel observations of the same process. This has been used to perform simultaneous denoising and temporal super-resolution of the beating heart [73], to build volume videos (3D+time) of the beating heart [145] or to superpose images from multiple acquisition modalities [147].

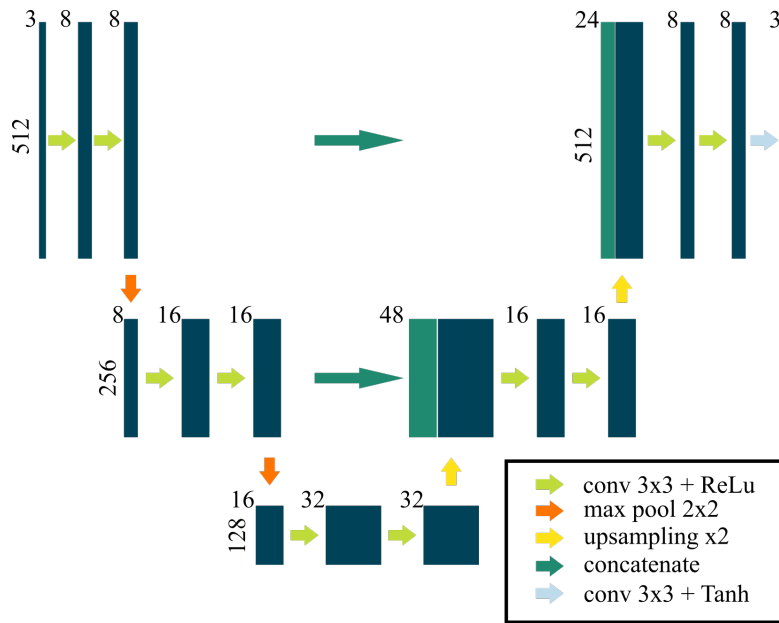


Figure 7.1 – U-Net adapted for regression. An input RGB image of size  $512 \times 512 \times 3$  is processed and the output has the same shape. The color information has been transformed by the network in temporal information. To adapt the U-Net for regression, the last layers have been changed to be convolution + non-linearity layers, followed by a hyperbolic tangent layer. This network has 30K parameters.

Another application of this idea would be to perform compressed sensing of the beating heart through imaging with a known pseudo-random pulsed code. Performing sorting post-acquisitions [166], one can do compressed sensing reconstruction and possibly reconstruct a very high temporal resolution video of the beating heart.

Taking advantage of the simultaneous computation of multiple inner products of Section 5.4.1, it could also be possible to do temporal compressive sensing if one would be to devise an optical acquisition system with many color channels.

### Hue-encoded shutter method for 2-photons imaging

2-Photons imaging is an imaging modality that is well-suited for imaging live samples in vivo, thanks to its low photo-damaging of the sample, fast, and deep tissue imaging capabilities [87]. It would likely be possible to apply our method of Chapter 4 to 2-photons imaging. This modality would particularly benefit from our approach as it offer alternative illumination-excitation sequences and use of fluorophores [88] which could be taken advantage of or benefit from HESM.

### Fully aliasing-free temporal imaging

As mentioned in Section 5.6, of our generalized sampling method of Chapter 5, during the image transfer from the camera to the computer, the partition of unity condition [106] is not



respected. This issue can be solved using two cameras whose exposure times are staggered in time, or using rolling-shutter special mode where lines on the photosensitive sensor of the camera are sequentially capturing light and transferring their pixels to the computer.

This could prove useful for motion analysis of the beating heart [167, 168, 169].

### **Spectral imaging of repeating processes using more filters**

In our method of Chapter 6, we used 6 filters in our experiments and presented results with the visible spectrum divided in bands of  $60nm$ . It would be interesting in using more filters, and applying the method for a quantitative study.

For instance, measuring the percentage of oxygenated haemoglobin within the heart of zebrafish embryos. Also, I would find it interesting to see the method applied in fluorescence microscopy for spectral imaging in the presence of many fluorophores.

## **7.4 Final words**

To conclude this dissertation, we state again the main contributions of the thesis.

First, we presented a temporal super-resolution method, which we applied to both transmission microscopy [117] as well as fluorescence light-sheet microscopy [131]. The sectioning ability of light-sheet microscopy allowed us to apply our temporal super-resolution method and reconstruct a whole volume of the beating heart of a zebrafish embryo.

Second, we introduced a way to strongly mitigate temporal aliasing in imaging by performing temporal generalized sampling [149, 150]. This method introduces a new way to simultaneously compute multiple overlapping inner products of the sampled signal with chosen pre-filters. This can be taken advantage of for other purposes than generalized sampling.

Third, we presented a method to perform spectral imaging of repeating processes [148]. We illustrated its potential by performing spectral imaging of the beating heart of the zebrafish embryo.

Finally, all our methods rely on the use of active illumination and computational procedures and they are particularly well suited for microscopy as they are simple to implement on existing microscopes with cost-effective hardware. For all of our publications, we presented real data of live samples, which we acquired on our imaging platform.



# A Derivation of the Alternating Direction Method of Multipliers for temporal super-resolution

## A.1 Introduction

For our paper [117] of Chapter 3, we minimize an  $\ell_2$ -norm to solve an inverse problem to do temporal super-resolution. The minimized energy  $e(\mathbf{A}, \mathbf{x}, \mathbf{y})$  is the  $\ell_2$ -norm of the error between the observations vector  $\mathbf{y}$  and the solution  $\mathbf{x}$  linearly transformed by a forward model  $\mathbf{A}$ , that is

$$e(\mathbf{A}, \mathbf{x}, \mathbf{y}) = \|\mathbf{Ax} - \mathbf{y}\|_2^2. \quad (\text{A.1})$$

The above super-resolution inversion works as long as the matrix  $\mathbf{A}$  is well conditioned. In practice, two things make our reconstructions “flicker” (i.e. a static part of the imaged scene flickers along time, which is an error); (1) our linear model is wrong and (2) the parameters in our model are slightly off.

In our paper [131] of Chapter 4, to increase the robustness of our inversion method, we add a temporal *total variation* regularization term, that is the  $\ell_1$  norm of the first order derivative of the reconstructions. To implement this regularization and solve a regularized inverse problem, we are interested in the *alternating direction method of multipliers* (ADMM), a variant of the *augmented Lagrangian methods* [170, 171].

## A.2 Alternating direction method of multipliers

ADMM allows to solve *constrained optimization problems*; they typically have the form [139, 135]:

$$\begin{aligned} &\text{minimize} && f(\mathbf{x}) + g(\mathbf{z}) \\ &\text{such that} && \mathbf{Ax} + \mathbf{Bz} = \mathbf{c}. \end{aligned} \quad (\text{A.2})$$

## Appendix A. Derivation of the Alternating Direction Method of Multipliers for temporal super-resolution

---

with  $\mathbf{x} \in \mathbb{R}^m$ ,  $\mathbf{z} \in \mathbb{R}^n$ ,  $\mathbf{A} \in \mathbb{R}^{p \times m}$ ,  $\mathbf{B} \in \mathbb{R}^{p \times n}$  and  $\mathbf{c} \in \mathbb{R}^p$ . We start by forming the *augmented Lagrangian* associated with Problem (A.2):

$$\mathcal{L}(\mathbf{x}, \mathbf{z}, \mathbf{y}) = \underbrace{f(\mathbf{x}) + g(\mathbf{z}) + \mathbf{y}^\top (\mathbf{A}\mathbf{x} + \mathbf{B}\mathbf{z} - \mathbf{c})}_{\text{Lagrangian}} + (\rho/2) \|\mathbf{A}\mathbf{x} + \mathbf{B}\mathbf{z} - \mathbf{c}\|_2^2,$$

where  $\mathbf{y} \in \mathbb{R}^p$  is called a *dual* variable. Notice the extra quadratic term, explaining the term *augmented Lagrangian* [135].

As for the penalty method, we do the optimization on the augmented Lagrangian instead of the constrained problem. The optimization iterations are:

```

while not converged do
  |  $\mathbf{x}^{k+1} = \arg \min_{\mathbf{x}} \mathcal{L}(\mathbf{x}, \mathbf{z}^k, \mathbf{y}^k);$ 
  |  $\mathbf{z}^{k+1} = \arg \min_{\mathbf{z}} \mathcal{L}(\mathbf{x}^k, \mathbf{z}, \mathbf{y}^k);$ 
  |  $\mathbf{y}^{k+1} = \mathbf{y}^k + \rho(\mathbf{A}\mathbf{x}^{k+1} + \mathbf{B}\mathbf{z}^{k+1} - \mathbf{c});$ 
end

```

**Algorithm 2:** ADMM algorithm generic steps: (1) primal variables ( $\mathbf{x}$  and  $\mathbf{z}$ ) update, (2) dual variables update, also called dual ascent.

where  $\rho \in \mathbb{R}_+$  is a penalty parameter.

### A.3 ADMM applied to the temporal super-resolution problem of Chapter 4

#### A.3.1 LASSO-formulation of the problem

The model in [117] is an over-simplification of the underlying physical process, but we know it is a rather natural thing that the reconstructed signal  $\mathbf{x}^*$  be piecewise constant. We enforce this by adding a regularization on the  $\ell_1$ -norm of the first derivative of  $\mathbf{x}$ . We now seek the solution to the unconstrained problem

$$\text{minimize } \frac{1}{2} \|\mathbf{A}\mathbf{x} - \mathbf{y}\|_2^2 + \lambda \|\mathbf{T}\mathbf{x}\|_1, \quad (\text{A.3})$$

where  $\mathbf{T}$  is a first-order Tikhonov matrix (also known as the *Total Variation* regularization). Problem (A.3) is commonly referred to as LASSO. We then *split* Problem (A.3) to a constrained problem [172]:

$$\begin{aligned} & \text{minimize } \frac{1}{2} \|\mathbf{A}\mathbf{x} - \mathbf{y}\|_2^2 + \lambda \|\mathbf{u}\|_1, \\ & \text{such that } \mathbf{T}\mathbf{x} = \mathbf{u}, \end{aligned} \quad (\text{A.4})$$

### A.3. ADMM applied to the temporal super-resolution problem of Chapter 4

and build the *augmented Lagrangian* for Problem (A.4) (notice the introduction of a new variable, which is a common trick with ADMM [173, 135, 172]):

$$\mathcal{L}(\mathbf{x}, \mathbf{u}, \mathbf{z}) = \frac{1}{2} \|\mathbf{Ax} - \mathbf{y}\|_2^2 + \lambda \|\mathbf{u}\|_1 + \mathbf{z}^\top (\mathbf{T}\mathbf{x} - \mathbf{u}) + (\rho/2) \|\mathbf{T}\mathbf{x} - \mathbf{u}\|_2^2. \quad (\text{A.5})$$

The ADMM algorithm requires computing the gradient of  $\mathcal{L}(\mathbf{x}, \mathbf{u}, \mathbf{z})$ :

$$\frac{\partial}{\partial \mathbf{z}} \mathcal{L}(\mathbf{x}, \mathbf{u}, \mathbf{z}) = \mathbf{T}\mathbf{x} - \mathbf{u} \quad (\text{A.6})$$

$$\frac{\partial}{\partial \mathbf{x}} \mathcal{L}(\mathbf{x}, \mathbf{u}, \mathbf{z}) = \mathbf{A}^\top (\mathbf{Ax} - \mathbf{y}) + \rho \mathbf{T}^\top (\mathbf{T}\mathbf{x} - \mathbf{u}) + \mathbf{z}^\top \mathbf{T} \quad (\text{A.7})$$

$$\frac{\partial}{\partial \mathbf{u}} \mathcal{L}(\mathbf{x}, \mathbf{u}, \mathbf{z}) = \frac{\partial}{\partial \mathbf{u}} \{\lambda \|\mathbf{u}\|_1\} + \rho(\mathbf{u} - \mathbf{T}\mathbf{x}) - \mathbf{z}^\top. \quad (\text{A.8})$$

We now compute the values to have  $\nabla \mathcal{L}(\mathbf{x}, \mathbf{u}, \mathbf{z}) = 0$  for the primal variables. Here is the update for  $\mathbf{x}$ :

$$0 = \mathbf{A}^\top (\mathbf{Ax}^* - \mathbf{y}) + \rho \mathbf{T}^\top (\mathbf{T}\mathbf{x}^* - \mathbf{u}) + \mathbf{z}^\top \mathbf{T} \quad (\text{A.9})$$

$$\mathbf{x}^* = (\mathbf{A}^\top \mathbf{A} + \rho \mathbf{T}^\top \mathbf{T})^{-1} (\mathbf{A}^\top \mathbf{y} + \mathbf{T}^\top (\rho \mathbf{u} - \mathbf{z})). \quad (\text{A.10})$$

For  $\mathbf{u}$ , it is a tad harder because of the  $\ell_1$ -norm, which is not differentiable at 0. It is, however, still convex and the properties of sub-gradients hold (see Section 23 in [174], p. 213, or [170, 171]). The component-wise derivative of the  $\ell_1$ -norm is defined as:

$$\frac{\partial}{\partial \mathbf{u}} \{\|\mathbf{u}\|_1\}_i = \begin{cases} \text{sign}(u_i) & u_i \neq 0 \\ [-1, 1] & u_i = 0. \end{cases} \quad (\text{A.11})$$

Taking the first case into account ( $u_i \neq 0$ ), we can compute  $\frac{\partial}{\partial \mathbf{u}} \mathcal{L}(\mathbf{x}, \mathbf{u}, \mathbf{z}) = 0$ :

$$\lambda(\text{sign}(u_i)) + [\rho(\mathbf{u} - \mathbf{T}\mathbf{x}) - \mathbf{z}]_i = 0 \quad (\text{A.12})$$

$$= \begin{cases} [\lambda + \rho(\mathbf{u} - \mathbf{T}\mathbf{x}) - \mathbf{z}]_i & \text{if } u_i > 0 \\ [\lambda - \rho(\mathbf{u} - \mathbf{T}\mathbf{x}) - \mathbf{z}]_i & \text{if } u_i < 0 \end{cases} \quad (\text{A.13})$$

$$\rightarrow u_i = \begin{cases} \frac{z_i - \lambda}{\rho} + [\mathbf{T}\mathbf{x}]_i & \text{if } u_i > 0 \\ \frac{z_i + \lambda}{\rho} + [\mathbf{T}\mathbf{x}]_i & \text{if } u_i < 0. \end{cases} \quad (\text{A.14})$$

$$= \begin{cases} s_i - \lambda/\rho & \text{if } u_i > 0 \\ s_i + \lambda/\rho & \text{if } u_i < 0 \end{cases} \quad (\text{A.15})$$

## Appendix A. Derivation of the Alternating Direction Method of Multipliers for temporal super-resolution

---

where  $s_i = [\mathbf{T}\mathbf{x}]_i + \frac{z_i}{\rho}$ . Instead of expressing the  $u_i$  as a function of itself, we can express it in terms of  $s_i, \lambda$  and  $\rho$ . Also, looking at the second case in Equation (A.11) ( $u_i = 0$ ), we have that

$$0 \in \lambda[-1, 1] + [\rho(\mathbf{u} - \mathbf{T}\mathbf{x}) - \mathbf{z}]_i \quad (\text{A.16})$$

$$0 \in [s_i - \lambda/\rho, s_i + \lambda/\rho] \quad (\text{A.17})$$

$$\Rightarrow |s_i| < \lambda/\rho \quad \text{if } u_i = 0. \quad (\text{A.18})$$

We can now write  $u_i$  according to a condition on  $s_i$ :

$$u_i = \begin{cases} s_i - \lambda/\rho & \text{if } s_i > \lambda/\rho \\ s_i + \lambda/\rho & \text{if } s_i < -\lambda/\rho \\ 0 & \text{if } |s_i| < \lambda/\rho \end{cases} \quad (\text{A.19})$$

Equation (A.19) is a component-wise *soft threshold* noted as  $S_{\lambda/\rho}(\mathbf{s})$  [135]. Solving for  $\nabla \mathcal{L}(x, u, y) = 0$ , Algorithm 2 becomes

**while not converged do**

$$\mathbf{x}^{k+1} = (\mathbf{A}^\top \mathbf{A} + \rho \mathbf{T}^\top \mathbf{T})^{-1} (\mathbf{A}^\top \mathbf{y} + \mathbf{T}^\top (\rho \mathbf{u}^k - \mathbf{z}^k));$$

$$\mathbf{u}^{k+1} = S_{\lambda/\rho}(\mathbf{T}\mathbf{x}^{k+1} + \mathbf{z}^k);$$

$$\mathbf{z}^{k+1} = \mathbf{z}^k + \mathbf{T}\mathbf{x}^{k+1} - \mathbf{u}^{k+1};$$

**end**

**Algorithm 3:** ADMM applied to temporal super-resolution in [117]

## B Constrained $\ell_1$ -norm minimization with linear programming

In [148], we minimize the following  $\ell_1$  norm, with constraints on the solutions:

$$\begin{aligned} & \text{minimize} && \| \mathbf{y} - \mathbf{d} - \mathbf{A}\mathbf{s} \|_{\ell_1} , \\ & \text{subject to} && 0 \leq \mathbf{s} \leq 1 \end{aligned} \quad (\text{B.1})$$

with  $\mathbf{y}, \mathbf{d} \in \mathbb{R}^{m \times 1}$ ,  $\mathbf{A} \in \mathbb{R}^{m \times n}$  and  $\mathbf{s} \in \mathbb{R}^{n \times 1}$ . We explain in the paper that we solve this using the simplex, a linear programming (LP) technique [127, 164].

However, LP packages as CPLEX [127] or CVXPY [175, 176] solve problems of the form:

$$\begin{aligned} & \text{minimize} && \mathbf{c}^\top \mathbf{x} \\ & \text{subject to} && \begin{cases} \mathbf{A}\mathbf{x} = \mathbf{b} \\ \mathbf{x} \geq 0 \end{cases} \end{aligned} \quad (\text{B.2})$$

with  $\mathbf{c}, \mathbf{x} \in \mathbb{R}^{n \times 1}$ . Similarly to [73], we re-formulate the problem in Equation (B.1) to match the LP form, by adding a variable and introducing an equivalent problem.

$$\begin{aligned} & \text{minimize} && \mathbf{c}^\top \mathbf{z} \\ & \text{subject to} && -\mathbf{z} \leq \mathbf{A}\mathbf{s} - \mathbf{y} - \mathbf{d} \leq \mathbf{z} , \\ & && \text{and} \quad \mathbf{z} \geq 0 \end{aligned} \quad (\text{B.3})$$

where  $\mathbf{z} \in \mathbb{R}^{m \times 1}$  is a helper variable bounding the absolute values of  $\mathbf{A}\mathbf{s} - \mathbf{y} - \mathbf{d}$ . We separate the two inequalities and rewrite Eq. (B.3) as

$$\begin{aligned} & \text{minimize} && \mathbf{c}^\top \mathbf{z} \\ & \text{subject to} && \mathbf{A}\mathbf{s} - \mathbf{y} + \mathbf{d} \leq \mathbf{z} \Rightarrow \mathbf{A}\mathbf{s} - \mathbf{z} \leq \mathbf{y} - \mathbf{d} \\ & && \text{and} \quad -(\mathbf{A}\mathbf{s} - \mathbf{y} - \mathbf{d}) \leq -\mathbf{z} \Rightarrow -\mathbf{A}\mathbf{s} - \mathbf{z} \leq -(\mathbf{y} - \mathbf{d}) , \\ & && \text{and} \quad \mathbf{z} \geq 0 \end{aligned} \quad (\text{B.4})$$

## Appendix B. Constrained $\ell_1$ -norm minimization with linear programming

---

which we can rewrite in matrix form:

$$\begin{aligned}
 & \text{minimize} && \underbrace{\begin{pmatrix} \mathbf{0}_{n \times 1} \\ \mathbf{1}_{m \times 1} \end{pmatrix}}_{\tilde{\mathbf{c}}}^\top \begin{pmatrix} \mathbf{s} \\ \mathbf{z} \end{pmatrix} \\
 & \text{subject to} && \underbrace{\begin{pmatrix} \mathbf{A} & -\mathbf{I}_{m \times m} \\ -\mathbf{A} & -\mathbf{I}_{m \times m} \\ \mathbf{0}_{n \times n} & -\mathbf{I}_{m \times m} \end{pmatrix}}_{\tilde{\mathbf{A}}} \underbrace{\begin{pmatrix} \mathbf{s} \\ \mathbf{z} \end{pmatrix}}_{\tilde{\mathbf{x}}} \leq \underbrace{\begin{pmatrix} \mathbf{y} - \mathbf{d} \\ -(\mathbf{y} - \mathbf{d}) \\ \mathbf{0}_{m \times 1} \end{pmatrix}}_{\tilde{\mathbf{b}}}. \tag{B.5}
 \end{aligned}$$

We now see the familiar looking problem of Equation (B.2), where the vectors and matrices to feed an LP package are underlined. Most LP packages accept input as given in Equation (B.5) and offer the possibility to set lower and upper bounds on the solution. From the solution return by the LP package, the vector  $\mathbf{s}$  minimizing Eq. (6.7) is obtained by keeping the first  $n$  values of the returned solution  $\tilde{\mathbf{x}}$ .



# Bibliography

- [1] D. Evanko, A. Heinrichs, C. Karlsson Rosenthal, N. Gray, N. Rusk, N. Blow, K. Baumann, C. van Ooij, A. Schuldt, E. J. Chenette, A. Doerr, S. Grisendi, S. Tonzani, K. Whalley, N. Le Bot, R. David, S. Swaminathan, K. H. Wrighton, F. Cesari, and N. De Souza, “Milestones in light microscopy.” [https://www.nature.com/milestones/milelight/pdf/milelight\\_all.pdf](https://www.nature.com/milestones/milelight/pdf/milelight_all.pdf), 2008. Accessed: 2020-02-12.
- [2] G. B. Airy, “On the diffraction of an object-glass with circular aperture,” *Transaction of the Cambridge Philosophical Society*, vol. 5, pp. 283–291, 1835.
- [3] E. Abbe, “Beiträge zur theorie des mikroskops und der mikroskopischen wahrnehmung,” *Archiv für Mikroskopische Anatomie*, vol. 9, pp. 413–418, 1873.
- [4] Lord F. R. S. Rayleigh, “XXXI. investigations in optics, with special reference to the spectroscope,” *The London, Edinburgh, and Dublin Philosophical Magazine and Journal of Science*, vol. 8, no. 49, pp. 261–274, 1879.
- [5] A. Koehler, “Ein neues Beleuchtungsverfahren für mikrographische Zwecke,” *Zeitschrift für wissenschaftliche Mikroskopie und für Mikroskopische Technik*, vol. 10, no. 4, pp. 433–440, 1893.
- [6] A. H. Coons, H. J. Creech, and R. N. Jones, “Immunological properties of an antibody containing a fluorescent group,” *Proceedings of the Society for Experimental Biology and Medicine*, vol. 47, no. 2, pp. 200–202, 1941.
- [7] A. H. Coons, H. J. Creech, R. N. Jones, and E. Berliner, “The demonstration of pneumococcal antigen in tissues by the use of fluorescent antibody,” *The Journal of Immunology*, vol. 45, no. 3, pp. 159–170, 1942.
- [8] M. Minsky, “Microscopy apparatus,” U.S. Patent US3013467A, 1957.
- [9] M. D. Egger and M. Petran, “New reflected-light microscope for viewing unstained brain and ganglion cells,” *Science*, vol. 157, no. 3786, pp. 305–307, 1967.

## Bibliography

---

- [10] C. J. R. Sheppard and T. Wilson, "The theory of the direct-view confocal microscope," *Journal of Microscopy*, vol. 124, no. 2, pp. 107–117, 1981.
- [11] J. G. White, W. B. Amos, and M. Fordham, "An evaluation of confocal versus conventional imaging of biological structures by fluorescence light microscopy.," *Journal of Cell Biology*, vol. 105, pp. 41–48, 07 1987.
- [12] G. van Meer, E. H. Stelzer, R. W. Wijnaendts-van Resandt, and K. Simons, "Sorting of sphingolipids in epithelial (Madin-Darby canine kidney) cells.," *Journal of Cell Biology*, vol. 105, pp. 1623–1635, 10 1987.
- [13] A. H. Voie, D. H. Burns, and F. A. Spelman, "Orthogonal-plane fluorescence optical sectioning: three-dimensional imaging of macroscopic biological specimens.," *Journal of Microscopy*, vol. 170, pp. 229–236, 1993.
- [14] A. H. Voie and F. A. Spelman, "Three-dimensional reconstruction of the cochlea from two-dimensional images of optical sections," *Computerized Medical Imaging and Graphics*, vol. 19, no. 5, pp. 377–384, 1995.
- [15] A. H. Voie, "Imaging the intact guinea pig tympanic bulla by orthogonal-plane fluorescence optical sectioning microscopy," *Hearing Research*, vol. 171, no. 1, pp. 119–128, 2002.
- [16] S. Lindek, R. Pick, and E. H. K. Stelzer, "Confocal theta microscope with three objective lenses," *Review of Scientific Instruments*, vol. 65, no. 11, pp. 3367–3372, 1994.
- [17] S. Lindek and E. H. K. Stelzer, "Confocal theta microscopy and 4Pi-confocal theta microscopy," in *Three-Dimensional Microscopy: Image Acquisition and Processing* (C. J. Cogswell and K. Carlsson, eds.), vol. 2184, pp. 188–194, International Society for Optics and Photonics, SPIE, 1994.
- [18] E. H. K. Stelzer, S. Lindek, S. Albrecht, R. Pick, G. Ritter, N. J. Salmon, and R. Stricker, "A new tool for the observation of embryos and other large specimens: confocal theta fluorescence microscopy," *Journal of Microscopy*, vol. 179, no. 1, pp. 1–10, 1995.
- [19] H. Siedentopf and R. Zsigmondy, "Über sichtbarmachung und grössenbestimmung ultramikroskopischer teilchen, mit besonderer anwendung auf goldrubingläser," *Annalen der Physik*, vol. 315, no. 1, pp. 1–39, 1902.
- [20] P. A. Santi, "Light sheet fluorescence microscopy: a review.," *J Histochem Cytochem*, vol. 59, pp. 129–138, Feb 2011.
- [21] J. Huisken, J. Swoger, F. Del Bene, J. Wittbrodt, and E. H. K. Stelzer, "Optical sectioning deep inside live embryos by selective plane illumination microscopy," *Science*, vol. 305, no. 5686, pp. 1007–1009, 2004.

- [22] J. Huisken and D. Y. R. Stainier, “Even fluorescence excitation by multidirectional selective plane illumination microscopy (mspim),” *Opt. Lett.*, vol. 32, pp. 2608–2610, Sep 2007.
- [23] J. Huisken and D. Y. R. Stainier, “Selective plane illumination microscopy techniques in developmental biology,” *Development*, vol. 136, no. 12, pp. 1963–1975, 2009.
- [24] E. Fuchs, J. S. Jaffe, R. A. Long, and F. Azam, “Thin laser light sheet microscope for microbial oceanography,” *Opt. Express*, vol. 10, pp. 145–154, Jan 2002.
- [25] J. A. N. Buytaert and J. J. Dirckx, “Design and quantitative resolution measurements of an optical virtual sectioning three-dimensional imaging technique for biomedical specimens, featuring two-micrometer slicing resolution,” *Journal of Biomedical Optics*, vol. 12, no. 1, pp. 1–13, 2007.
- [26] H.-U. Dodt, U. Leischner, A. Schierloh, N. Jährling, C. P. Mauch, K. Deininger, J. M. Deussing, M. Eder, W. Zieglgänsberger, and K. Becker, “Ultramicroscopy: three-dimensional visualization of neuronal networks in the whole mouse brain,” *Nature Methods*, vol. 4, no. 4, pp. 331–336, 2007.
- [27] C. Dunsby, “Optically sectioned imaging by oblique plane microscopy,” *Opt. Express*, vol. 16, pp. 20306–20316, Dec 2008.
- [28] P. A. Santi, S. B. Johnson, M. Hillenbrand, P. Z. GrandPre, T. J. Glass, and J. Leger, “Thin-sheet laser imaging microscopy for optical sectioning of thick tissues,” *Biotechniques*, vol. 46, pp. 287–294, 2009.
- [29] P. J. Keller, A. D. Schmidt, A. Santella, K. Khairy, Z. Bao, J. Wittbrodt, and E. H. K. Stelzer, “Fast, high-contrast imaging of animal development with scanned light sheet-based structured-illumination microscopy,” *Nature Methods*, vol. 7, pp. 637–642, 2010.
- [30] P. J. Keller, A. D. Schmidt, J. Wittbrodt, and E. H. K. Stelzer, “Reconstruction of zebrafish early embryonic development by scanned light sheet microscopy,” *Science*, vol. 322, no. 5904, pp. 1065–1069, 2008.
- [31] P. J. Keller and E. H. K. Stelzer, “Quantitative in vivo imaging of entire embryos with digital scanned laser light sheet fluorescence microscopy,” *Current Opinion in Neurobiology*, vol. 18, no. 6, pp. 624–632, 2008.
- [32] J. B. Bosse, N. S. Tanneti, I. B. Hogue, and L. W. Enquist, “Open led illuminator: A simple and inexpensive LED illuminator for fast multicolor particle tracking in neurons,” *PLOS ONE*, vol. 10, pp. 1–21, 11 2015.

## Bibliography

---

- [33] P. G. Pitrone, J. Schindelin, L. Stuyvenberg, S. Preibisch, M. Weber, K. W. Eliceiri, J. Huisken, and P. Tomancak, "OpenSPIM: an open-access light-sheet microscopy platform," *Nat. Methods*, vol. 10, pp. 598–599, Jun 2013.
- [34] E. J. Gualda, T. Vale, P. Almada, J. A. Feijó, G. G. Martins, and N. Moreno, "OpenSpin Microscopy: an open-source integrated microscopy platform," *Nat. Methods*, pp. 599–600, Jun 2013.
- [35] A. Edelstein, N. Amodaj, K. Hoover, R. Vale, and N. Stuurman, "Computer control of microscopes using  $\mu$ Manager," *Curr Protoc Mol Biol*, vol. Chapter 14, pp. Unit14.20–Unit14.20, 10 2010.
- [36] A. Edelstein, M. Tsuchida, N. Amodaj, H. Pinkard, R. Vale, and N. Stuurman, "Advanced methods of microscope control using  $\mu$ Manager software," *Journal of Biological Methods*, vol. 1, no. 2, 2014.
- [37] J. Krieger, "Spim principle image." [https://commons.wikimedia.org/wiki/File:Spim\\_prinziple\\_en.svg](https://commons.wikimedia.org/wiki/File:Spim_prinziple_en.svg). Creative Commons License.
- [38] S. W. Hell and E. H. K. Stelzer, "Fundamental improvement of resolution with a 4pi-confocal fluorescence microscope using two-photon excitation," *Optics Communications*, vol. 93, no. 5, pp. 277–282, 1992.
- [39] S. W. Hell and J. Wichmann, "Breaking the diffraction resolution limit by stimulated emission: stimulated-emission-depletion fluorescence microscopy," *Opt. Lett.*, vol. 19, pp. 780–782, Jun 1994.
- [40] T. A. Klar and S. W. Hell, "Subdiffraction resolution in far-field fluorescence microscopy," *Opt. Lett.*, vol. 24, pp. 954–956, Jul 1999.
- [41] T. A. Klar, S. Jakobs, M. Dyba, A. Egner, and S. W. Hell, "Fluorescence microscopy with diffraction resolution barrier broken by stimulated emission," *Proceedings of the National Academy of Sciences*, vol. 97, no. 15, pp. 8206–8210, 2000.
- [42] E. Betzig, G. H. Patterson, R. Sougrat, O. W. Lindwasser, S. Olenych, J. S. Bonifacino, M. W. Davidson, J. Lippincott-Schwartz, and H. F. Hess, "Imaging Intracellular Fluorescent Proteins at Nanometer Resolution," *Science*, vol. 313, no. 5793, pp. 1642–1645, 2006.
- [43] M. J. Rust, M. Bates, and X. Zhuang, "Sub-diffraction-limit imaging by stochastic optical reconstruction microscopy (STORM)," *Nat. Meth.*, vol. 3, pp. 793–796, oct 2006.
- [44] S. T. Hess, T. P. K. Girirajan, and M. D. Mason, "Ultra-high resolution imaging by fluorescence photoactivation localization microscopy," *Biophysical Journal*, vol. 91, no. 11, pp. 4258–4272, 2006.

- [45] J. I. Hoffman and S. Kaplan, "The incidence of congenital heart disease," *Journal of the American College of Cardiology*, vol. 39, no. 12, pp. 1890–1900, 2002.
- [46] M. E. Oster, K. A. Lee, M. A. Honein, T. Riehle-Colarusso, M. Shin, and A. Correa, "Temporal trends in survival among infants with critical congenital heart defects," *Pediatrics*, vol. 131, no. 5, pp. e1502–e1508, 2013.
- [47] C. T. Nguyen, Q. Lu, Y. Wang, and J.-N. Chen, "Zebrafish as a model for cardiovascular development and disease," *Drug discovery today. Disease models*, vol. 5, pp. 135–140, Fall 2008.
- [48] W. Spalteholz, *Über das Durchsichtigmachen von menschlichen und tierischen Präparaten und seine theoretischen Bedingungen, nebst Anhang: Über Knochenfärbung*. Leipzig: S. Hirzel, 1914.
- [49] W. Korytowski and T. Sarna, "Bleaching of melanin pigments. role of copper ions and hydrogen peroxide in autooxidation and photooxidation of synthetic dopa- melanin.," *Journal of Biological Chemistry*, vol. 265, no. 21, pp. 12410–12416, 1990.
- [50] M. W. Klymkowsky and J. Hanken, "Chapter 22 whole-mount staining of xenopus and other vertebrates," in *Xenopus laevis: Practical Uses in Cell and Molecular Biology* (B. K. Kay and H. B. Peng, eds.), vol. 36 of *Methods in Cell Biology*, pp. 419 – 441, Academic Press, 1991.
- [51] J. Karlsson, J. Von Hofsten, and P-E. Olsson, "Generating transparent zebrafish: A refined method to improve detection of gene expression during embryonic development," *Mar Biotechnol*, vol. 3, no. 6, pp. 522–527, 2001.
- [52] K. D. Poss, L. G. Wilson, and M. T. Keating, "Heart regeneration in zebrafish," *Science*, vol. 298, no. 5601, pp. 2188–2190, 2002.
- [53] J. M. González-Rosa, C. E. Burns, and C. G. Burns, "Zebrafish heart regeneration: 15 years of discoveries," *Regeneration (Oxford, England)*, vol. 4, pp. 105–123, 09 2017.
- [54] E. Endel, "Stages of zebrafish development." [https://en.wikipedia.org/wiki/Zebrafish#/media/File:Zebrafish\\_Developmental\\_Stages.tiff](https://en.wikipedia.org/wiki/Zebrafish#/media/File:Zebrafish_Developmental_Stages.tiff). Creative Commons License.
- [55] J. Vermot, S. E. Fraser, and M. Liebling, "Fast fluorescence microscopy for imaging the dynamics of embryonic development.," *HFSP journal*, vol. 2, no. 3, pp. 143–55, 2008.
- [56] E. Shechtman, Y. Caspi, and M. Irani, "Space-time super-resolution," *IEEE Trans. Pattern Anal. Mach. Intell.*, vol. 27, no. 4, pp. 531–545, 2005.
- [57] T. Li, X. He, Q. Teng, Z. Wang, and C. Ren, "Space-time super-resolution with patch group cuts prior," *Signal Process-Image*, vol. 30, pp. 147–165, 2015.

## Bibliography

---

- [58] A. Agrawal, M. Gupta, A. Veeraraghavan, and S. G. Narasimhan, “Optimal coded sampling for temporal super-resolution,” in *CVPR*, pp. 599–606, 2010.
- [59] R. Pournaghi and X. Wu, “Coded Acquisition of High Frame Rate Video,” *IEEE Trans. Image Process.*, vol. 23, no. Dec 2014, pp. 5670–5682, 2013.
- [60] E. J. Candès, J. Romberg, and T. Tao, “Robust uncertainty principles: exact signal reconstruction from highly incomplete frequency information,” *IEEE Transactions on Information Theory*, vol. 52, pp. 489–509, Feb 2006.
- [61] D. L. Donoho, “For most large underdetermined systems of equations, the minimal  $\ell_1$ -norm near-solution approximates the sparsest near-solution,” *Communications on Pure and Applied Mathematics*, vol. 59, no. 7, pp. 907–934, 2006.
- [62] E. J. Candès and T. Tao, “Near-optimal signal recovery from random projections: Universal encoding strategies?,” *IEEE Transactions on Information Theory*, vol. 52, pp. 5406–5425, Dec 2006.
- [63] D. L. Donoho, “Compressed sensing,” *IEEE Transactions on Information Theory*, vol. 52, pp. 1289–1306, April 2006.
- [64] E. J. Candès and M. B. Wakin, “An introduction to compressive sampling,” *IEEE Signal Processing Magazine*, vol. 25, no. 2, pp. 21–30, 2008.
- [65] M. Rudelson and R. Vershynin, “On sparse reconstruction from fourier and gaussian measurements,” *Communications on Pure and Applied Mathematics*, vol. 61, no. 8, pp. 1025–1045, 2008.
- [66] E. J. Candès, M. B. Wakin, and S. P. Boyd, “Enhancing sparsity by reweighted  $\ell_1$  minimization,” *Journal of Fourier Analysis and Applications*, vol. 14, no. 5, pp. 877–905, 2008.
- [67] M. F. Duarte and Y. C. Eldar, “Structured compressed sensing: From theory to applications,” *IEEE Transactions on Signal Processing*, vol. 59, pp. 4053–4085, Sep. 2011.
- [68] S. Gleichman and Y. C. Eldar, “Blind compressed sensing,” *IEEE Transactions on Information Theory*, vol. 57, pp. 6958–6975, Oct 2011.
- [69] P. Llull, X. Liao, X. Yuan, J. Yang, D. Kittle, L. Carin, G. Sapiro, and D. J. Brady, “Coded aperture compressive temporal imaging,” *Opt. Express*, vol. 21, no. 9, pp. 1289–1306, 2013.
- [70] X. Fei, Z. Wei, and L. Xiao, “Iterative directional total variation refinement for compressive sensing image reconstruction,” *IEEE Signal Processing Letters*, vol. 20, no. 11, pp. 1070–1073, 2013.

- 
- [71] T.-H. Tsai, P. Llull, X. Yuan, L. Carin, and D. J. Brady, "Spectral-temporal compressive imaging," *Opt. Lett.*, vol. 40, no. 17, pp. 4054–4057, 2015.
- [72] R. Koller, L. Schmid, N. Matsuda, T. Niederberger, L. Spinoulas, O. Cossairt, G. Schuster, and A. K. Katsaggelos, "High spatio-temporal resolution video with compressed sensing," *Opt. Express*, vol. 23, no. 12, p. 15992, 2015.
- [73] K. G. Chan, S. J. Streichan, L. A. Trinh, and M. Liebling, "Simultaneous temporal super-resolution and denoising for cardiac fluorescence microscopy," *IEEE Trans. Comput. Imaging*, vol. 2, no. 3, pp. 348–358, 2016.
- [74] A. Veeraraghavan, D. Reddy, and R. Raskar, "Coded strobing photography: Compressive sensing of high speed periodic videos," *IEEE Transactions on Pattern Analysis and Machine Intelligence*, vol. 33, pp. 671–686, April 2011.
- [75] G. Bub, M. Tecza, M. Helmes, P. Lee, and P. Kohl, "Temporal pixel multiplexing for simultaneous high-speed, high-resolution imaging.," *Nat. Methods*, vol. 7, no. 3, pp. 209–211, 2010.
- [76] N. Wagner, N. Norlin, J. Gierten, G. de Medeiros, B. Balázs, J. Wittbrodt, L. Hufnagel, and R. Prevedel, "Instantaneous isotropic volumetric imaging of fast biological processes," *Nat. Meth.*, vol. 16, no. 6, pp. 497–500, 2019.
- [77] W. Lukosz, "Optical systems with resolving powers exceeding the classical limit," *J. Opt. Soc. Am.*, vol. 56, pp. 1463–1471, Nov 1966.
- [78] W. Lukosz, "Optical systems with resolving powers exceeding the classical limit. II," *J. Opt. Soc. Am.*, vol. 57, pp. 932–941, Jul 1967.
- [79] P. J. Verveer, Q. S. Hanley, P. W. Verbeek, L. J. Van Vliet, and T. M. Jovin, "Theory of confocal fluorescence imaging in the programmable array microscope (pam)," *Journal of Microscopy*, vol. 189, no. 3, pp. 192–198, 1998.
- [80] M. G. L. Gustafsson, "Surpassing the lateral resolution limit by a factor of two using structured illumination microscopy," *J. Microsc.*, vol. 198, no. 2, pp. 82–87, 2000.
- [81] R. Heintzmann, T. M. Jovin, and C. Cremer, "Saturated patterned excitation microscopy—a concept for optical resolution improvement," *J. Opt. Soc. Am. A*, vol. 19, pp. 1599–1609, Aug 2002.
- [82] L. H. Schaefer, D. Schuster, and J. Schaffer, "Structured illumination microscopy: artefact analysis and reduction utilizing a parameter optimization approach," *Journal of Microscopy*, vol. 216, no. 2, pp. 165–174, 2004.

## Bibliography

---

- [83] E. Mudry, K. Belkebir, J. Girard, J. Savatier, E. Le Moal, C. Nicoletti, M. Allain, and A. Sentenac, "Structured illumination microscopy using unknown speckle patterns," *Nat. Photonics*, vol. 6, pp. 312–315, Apr 2012.
- [84] F. Orieux, E. Sepulveda, V. Lorient, B. Dubertret, and J. Olivo-Marin, "Bayesian estimation for optimized structured illumination microscopy," *IEEE Trans. Image Process.*, vol. 21, pp. 601–614, Feb 2012.
- [85] W. R. Zipfel, R. M. Williams, and W. W. Webb, "Nonlinear magic: multiphoton microscopy in the biosciences," *Nature Biotechnology*, vol. 21, no. 11, pp. 1369–1377, 2003.
- [86] W. R. Zipfel, R. M. Williams, R. Christie, A. Y. Nikitin, B. T. Hyman, and W. W. Webb, "Live tissue intrinsic emission microscopy using multiphoton-excited native fluorescence and second harmonic generation," *Proceedings of the National Academy of Sciences*, vol. 100, no. 12, pp. 7075–7080, 2003.
- [87] T. V. Truong, W. Supatto, D. S. Koos, J. M. Choi, and S. E. Fraser, "Deep and fast live imaging with two-photon scanned light-sheet microscopy," *Nature Methods*, vol. 8, no. 9, pp. 757–760, 2011.
- [88] P. Mahou, J. Vermot, E. Beaurepaire, and W. Supatto, "Multicolor two-photon light-sheet microscopy," *Nature Methods*, vol. 11, no. 6, pp. 600–601, 2014.
- [89] C. Stringari, L. Abdeladim, G. Malkinson, P. Mahou, X. Solinas, I. Lamarre, S. Brizion, J.-B. Galey, W. Supatto, R. Legouis, A.-M. Pena, and E. Beaurepaire, "Multicolor two-photon imaging of endogenous fluorophores in living tissues by wavelength mixing," *Scientific Reports*, vol. 7, no. 1, p. 3792, 2017.
- [90] R. W. G. Hunt and M. R. Pointer, *Measuring colour*. John Wiley & Sons, 4th edition ed., 2011.
- [91] Y. Garini, I. T. Young, and G. McNamara, "Spectral imaging: Principles and applications," *Cytometry Part A*, vol. 69A, no. 8, pp. 735–747, 2006.
- [92] R. M. Levenson and J. R. Mansfield, "Multispectral imaging in biology and medicine: Slices of life," *Cytometry Part A*, vol. 69A, no. 8, pp. 748–758, 2006.
- [93] L. Zhou and W. S. El-Deiry, "Multispectral fluorescence imaging," *Journal of Nuclear Medicine*, 2009.
- [94] T. Zimmermann, J. Rietdorf, A. Girod, V. Georget, and R. Pepperkok, "Spectral imaging and linear un-mixing enables improved FRET efficiency with a novel GFP2–YFP FRET pair," *FEBS Letters*, vol. 531, no. 2, pp. 245–249, 2002.



- [95] T. Zimmermann, J. Rietdorf, and R. Pepperkok, "Spectral imaging and its applications in live cell microscopy," *FEBS Letters*, vol. 546, no. 1, pp. 87–92, 2003.
- [96] M. B. Sinclair, D. M. Haaland, J. A. Timlin, and H. D. T. Jones, "Hyperspectral confocal microscope," *Appl. Opt.*, vol. 45, pp. 6283–6291, Aug 2006.
- [97] P. M. Carlton, J. Boulanger, C. Kervrann, J.-B. Sibarita, J. Salamero, S. Gordon-Messer, D. Bressan, J. E. Haber, S. Haase, L. Shao, L. Winoto, A. Matsuda, P. Kner, S. Uzawa, M. Gustafsson, Z. Kam, D. A. Agard, and J. W. Sedat, "Fast live simultaneous multiwavelength four-dimensional optical microscopy," *Proceedings of the National Academy of Sciences*, vol. 107, no. 37, pp. 16016–16022, 2010.
- [98] F. Fereidouni, A. N. Bader, and H. C. Gerritsen, "Spectral phasor analysis allows rapid and reliable unmixing of fluorescence microscopy spectral images," *Opt. Express*, vol. 20, pp. 12729–12741, Jun 2012.
- [99] W. Jahr, B. Schmid, C. Schmied, F. O. Fahrbach, and J. Huisken, "Hyperspectral light sheet microscopy," *Nature Communications*, vol. 6, no. 1, p. 7990, 2015.
- [100] T. Niehörster, A. Löschberger, I. Gregor, B. Krämer, H.-J. Rahn, M. Patting, F. Koberling, J. Enderlein, and M. Sauer, "Multi-target spectrally resolved fluorescence lifetime imaging microscopy," *Nature Methods*, vol. 13, no. 3, pp. 257–262, 2016.
- [101] F. Cutrale, V. Trivedi, L. A. Trinh, C.-L. Chiu, J. M. Choi, M. S. Artiga, and S. E. Fraser, "Hyperspectral phasor analysis enables multiplexed 5d in vivo imaging," *Nature Methods*, vol. 14, no. 2, pp. 149–152, 2017.
- [102] F. Fereidouni, C. Griffin, A. Todd, and R. Levenson, "Multispectral analysis tools can increase utility of RGB color images in histology," *Journal of Optics*, vol. 20, p. 044007, mar 2018.
- [103] W. Shi, D. E. S. Koo, M. Kitano, H. J. Chiang, L. A. Trinh, G. Turcatel, B. Steventon, C. Arnesano, D. Warburton, S. E. Fraser, and F. Cutrale, "Pre-processing visualization of hyperspectral fluorescent data with spectrally encoded enhanced representations," *Nature Communications*, vol. 11, no. 1, p. 726, 2020.
- [104] G. Weber and F. J. Farris, "Synthesis and spectral properties of a hydrophobic fluorescent probe: 6-propionyl-2-(dimethylamino)naphthalene," *Biochemistry*, vol. 18, no. 14, pp. 3075–3078, 1979.
- [105] G. Bianchetti, F. Di Giacinto, D. Pitocco, A. Rizzi, G. E. Rizzo, F. De Leva, A. Flex, E. di Stasio, G. Ciasca, M. De Spirito, and G. Maulucci, "Red blood cells membrane micropolarity as a novel diagnostic indicator of type 1 and type 2 diabetes," *Analytica Chimica Acta: X*, vol. 3, p. 100030, 2019.

## Bibliography

---

- [106] M. Unser, "Sampling - 50 years after Shannon," *Proceedings of the IEEE*, vol. 88, no. 4, pp. 569–587, 2000.
- [107] M. Unser, A. Aldroubi, and M. Eden, "The L2 Polynomial Spline Pyramid," *IEEE Transactions on Pattern Analysis and Machine Intelligence*, vol. 15, no. 4, pp. 364–379, 1993.
- [108] C. E. Shannon, "Communication in the presence of noise," *Proceedings of the IRE*, vol. 37, pp. 10–21, Jan 1949.
- [109] C. E. Shannon, "Classic paper: Communication in the presence of noise," *Proceedings of the IEEE*, vol. 86, pp. 447–457, Feb 1998.
- [110] N. C. Shaner, P. A. Steinbach, and R. Y. Tsien, "A guide to choosing fluorescent proteins," *Nature Methods*, vol. 2, no. 12, pp. 905–909, 2005.
- [111] R. Yuste, "Fluorescence microscopy today," *Nature Methods*, vol. 2, no. 12, pp. 902–904, 2005.
- [112] G. G. Stokes, "On the change of refrangibility of light.," *Philosophical Transactions of the Royal Society of London*, vol. 142, pp. 463–562, 1852.
- [113] B. P. Cormack, R. H. Valdivia, and S. Falkow, "FACS-optimized mutants of the green fluorescent protein (GFP)," *Gene*, vol. 173, no. 1, pp. 33–38, 1996.
- [114] H. Morise, O. Shimomura, F. H. Johnson, and J. Winant, "Intermolecular energy transfer in the bioluminescent system of aequorea," *Biochemistry*, vol. 13, no. 12, pp. 2656–2662, 1974.
- [115] W. W. Ward, C. W. Cody, R. C. Hart, and M. J. Cormier, "Spectrophotometric identity of the energy transfer chromophores in renilla and aequorea green-fluorescent proteins," *Photochemistry and Photobiology*, vol. 31, no. 6, pp. 611–615, 1980.
- [116] R. Y. Tsien, "The green fluorescent protein," *Annual Review of Biochemistry*, vol. 67, no. 1, pp. 509–544, 1998. PMID: 9759496.
- [117] C. Jaques, E. Pignat, S. Calinon, and M. Liebling, "Temporal Super-Resolution Microscopy Using a Hue-Encoded Shutter," *Biomedical Optics Express Journal*, vol. 10, no. 9, pp. 4727–4741, 2019.
- [118] D. W. Staudt, J. Liu, K. S. Thorn, N. Stuurman, M. Liebling, and D. Y. R. Stainier, "High-resolution imaging of cardiomyocyte behavior reveals two distinct steps in ventricular trabeculation," *Development*, vol. 141, no. 3, pp. 585–593, 2014.
- [119] S. S. Gorthi, D. Schaak, and E. Schonbrun, "Fluorescence imaging of flowing cells using a temporally coded excitation," *Opt. Express*, vol. 21, pp. 5164–5170, Feb 2013.

- [120] R. Raskar, A. Agrawal, and J. Tumblin, “Coded exposure photography: Motion deblurring using fluttered shutter,” *ACM Trans. Graph.*, vol. 25, pp. 795–804, 07 2006.
- [121] Y. Shiba, S. Ono, R. Furukawa, S. Hiura, and H. Kawasaki, “Temporal shape super-resolution by intra-frame motion encoding using high-fps structured light,” *ICCV*, 2017.
- [122] P. Rangarajan, I. Sinharoy, P. Milojkovic, and M. P. Christensen, “Active computational imaging for circumventing resolution limits at macroscopic scales,” *Appl. Optics*, vol. 56, no. 9, pp. D84–D107, 2017.
- [123] G. H. Golub and C. F. Van Loan, *Matrix Computations*. The John Hopkins University Press, 3 ed., 1996.
- [124] R. E. Welsch, “Robust regression using iteratively reweighted least-squares,” *Commun. Stat. Theory*, vol. 6, no. 9, pp. 813–827, 1977.
- [125] R. Chartrand and W. Yin, “Iteratively reweighted algorithms for compressive sensing,” in *ICASSP*, pp. 3869–3872, 2008.
- [126] I. Daubechies, R. Devore, M. Fornasier, and C. S. Güntürk, “Iteratively reweighted least squares minimization for sparse recovery,” *Communications on Pure and Applied Mathematics*, vol. 63, no. 1, pp. 1–38, 2010.
- [127] ILOG-CPLEX, “High-performance software for mathematical programming and optimization.” <http://www.ilog.com/products/cplex>, 2005.
- [128] C. Jaques. [https://github.com/idiap/hesm\\_distrib](https://github.com/idiap/hesm_distrib), 2019.
- [129] C. Jaques, “Supplementary material for phd thesis of christian jaques.” <https://dx.doi.org/10.5281/zenodo.3813603>, 2020.
- [130] M. Bertero and P. Boccacci, *Introduction to inverse problems in imaging*. Bristol, UK: IOP Publishing, 1998.
- [131] C. Jaques, A. Ernst, N. Mercader, and M. Liebling, “Temporal resolution doubling in fluorescence light-sheet microscopy via a hue-encoded shutter,” *Continuum Journal*, vol. 3, no. 7, 2020.
- [132] M. G. L. Gustafsson, “Nonlinear structured-illumination microscopy: Wide-field fluorescence imaging with theoretically unlimited resolution,” *Proceedings of the National Academy of Sciences*, vol. 102, no. 37, pp. 13081–13086, 2005.
- [133] S. Dillavou, S. M. Rubinstein, and J. M. Kolinski, “The virtual frame technique: ultrafast imaging with any camera,” *Opt. Express*, vol. 27, pp. 8112–8120, Mar 2019. ultrafast imaging of binary stuff – CiteMe.

## Bibliography

---

- [134] J. Marguier, N. Bhatti, H. Baker, M. Harville, and S. Süssstrunk, “Color correction of uncalibrated images for the classification of human skin color,” *Proceedings of the 15th IS&T/SID Color Imaging Conference*, pp. 331–335, 2007.
- [135] S. Boyd, N. Parikh, E. Chu, B. Peleato, and J. Eckstein, “Distributed optimization and statistical learning via the alternating direction method of multipliers,” *Foundations and Trends in Machine Learning*, vol. 3, no. 1, pp. 1–122, 2010.
- [136] L. I. Rudin, S. Osher, and E. Fatemi, “Nonlinear total variation based noise removal algorithms,” *Physica D*, vol. 60, pp. 259–268, 1992.
- [137] R. Tibshirani, “Regression shrinkage and selection via the lasso,” *Journal of the Royal Statistical Society, Series B*, vol. 58, pp. 267–288, 1996.
- [138] D. P. Bertsekas, *Constrained Optimization and Lagrange Multiplier Methods*. Academic Press, 1982.
- [139] S. Boyd and L. Vandenberghe, *Convex Optimization*. Cambridge Press University, 2004.
- [140] A. Beck and M. Teboulle, “A fast iterative shrinkage-thresholding algorithm for linear inverse problems,” *SIAM Journal on Imaging Sciences*, vol. 2, no. 1, pp. 183–202, 2009.
- [141] P. C. Hansen, “Analysis of discrete ill-posed problems by means of the l-curve,” *SIAM Review*, vol. 34, no. 4, pp. 561–580, 1992.
- [142] P. C. Hansen, *Discrete inverse problems: insight and algorithms*, vol. 7. Siam, 2010.
- [143] Y. A. Pan, T. Freundlich, T. A. Weissman, D. Schoppik, X. C. Wang, S. Zimmerman, B. Ciruna, J. R. Sanes, J. W. Lichtman, and A. F. Schier, “ZebraBow: multispectral cell labeling for cell tracing and lineage analysis in zebrafish,” *Development*, vol. 140, no. 13, pp. 2835–2846, 2013.
- [144] Y. Wan, K. McDole, and P. J. Keller, “Light-sheet microscopy and its potential for understanding developmental processes,” *Annual Review of Cell and Developmental Biology*, vol. 35, no. 1, pp. 655–681, 2019. PMID: 31299171.
- [145] M. Liebling, J. Vermot, A. S. Forouhar, M. Gharib, M. E. Dickinson, and S. E. Fraser, “Nonuniform temporal alignment of slice sequences for four-dimensional imaging of cyclically deforming embryonic structures,” *Proc. IEEE Int. Symp. Biomed. Imag.*, pp. 1156–1159, 2006.
- [146] M. Liebling and H. Ranganathan, “Wavelet domain mutual information synchronization of multimodal cardiac microscopy image sequences,” in *Proc. SPIE 7446*, pp. 744602 1–5, 2009.

- 
- [147] J. Ohn, J. Yang, S. E. Fraser, R. Lansford, and M. Liebling, “High-speed multicolor microscopy of repeating dynamic processes,” *Genesis*, vol. 49, no. 7, pp. 514–521, 2011.
- [148] C. Jaques, L. Bapst-Wicht, D. F. Schorderet, and M. Liebling, “Multi-spectral widefield microscopy of the beating heart through post-acquisition synchronization and unmixing,” in *2019 IEEE 16th International Symposium on Biomedical Imaging (ISBI 2019)*, pp. 1382–1385, April 2019.
- [149] C. Jaques and M. Liebling, “Generalized temporal sampling with active illumination in optical microscopy,” in *Wavelets and Sparsity XVIII* (D. V. D. Ville, M. Papadakis, and Y. M. Lu, eds.), vol. 11138, pp. 337 – 345, International Society for Optics and Photonics, SPIE, 2019.
- [150] C. Jaques and M. Liebling, “Aliasing mitigation in optical microscopy of dynamic biological samples by use of temporally-modulated color illumination and a standard RGB camera,” *Submitted to Journal of Biomedical Optics*, 2020.
- [151] N. Chacko, M. Liebling, and T. Blu, “Discretization of continuous convolution operators for accurate modeling of wave propagation in digital holography,” *J. Opt. Soc. Am. A*, vol. 30, pp. 2012–2020, Oct. 2013.
- [152] K. Gedalyahu, R. Tur, and Y. C. Eldar, “Multichannel sampling of pulse streams at the rate of innovation,” *IEEE Transactions on Signal Processing*, vol. 59, pp. 1491–1504, Apr. 2011.
- [153] T. Blu and M. Unser, “Quantitative fourier analysis of approximation techniques: Part I – Interpolators and projectors,” *IEEE Transactions on Signal Processing*, vol. 47, pp. 2783–2795, Oct 1999.
- [154] T. Blu and M. Unser, “Quantitative fourier analysis of approximation techniques: Part II –Wavelets,” *IEEE Transactions on Signal Processing*, vol. 47, no. 10, pp. 2796–2806, 1999.
- [155] A. A. Bell, J. Brauers, J. N. Kaftan, D. Meyer-Ebrecht, A. Böcking, and T. Aach, “High dynamic range microscopy for cytopathological cancer diagnosis,” *IEEE J. Sel. Topics Signal Process.*, vol. 3, no. 1, pp. 170–184, 2009.
- [156] H. Blasinski, J. Farrell, B. Wandell, and P. Wang, “Multispectral imaging of tissue ablation,” *Proc. IEEE Int. Symp. Biomed. Imag.*, pp. 360–363, 2016.
- [157] N. Gat, “Imaging spectroscopy using tunable filters: a review,” *Proc. SPIE Wavelet Application VII*, vol. 4056, pp. 50–64, 2000.
- [158] J. I. Park, M. H. Lee, M. D. Grossberg, and S. K. Nayar, “Multispectral imaging using multiplexed illumination,” in *Proc. IEEE Int. Conf. on Comput. Vis.*, pp. 1–8, 2007.

## Bibliography

---

- [159] C. Chi, H. Yoo, and M. Ben-Ezra, "Multi-spectral imaging by optimized wide band illumination," *Int. J. Comput. Vis.*, vol. 86, no. 2-3, pp. 140–151, 2010.
- [160] S. W. Oh, M. S. Brown, M. Pollefeys, and S. J. Kim, "Do it yourself hyperspectral imaging with everyday digital cameras," *Proc. IEEE Conf. on Comput. Vis. and Pat. Recog.*, pp. 2461–2469, 2016.
- [161] S. Galliani, C. Lanaras, D. Marmanis, E. Baltsavias, and K. Schindler, "Learned spectral super-resolution," *Proc. IEEE Int. Conf. on Comput. Vis.*, 2017.
- [162] Y. Qu, H. Qi, and C. Kwan, "Unsupervised sparse dirichlet-net for hyperspectral image super-resolution," *Proc. IEEE Conf. on Comput. Vis. and Pat. Recog.*, pp. 2511–2520, 2018.
- [163] C. Studholme, D. J. Hawkes, and D. L. G. Hill, "Normalized entropy measure for multi-modality image alignment," in *Proc. SPIE 3338*, pp. 132–143, 1998.
- [164] G. B. Dantzig, A. Orden, and P. Wolfe, "The generalized simplex method for minimizing a linear form under linear inequality restraints," *Pac. J. Math.*, vol. 5, no. 2, pp. 183–195, 1955.
- [165] O. Ronneberger, P. Fischer, and T. Brox, "U-net: Convolutional networks for biomedical image segmentation," in *Medical Image Computing and Computer-Assisted Intervention – MICCAI 2015*, pp. 234–241, Springer International Publishing, 2015.
- [166] O. Mariani, A. Ernst, N. Mercader, and M. Liebling, "Reconstruction of image sequences from ungated and scanning-aberrated laser scanning microscopy images of the beating heart," *IEEE Transactions on Computational Imaging*, vol. 6, pp. 385–395, 2020.
- [167] E. Jones, M. Baron, S. Fraser, and M. Dickinson, "Measuring hemodynamic changes during mammalian development," *American Journal of Physiology-Heart and Circulatory Physiology*, vol. 287, no. 4, pp. H1561–H1569, 2004.
- [168] A. S. Forouhar, M. Liebling, A. Hickerson, A. Nasiraei-Moghaddam, H.-J. Tsai, J. R. Hove, S. E. Fraser, M. E. Dickinson, and M. Gharib, "The embryonic vertebrate heart tube is a dynamic suction pump," *Science*, vol. 312, no. 5774, pp. 751–753, 2006.
- [169] Y. N. Tallini, M. Ohkura, B.-R. Choi, G. Ji, K. Imoto, R. Doran, J. Lee, P. Plan, J. Wilson, H.-B. Xin, A. Sanbe, J. Gulick, J. Mathai, J. Robbins, G. Salama, J. Nakai, and M. I. Kotlikoff, "Imaging cellular signals in the heart in vivo: Cardiac expression of the high-signal Ca<sup>2+</sup> indicator GCaMP2," *Proceedings of the National Academy of Sciences*, vol. 103, no. 12, pp. 4753–4758, 2006.

- [170] M. R. Hestenes, “Multiplier and gradient methods,” *Journal of Optimization Theory and Applications*, vol. 4, no. 5, pp. 303–320, 1969.
- [171] M. J. D. Powell, “Algorithms for nonlinear constraints that use lagrangian functions,” *Mathematical Programming*, vol. 14, no. 1, pp. 224–248, 1978.
- [172] C. Biscarrat, S. Parthasarathy, N. Antipa, G. Kuo, and L. Waller, “Diffusercam tutorial.” <https://waller-lab.github.io/DiffuserCam/tutorial.html>, 2019. Accessed: 2019-11-04.
- [173] M. V. Afonso, J. Bioucas-Dias, and M. A. T. Figueiredo, “Fast image recovery using variable splitting and constrained optimization,” *IEEE Transactions on Image Processing*, pp. 1–11, 2010.
- [174] R. T. Rockafellar, *Convex analysis*. Princeton University Press, 1970.
- [175] S. Diamond and S. Boyd, “CVXPY: A Python-embedded modeling language for convex optimization,” *Journal of Machine Learning Research*, vol. 17, no. 83, pp. 1–5, 2016.
- [176] A. Agrawal, R. Verschueren, S. Diamond, and S. Boyd, “A rewriting system for convex optimization problems,” *Journal of Control and Decision*, vol. 5, no. 1, pp. 42–60, 2018.





# CHRISTIAN JAQUES

📍 2000 Neuchâtel  
☎ +41 78 812 33 32  
@ cjaques@pm.me

🌐 christianjaques.ch  
🐙 github.com/cjaques

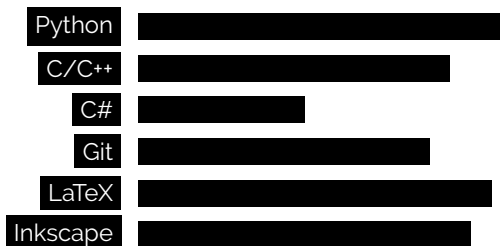
## Signal Processing Engineer

### WHO AM I?

Open minded 32 years-old Swiss and Belgian citizen, based in Switzerland.

I enjoy challenges and teamwork, especially to solve interdisciplinary problems, where my critical thinking and interpersonal skills are valuable assets.

If I am not behind a computer, you will likely find me on a bike, ski-touring, or brewing some beer.



### EXPERIENCE

- Currently **Industrial Vision Consulting Engineer** Freelance, Switzerland  
Development of optical solutions for industrial vision applications  
Image processing algorithms  
Automation lines assessment and improvement  
Python / C++ / C# / Cognex VisionPro, InSight, Vidi
- 2016 – 2020 **PhD Candidate** Computational Bio-Imaging Group, Idiap Research Institute, Switzerland  
Thesis title: *Computational methods for temporal and spectral super-resolution*  
under the supervision of Dr. Michael Liebling  
Development of applied computational methods for microscopy  
Scientific papers redaction  
Build of a light-sheet microscope  
Patent redaction in collaboration with attorneys  
Python / C++ / NumPy / Matplotlib / Fiji / Matlab / LaTeX / Inkscape
- 2015 **Computer Vision Developer** Computer Vision Lab, EPFL, Switzerland  
Porting algorithms to Ilastik  
C++ / Python / Ilastik
- 2014 **Freelance Software Developer** Cape Town, South Africa  
Web development for digital agencies and schools  
IT infrastructure implementation  
C# / Python / Django
- 2011 – 2014 **Industrial Vision Engineer** Mikron Automation SA, Switzerland  
Industrial vision for assembly lines  
Development of best/cheapest optical and algorithmic solution to inspect components  
Training of new team members  
C# development and support of Mikron's patented image processing platforms  
Over 25% of work time spent abroad – USA, South America, Asia, Europe  
Computer Vision / Cognex InSight solutions / Cognex VisionPro solutions / C#
- 2009–2011 **Teaching assistant** EPFL, Switzerland  
*Informatics I & II – C programming* Microtechnology students of 1<sup>st</sup> year: Dr. Ronan Boulic  
*Analysis I* Engineering faculty students of 1<sup>st</sup> year: Dr. Philippe Chabloz  
*General Physics IV* Engineering faculty students of 2<sup>nd</sup> year: Dr. Alfredo Pasquarello

### PUBLICATIONS AND TALKS

- Submitted in 2020 **Aliasing mitigation in optical microscopy of dynamic biological samples by use of temporally-modulated color illumination and a standard RGB camera** SPIE Journal of Biomedical Optics  
C. Jaques, M. Liebling

- August 2020 **Temporal resolution doubling in fluorescence light-sheet microscopy via a hue-encoded shutter** OSA Continuum Journal  
C. Jaques, A. Ernst, N. Mercader, M. Liebling
- September 2019 **Temporal super-resolution microscopy using a hue-encoded shutter** OSA Biomedical Optics Express Journal  
C. Jaques, E. Pignat, S. Calinon, M. Liebling
- August 2019 **Generalized temporal sampling with active illumination in optical microscopy** SPIE Wavelets and Sparsity 18<sup>th</sup> conference  
C. Jaques, M. Liebling
- April 2019 **Multi-Spectral Widefield Microscopy of the Beating Heart Through Post-Acquisition Synchronization of Overlapping Filter Bands** IEEE symposium on biomedical imaging (ISBI)  
C. Jaques, L. Bapst-Wicht, D. Schorderet, M. Liebling  
This paper won the best paper award(1<sup>st</sup> place) of the conference
- September 2017 **Imaging Monochrome Samples at Sub-Shutter Time Resolution with Hue-Encoded Illumination and an RGB Camera** Bio-Image Informatics Conference  
C. Jaques, E. Pignat, S. Calinon, M. Liebling
- 2019 **System and method for increasing the resolution of a camera** European Patent Office  
C. Jaques, M. Liebling  
Patent number EP19154253

## EDUCATION

- 2016-2020 **PhD in Computational Imaging** Idiap Research Institute, École Polytechnique Fédérale de Lausanne  
Switzerland
- 2009 – 2011 **Master's Degree, Microengineering** École Polytechnique Fédérale de Lausanne  
Switzerland
- 2007 – 2013 **Bachelor's Degree, Microengineering** École Polytechnique Fédérale de Lausanne  
Switzerland

## LANGUAGES

**French** - native  
**English** - fluent  
**Spanish** - conversational  
**German** - conversational  
**Italian** - rudimentary

## INTERESTS

Computational imaging, image processing, computer vision, signal processing  
 Industrial applications, assembly  
 Deep learning, blockchain technologies

## HOBBIES

Running (ultra-marathons, trails), rock climbing, alpinism, ski-touring, beer brewing, reading, travelling, snowboarding, biking, hiking, photography, architecture